UNIVERSITAT POLITÈCNICA DE VALÈNCIA

UNIVERSITAT POLITÈCNICA DE VALÈNCIA

School of Industrial Engineering

Study of the influence of Tantalum concentration on Ti-Nb-Zr-Ta medium entropy alloys and perspectives of future developments for biomedical applications.

Master's Thesis

Master's Degree in Industrial Engineering (Access from Bachelor's Degree in Mechanical Engineering)

AUTHOR: Guillotin, Titouan

Tutor: Amigó Borrás, Vicente

External cotutor: Correa Rossi, Mariana

ACADEMIC YEAR: 2023/2024

Dedication

A mes parents et ma famille pour leur soutien indéfectible,
en témoignage de ma reconnaissance et mon profond attachement en dépit de la distance.

A mes amis et tous ceux qui me sont chers...

Acknowledgment

I would like to first express my heartfelt gratitude to my master's thesis supervisor Vicente Amigo Borras, for his guidance and support throughout this master's thesis. His insights and knowledge of TNZT greatly facilitated the seamless execution of this research.

A special thank to the lab staff and professors for their support during the development of this project. Their willingness to help and their assistance significantly contributed to the smooth conduct of this master's thesis. In addition, I wish to thank the other students I met in the laboratory whose discussions helped lighten the mood during these long hours of sample polishing.

Finally, I extend my gratitude to my home institution, the EEIGM, along with the UPV, for providing me with this extraordinary opportunity to pursue a double degree in Valencia. This has been an unforgettable experience that greatly contributed to my academic journey and personal growth.

Abstract

This work was carried out as part of the double degree program in industrial engineering at UPV and Materials Science engineering at EEIGM. This Master's thesis focuses on the study of a medium entropy alloy (MEA) more specifically, the Ti-Nb-Zr-Ta system. The alloys studied, all equimolar in Ti-Nb-Zr, were produced by a blending and pressing powder process (BE + P&S), followed by sintering held at 1350 °C for four hours. The study seeks to evaluate the impact of tantalum content, varying between 15 to 30 percent molar, on the alloys' properties, to potentially determine the most suitable chemical composition for biomedical use. For this purpose, the mechanical, microstructural, and biochemical properties of the four TNZT alloys were examined using various experimental approaches. This included tensile and flexural testing, Vickers and Rockwell hardness measurements, as well as non-destructive techniques such as the impulse excitation method to determine the elastic modulus and the Archimedes method for evaluating porosity. The microstructural attributes and their evolution with the concentration in Tantalum were analyzed using Electron Backscatter Microscope (EBSD) analysis and X-ray diffraction (XRD). The findings indicate that increasing Ta within the 15 to 30% molar range leads generally to advantageous and promising properties for the anticipated biomaterial applications. Specifically, a significant reduction in the elastic modulus was observed alongside an enhancement in the ultimate tensile and flexural strength. A decrease in internal porosity was also identified, while the external porosity exhibited a substantial increase. It should be noted however that a marginal decrease in hardness and an increased release of metal ions in an organic medium were observed with greater Ta concentrations. Although the synthesized alloys exhibited promising mechanical and structural properties, further investigation of the corrosion behavior of the developed alloys is recommended to better understand their biocompatibility and address the observations made in this study.

Keywords— TNZT, HEA, MEA, Powder Metallurgy, Biomaterial, Tantalum, Ti-based Alloys

UNIVERSITAT POLITÈCNICA DE VALÈNCIA

Master thesis submitted for the obtention of the

Master en Ingenieria Industrial

ESCOLA TÈCNICA SUPERIOR ENGINYERIA INDUSTRIAL VALÈNCIA

Realized by

Titouan Guillotin

Study of the Influence of Tantalum Concentration on Ti-Nb-Zr-Ta Medium Entropy Alloys and Perspectives of Future Developments for Biomedical Applications

---

Academic Tutor: Mr. Vicente Amigó Borrás **Tuteur Académique:** Mr. David Horwat

Master thesis realized at

CIUDAD POLITÉCNICA DE LA INNOVACIÓN

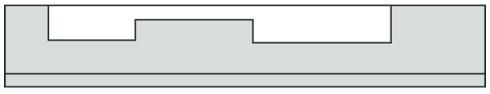

Parque Científico en Red de la UPV

Contents

List of Figures

List of Tables

Introduction

Materials have always been at the core of our civilizational development and even guided the course of history at many occasions. From the early bronze arrow tips that allowed for better hunting success to the mastering of steel and its processing from which emerged the industrial era we are living in, material history is profoundly indissociable from ours. The beginning of this civilizational journey began around 9000 BCE with the discovery of pure metals such as native gold and copper which were mainly used as ornaments. This discovery led many years later to the Chalcolithic age, also known as Copper Age, during which humankind learned to extract metal from copper ores by a smelting process. This process involved the extraction of the pure metal by heating the ores in a fire, and led to the creation of more sophisticated tools, weapons, and ornaments. However, the real breakthrough happened around 3300 BCE, with the discovery of alloying. It was discovered at that time that, the result of the contribution of several elements to the service of the same cause, often exceeded the sum of the individual effects. This groundbreaking discovery took humankind into the age of bronze, and later into the iron age by 1200 BCE. An other great turn was taken for humankind in the beginning of the nineteenth century with the discovery of the adjunction of carbon into iron. The age of steel was born. From this day on, formidable properties emerging from alloying metallic elements have never ceased to be investigated, leading to a wide array of behaviors and mechanical properties. The extensions of the metallic materials' properties through the alloying can be better shown by comparing the strength-to-density ratio map before and after the invention of alloying, as displayed in Figure 0.2.

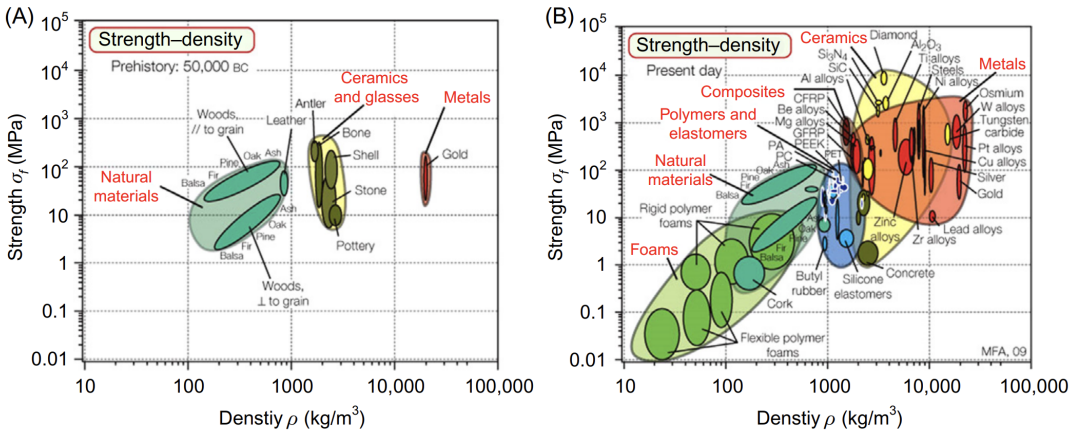

Figure 0.2: (A) prehistoric era (50,000 BCE) and (B) status in 2011 [F. Ashby, 2011].

The advent of the alloy allowed a great tunability of the mechanical properties of metallic materials, offering many adjustment parameters. The proportion of alloying elements, the proportion of phases, the control of their growth, of their geometry, become parameters on which engineers rely to adjust the properties to new emerging needs. This exceptional tunability, especially brought by the steel family quite literally changed the face of the world and almost single-handedly led us to the industrial era we know today. High-quality, affordable steel revolutionized construction, enabling skyscrapers and bridges, and expanded transportation networks with durable railways. This facilitated urbanization, boosted manufacturing efficiency with standardized machine tools, and enhanced military capabilities. The resulting economic growth and societal transformation, driven by steel's versatility, is probably the best example in our history of the pivotal role that material research and engineering play in our civilizational development. The ever increasing of alloys during this period is made obvious in Figure 0.3, where it can be seen that metal's maximum relative importance coincides with the advent of the industrial era.

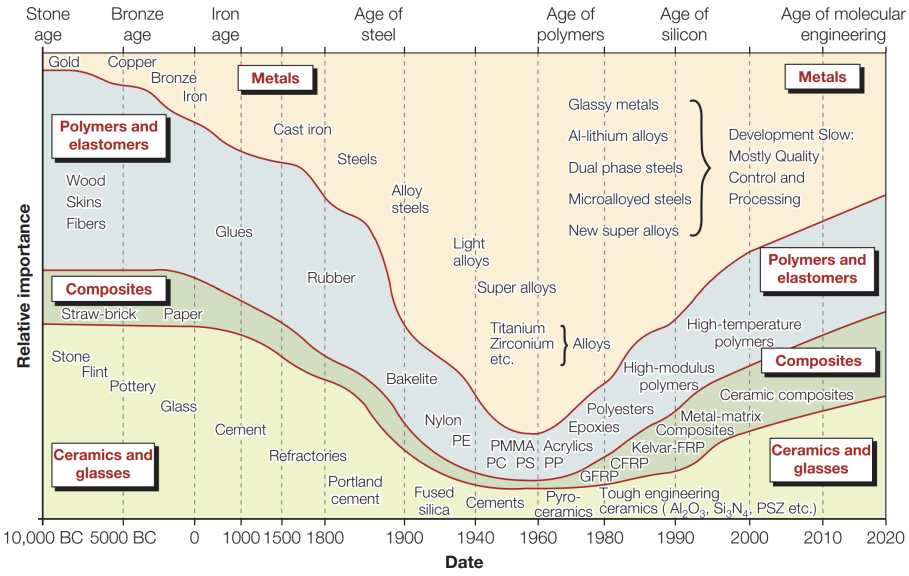

Figure 0.3: Evolution of the relative importance of each family of engineering materials with time [F. Ashby, 2011].

As this figure shows, the history of material development has since known many other events such as the age of polymers which took over the use of metallic material in many applications. Although research into new innovative steels for general applications is continuing such as TRIP steels (Transformation induced plasticity) for the automotive and naval industry; the field is slowly reaching maturity as discoveries are becoming rarer, leading researchers to investigate new approaches. One of the most interesting breakthroughs in recent years emerged from a complete paradigm shift. Rather than exploring the effects of the incorporation of elements into an already widely studied ternary or binary system such as the carbon-iron system, some research recently focused on developing new equimolar alloys composed of many elements. Although the first significant contribution to this field is often attributed to the United Kingdom and Taiwan by respectively Professors Brian Cantor and Jien-Wei Yeh in two independent studies, the question was first investigated by Karl Franz Achard more than two centuries before. In

his book published in 1788 named “Recherches sur les Propriétés des Alliages Métalliques”, he looked into the density, hardness, strength, impact resistance, ductility and the resistance of over 900 alloy compositions. Among them, some more exotic alloying systems were studied such as quinary, sexinary, and septenary alloys in equal proportions in weight. The real breakthrough for the rest of the scientific community happened many decades later with Jien-Wei Yeh’s first paper on HEAs (High Entropy Alloys) was published in May 2004 in *Advanced Engineering Materials* and was entitled “Nanostructured high-entropy alloys with multiprincipal elements—novel alloy design concepts and outcomes”. It became at the time the first publication to elucidate the concept of HEAs by providing both experimental results and related theory. This fundamental work has opened the door to numerous research and publications since 2004, with a growing interest in the last decade, as shown by the ever-increasing number of studies bearing the keyword "HEA" in Figure 0.4.

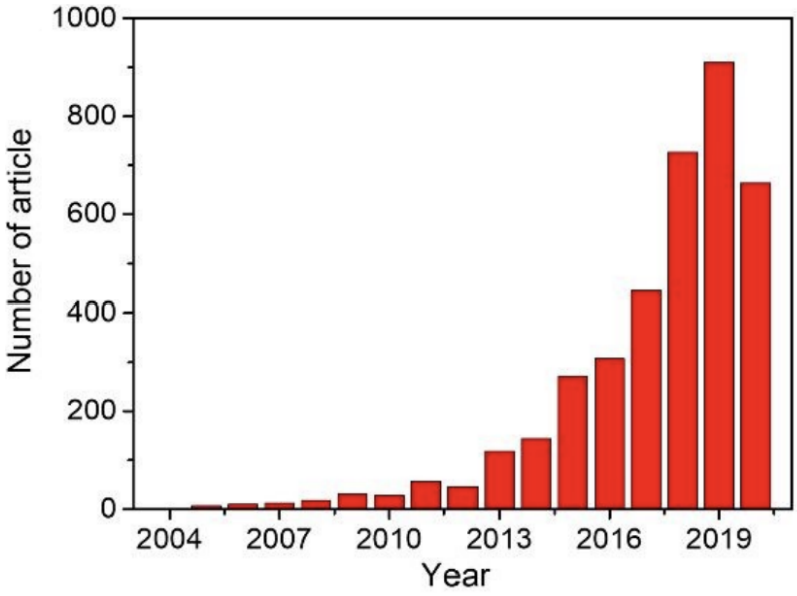

Figure 0.4: Evolution of the number of publication on HEAs between 2004 and September of 2020 [Wang et al., 2020].

This new craze around HEAs is a manifestation of the interest of the world of research. Indeed, these alloys displayed outstanding strength and hardness, notably good high-temperature performances and corrosion resistance, making for promising applications in the aeronautic industry. This new approach to alloying revealed new phenomenons specific to this new family of materials. The "sluggish diffusion" effect for instance, is an indirect effect of the high configurational entropy of the material, causes to slow down the kinetics of diffusion and phase growth considerably. This phenomenon, first described extensively by Professor Cantor, offers interesting perspectives for exploring finer microstructures. By slowing the kinetics and reducing the number of phases, it offers a promising prospect to better control the size of precipitates and grains, thereby leading to more tailorable mechanical properties. Due to these and other factors, this ground-breaking approach overcame many specific constraints of traditional alloys. By incorporating new tunable parameters and variables, this approach significantly broadened the potential uses for metal-based materials.

Among the various explored applications, one has drawn substantial interest since the emergence of HEAs. The potential use of these alloys in the biomedical industry and prosthetics has particularly sparked curiosity since the pioneering research of Professors Cantor and Yeh. The founding idea lies in taking advantage of the combination of high strength and low elastic modulus specific to this family of materials. Such properties are often inconceivable in classical alloys, yet, this unique combination is critical to best approach the characteristics of a human bone. Furthermore, the great tailorability discussed previously and offered by this type of materials, in conjunction with the porosity control offered by the different processing techniques, make these alloys one of the most serious candidates to replace the widely used Ti-based alloys in this field. In this regard, the association of Titanium, Niobium, Zirconium, and Tantalum has been extensively studied in the last few years. The low cytotoxicity of its components [Sidhu et al., 2021] grants this specific MEAs (Medium Enthropy Alloys) outstanding biocompatibility properties [Nasibi et al., 2020], thus greatly improving the osseointegration and reducing the risk of neighboring inflammation. Another advantage brought by the choice of these elements is their ability to stabilize the β phase and form a solid-state solution of all four elements. The presence of an almost uniform $\beta - Ti$ lattice allows for good hardness and strength while maintaining a relatively low elasticity modulus. Achieving a low elastic modulus is crucial for prosthesis applications to avoid damaging the bone by inducing undesirable stress-shielding effects. This effect resulting from a mismatch of the prosthesis' and bone elastic properties leads to a loss in the treated cortical bone's density, causing prosthesis loosening and overall a significant weakening of the bone over time [Guo et al., 2022, p.2-3].

Chapter 1

State of the Art

1.1 High and Medium Entropy Alloys

Before delving into this study, it is important to define the term "high entropy alloy (HEA)". As mentioned in the introduction, this new classification of metallic materials arose from a significant paradigm shift in metallurgy and alloy engineering. Professor Cantor highlighted in his groundbreaking work from just two decades ago [Cantor et al., 2002], [Cantor et al., 2004], that traditionally, alloy research has predominantly focused on the edges of phase diagrams. This means the study of systems in which one component is present in significantly smaller amounts within a matrix generally made up of a few elements. This focus has resulted in a limited understanding of the phases and mechanisms present in multicomponent alloys with nearly equal molar concentrations. This ignited a renewed interest among metallurgists and specialists, leading to the initial comprehensive studies on unconventional multicomponent systems. These research efforts began with academic works under the guidance of Professor Yeh around 1995. However, it was not until 2004, with Professor Yeh's pioneering study on Cu-Co-Ni-Cr-Al-Fe-Ti-V alloys [Nguyen et al., 2019], that the term high-entropy alloys (HEA) was officially formulated. The definition he proposed for HEAs was that of *"an alloy composed of five or more elements mixed in a near-equal molar ratio, with each element content (atomic ratio) greater than 5% and less"* [Yeh et al., 2004]. This initial composition-based definition was then extended and evolved into an entropy-based definition by quantifying the maximum entropy of the material. This maximum entropy is calculated for an ideal material, defined by [Yeh, 2006] as a liquid solution and high-temperature solid solution states where the thermal energy is high enough to cause different elements to have random positions within the structure. The mixing entropy of this theoretical material can be defined as the total contribution of configurational entropy ($\Delta S_{mix}{}^{conf}$), vibrational entropy ($\Delta S_{mix}{}^{vib}$), magnetic dipole entropy ($\Delta S_{mix}{}^{mag}$) and electronic randomness entropy ($\Delta S_{mix}{}^{elec}$) as shown in equation 1.1. That said, the total mixing entropy is governed mainly by the mixing configurational entropy, such that the approximation of Equation 1.2 is usually accepted [Wang et al., 2020, p.2].

$$\Delta S_{mix} = \Delta S_{mix}{}^{conf} + \Delta S_{mix}{}^{vib} + \Delta S_{mix}{}^{elec} \tag{1.1}$$

$$S_{mix} \approx S_{mix}{}^{conf} \tag{1.2}$$

The mixing configuration entropy can then be calculated using the Boltzmann-Planck equation and the complexion number ω as shown in Equation 1.3 where "x_i" is the molar fraction of the component "i" and "R" is the gas constant. This equation is particularized for the case of an equimolar alloy in Equation 1.4, where "n" is the number of components of the equimolar alloy.

$$S_{mix}{}^{conf} = -k.ln(\omega) = -R\sum_{i=1}^{n} x_i ln(x_i) \tag{1.3}$$

$$\begin{aligned} S_{mix} &= -R(x_1 ln(x_1) + x_2 ln(x_2) + x_3 ln(x_3) + x_4 ln(x_4)) \\ &where \quad x_1 = x_2 = x_3 = x_4 = X \\ S_{mix} &= -Rln(X) = -Rln(\tfrac{1}{n}) = Rln(n) \end{aligned} \tag{1.4}$$

According to Dr. Yeh's 2006 proposal [Yeh, 2006], the classification based on the configurational molar entropy is as follows: high when $S^{SS}{}_{ideal} > 1.61$R and medium when $0.69\text{R} < S^{SS}{}_{ideal} < 1.61$R. The configurational molar entropy for an ideal solution (SS) corresponding to each of the four synthesized alloys has been determined and is presented in Table 1.1. Even though the TNZT15 sample does not meet the criteria for a MEA as per the two definitions mentioned earlier, the study will make no distinction hereafter and will refer to it interchangeably as "medium entropy" for the sake of simplicity.

Alloy	Atomic composition [$\%_{At}$]	$S_{mix}{}^{conf}$ molar [$J.K^{-1}.mol^{-1}$]
TNZT15	$Ti_{28.33}Nb_{28.33}Zr_{28.34}Ta_{15}$	$0,357.R$
TNZT20	$Ti_{26.67}Nb_{26.66}Zr_{26.67}Ta_{20}$	$1,379.R$
TNZT25	$Ti_{25}Nb_{25}Zr_{25}Ta_{25}$	$1,386.R$
TNZT30	$Ti_{23.35}Nb_{23.33}Zr_{23.33}Ta_{30}$	$1,380.R$

Table 1.1: Total configurational molar entropy in an ideal SS of the four studied alloys, for different Tantalum concentrations.

The high degree of configurational entropy of HEAs and MEAs leads them to show novel and intriguing properties. Professor Yeh identified in 2006 four core phenomenons that may lead to these peculiar properties [Yeh, 2006]. The direct effect of the high entropy in thermodynamics, the lattice distortion effect in crystallography, the sluggish diffusion effect, and finally the cocktail effect, which impacts overall performance.

To begin with, it might be assumed that incorporating more elements into an alloy would result in a variety of intricate phase structures. However, as indicated by Equation 1.4 for an ideal equimolar SS, the configurational molar entropy rises with an increasing number of components. This rise in entropy reduces the Gibbs free energy of the material, which in turn promotes the formation of simple solid solutions at high temperatures. It was subsequently discovered that the phases emerging from this solid solution tend to be structurally simple and relatively few in number. A comprehensive review conducted in 2017, examining a sample of 648 MEAs and HEAs, revealed that 33% of the structures analyzed were single-phase alloys, 45% were dual-phase, and 16% were of other types, with the majority being disordered BCC (71.8%) or FCC (55.1%) [Miracle and Senkov, 2017, p.23]. This simple phase composition can be explained among others by the "sluggish effect". In the solid state, phase transformation and growth are

governed by diffusion. Therefore, the formation of a new phase during the cooling process requires the cooperative diffusion and redistribution of all of the atoms. It has been found in HEAs and MEAs, that the great number of components of various atomic radii had a significant impact on the nucleation and growth kinetic, by reducing the elements' diffusion coefficient in the HEAs [Tsai et al., 2013]. This sluggish diffusion effect has proved to be beneficial in controlling the properties of HEAs by promoting the formation of stable solid solutions and overall fine microstructures, leading for instance to improved creeping properties.
MEAs and HEAs also tend to have a greater lattice distortion because of the size differences of the numerous atoms they are made of. This parameter is quantified by the atomic mismatch δ, which is a crucial variable in the design and simulation of new HEAs. This parameter is used, for example, in thermodynamic models to predict the formation of single-phase disordered solid solutions [Singh et al., 2014, p.112-119]. On the other hand, while it has been shown to improve mechanical resistance in some cases, lattice strain caused by the atomic mismatch may also lead to reduced conductivity and thermal conductivity.
Finally, the last reported specificity of this novel category of alloys is the so-called "cocktail effect", named as such by Professor Ranganthan in 2003 [Ranganathan, 2003]. In a nutshell, it refers to the many degrees of freedom offered by the variety of elements that compose a HEAs. These elements serve as numerous variables that researchers and engineers can manipulate to adjust the mechanical and chemical properties of the alloys. Furthermore, varying the concentration of one element or another can result in significantly different characteristics, ranging from enhanced refractory behavior to generally superior mechanical properties. The unexpected high performance stemming from the cocktail effect is likely a key factor behind the enthusiasm and widespread interest in these materials over the past two decades.

1.2 On the Desired Properties of Biomedical Alloys

In the realm of medicine and orthopaedics, each material family is represented and plays a critical role in numerous applications. A notable example are dental prostheses, which are usually made of ceramics such as zirconia for their durability and aesthetic qualities. Polymers and hydrogels like polyethylene glycol are also significant, as methods for releasing drugs directly into the body in a more controlled fashion are explored. For wound healing, other natural organic molecules have shown promise in terms of their antimicrobial properties. Chitosan, a sugar molecule that forms the exoskeleton in some shellfish, exhibits biocompatibility, biodegradability, and antimicrobial properties, making it suitable for wound dressings and scaffolding. In orthopaedics, hydroxyapatite and tricalcium phosphate are utilized in bone grafts, while UHMWPE and PEEK are prevalent in joint and spinal implants. Biodegradable polymers such as PLA, PGA, and PLGA are employed in tendon repair and temporary bone fixation devices, which promote tissue regeneration and avoid the need for replacement surgeries. Lastly, alloys are possibly the most utilized family of materials. In surgical and orthopaedic applications, Titanium alloys and stainless steel are the most common materials, frequently used in hip and knee replacements and bone plates due to their strength and compatibility. Specifically, Ti-base alloys are preferred for their low density, excellent biocompatibility, and low elastic modulus. Noteworthy Ti-based alloys include Ti-6Al-4V, Ti-13Zr-13Ta, Ti-6Al-2Nb-1Ta, Ti-6Al-7Nb, and Ti-15Zr-4Nb-4Ta. These alloys contain varying proportions of a BCC phase and an HCP phase, and managing these phases' proportions and microstructural properties allows Ti-based alloys to exhibit high yield strength and hardness while maintaining an elastic modulus similar to human bones. This benefit is enhanced by the formation of an oxide layer, primarily titanium dioxide (TiO2), which contributes to the excellent corrosion resistance of titanium alloys.

Nevertheless, in the latest years some concerns were raised about the metal ions release effect, sometimes resulting in biological tissue responses in Ti-6Al-4V. The worries arose from the results of several studies evoking the long term effects of aluminium ions on the body, leading to potential neurodegenerative diseases including Alzheimer's disease [Hayakawa et al., 2002]. The effect of metallic ions on the body has been studied and proved to be harmful in some cases. Indeed, metallic ions exhibit a strong binding capacity to enzymes and cells in the body, forming complexes with organic and inorganic ligands. These metals alter the molecular structure of proteins by binding to groups like sulfhydryl (SH), leading to an inflammatory response of T-lymphocytes by mistakenly identifying these modified cells as foreign [Stejskal et al., 2007]. Such adverse effects were also found on current implant materials such as Ti-6Al-V, where it was found that concentrations of around 23- 30 uM in Vanadium ions, mainly $H_2VO_4^-$ and HVO_4^{2-} could significantly decrease the implant's viability [Costa et al., 2019]. This study from 2019 showed a decrease in the mice fibroblasts over time, a type of cell found in connective tissue that plays a critical role in tissue repair, leading to question the viability of peri-implant cells over long periods.

Metal components of implants are not only released as ions but also appear as microparticles in the human body. This phenomenon is particularly evident in joint prostheses like hip prostheses, where continuous friction occurs during use. In addition to enhancing ion release, causing the adverse effects described previously, these microparticles are shown to have endocrine and

reproductive impacts, along with potential carcinogenic effects. Research on the genotoxic effects of Cr, Co, Ni, V, Al, and Ti microparticles demonstrated their ability to release ions that could either cause DNA damage or hinder DNA repair. The extent of the damage varied with the prosthesis material, nevertheless, conventional Ti-V-Al prostheses resulted in a 5-fold increase in aneuploidy, defined as the occurrence of one or more extra or missing chromosomes in a cell or organism, and a smaller 2.5-fold increase for Co-Cr implants [Polyzois et al., 2012, p.265].
Last but not least, as mentioned in the introduction, it is crucial that the elastic modulus of the implant aligns with that of the bone it is meant to replace or support, in order to prevent bone stress shielding. This phenomenon occurs in load-bearing prostheses due to the implant material carrying most of the load. According to the German anatomist and surgeon Julius Wolff, bone structure is not immutable; it can remodel and adapt to repeated loading and stresses. The interior of a bone is a porous structure formed by cells undergoing constant remodelling, coordinated by the joint action of osteoclasts (which break down old or damaged bone tissue and create cavities) and osteoblasts (which fill these cavities with new bone tissue). In response to continuous stimuli, mechanosensors such as osteocytes and osteoprogenitors (which differentiate into osteoblasts and osteoclasts) regulate bone remodelling to better cope with mechanical stress [Chen et al., 2010]. These adaptations might result in bone densification or changes in alveoli geometry to handle directional loads better. What may be beneficial in various situations and sports can become risky if it leads to loss of bone density and strength. Using a prosthesis with a high elasticity modulus in a bone with a significantly lower Young's modulus results in the same strain in both materials due to the interface continuity. Consequently, the material with the highest modulus will bear most of the load, thus reducing the stress on the bone, as shown in Figure 1.1a. This effect is commonly seen in stem-inserted femur bones after total hip arthroplasty. The influence of a stiff stem under stress was investigated by calculating the Von-Mises stress at the interface in both materials by finite element simulation 1.1b. The findings shown in this figure indicate that Von-Mises' principal stress on the treated femur is nearly halved compared to the natural bone, eventually leading to a loss of bone density.

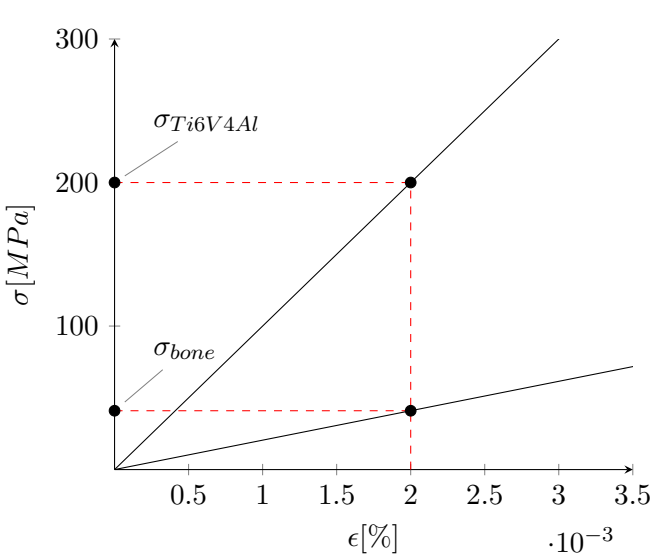

(a) Illustration of the stress shielding effect of a cortical bone by a typical T-V-Al biomaterial in their elastic domain.

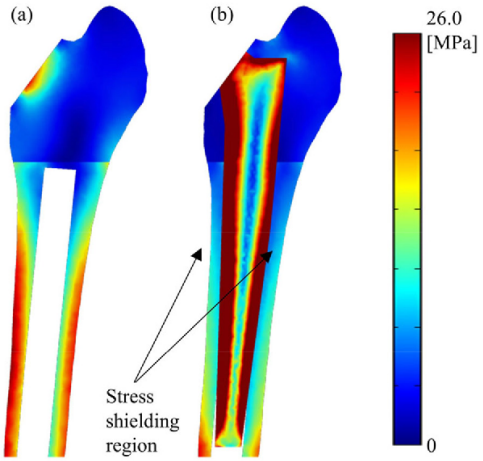

(b) Stress shielding around artificial femur simulated by FEM. The contour represents the von Mises stress of (a) natural bone and (b) bone partially replaced by an artificial femur [Nomura et al., 2022].

Figure 1.1: Illustration of the stress shielding phenomenon.

Thus, optimal material for medical implants and prostheses should exhibit the following characteristics. Good stability to ensure minimal ion release over time is needed, along with overall nontoxicity of its components. Good hardness paired with great wear resistance is necessary to minimize the amount of metal particles released into the body over the implant's lifetime. In terms of mechanical properties, high yield strength is expected so that the implant retains its properties over time and does not undergo plastic deformation during loading. On the other hand, this must be achieved while maintaining a relatively low elastic modulus similar to that of a bone, to prevent stress shielding effects of load-bearing implants which might result in a loss of the bone's density. Ultimately, the ideal material should also display a high porosity to favour osseointegration. In a recent study of 2024, the relationship between a porous metallic implant's porosity and its osseointegration was assessed by finite element modelling. The porosities between 60 and 70% were found to provide the best osseointegration, while the higher porosity values led to premature plastic deformation and failure [Mathey et al., 2024].

1.3 Emergence of TNZTs for Biomedical Applications

With these desired properties in mind, the interest naturally shifted to the HEAs and MEAs due to their specific properties that were previously highlighted. Recently, a potential new ideal material for orthopedic uses has appeared. Dr. Kopová and his team first introduced the use of a bio-compatible MEA based on the Ti-Nb-Zr-Ta-Si-Fe system in 2016 [Kopova et al., 2016]. It was found that this alloy succeeded in considerably lower the elastic modulus from 115 GPa for the currently most also reached higher cell population density and significantly higher collagen I production than cells cultured on the standard Ti-6Al-4V. This led to further investigation on the TNZ system with the addition of Tantalum or Molybdenum. These two elements are known to have a notorious β-stabilizing effect, which translates into a lowering of the β phase transition and the suppression of martensite formation passed a certain concentration threshold. Ta is also known to have a very low toxicity, leading it to be used in its oxidized form in many cosmetic products, and an overall high corrosion resistance. Therefore, it is no surprise that these alloys exhibited excellent biocompatibility, on top of excellent strength and corrosion resistance. Furthermore, it was found that the addition of 0,1 molar fraction of Ta to the TNZT system, led to an increased yield strength of 1060 MPa, while maintaining good ductility and displaying a wear resistance similar to that of traditional biomedical alloys such as Ti-6Al-4V [Akmal et al., 2021]. Several studies supported this result, although the benefits of the addition of β-stabilizers such as Ta and Mo showed some limits once passed a 0,4 mole fraction, leading to an increased brittleness and elasticity modulus while impacting the material's plasticity [Akmal et al., 2022].

There is a growing interest in incorporating tantalum or molybdenum into the TNZ system to enhance its biomedical application properties. Notably, TNZT alloys are highly suitable for such applications due to their excellent biocompatibility and unique mechanical properties, as previously mentioned. A primary challenge is to appropriately adjust the various parameters involved in developing these promising alloys. This adjustment process begins with selecting the best elaboration process to optimize prosthesis homogeneity and porosity, a subject that will not be covered in this study. The next step in this optimization involves determining the optimal concentration of tantalum within the system to better align with the desired properties. This issue will be the central focus of our investigation. It is anticipated that through collaborative efforts, the scientific community can identify this optimal balance, making TNZTs a viable material choice for the biomedical field.

Aim of the Study

This study aims to develop four high entropy alloys based on the Ti-Nb-Zr-Ta (TNZT) system developed by powder metallurgy, to explore their properties and possible applications to the biomedical sector. The MEAs thus synthesized have an increasing concentration of Tantalum (between 15 and 30% atomic in 5% increments) while maintaining an equimolar concentration of Ti, Nb, and Zr elements. The choice of these compositions covers a wide spectrum, from a material in which Ta is the minoritary component to a perfect equimolar quaternary alloy and ultimately, to a MEA in which Ta is predominant. The goal is to roughly explore the primary areas of interest in the TNZT quaternary diagram, to provide new insights for further research and finer adjustments in the composition.

The four alloys will be created by blending the elements together, followed by a pressing and sintering process (BE + P&S). This procedure, detailed in Chapter 3, will be followed by the evaluation of the primary mechanical properties of the material, including porosity type and quantity, elastic modulus, hardness, and microhardness, before examining the tensile and flexural properties. These findings will be supported by microstructural analysis to gain a better understanding of the phase content and geometry of these alloys. Finally, the behavior of the four developed alloys will be tested in a bio-like environment to study ion release over time. The characterization results are presented in Chapter 4.

It is hoped that the characterization of the obtained MEAs will help reveal the influence of Tantalum concentration on the mechanical, micro-structural, and chemical properties. These findings will be compared, and connections will be made between them to better understand how the microstructure impacts the material's performance and mechanical properties.

In conclusion, the previous findings will be examined to determine the impact of varying Ta concentration on the material's suitability for biomedical use and the existence of an optimal Ta concentration range.

Chapter 2

Study Planning

In order to best manage the raw material resources during this study, the tests and methods put in place were planned in advance. The order in which the manipulations are carried out is of great importance since some tests require different metallographic preparations or number of samples. In addition, some destructive tests such as tensile or flexural tests lead to the destruction of the sample or at least to a reduction in size, preventing in some cases further testing. Therefore, a preliminary analysis of the characteristics of each experiment and its preliminary steps must be carried out in order to detect possible interference between tests and preparations. The result of this approach is presented in Table 2.1.

Method/Test	**Studied Properties**	**Destruct. Level**	**Min. sample Frac.**
Sonelastic	Young's Modulus	NONE	1
Archimedes method	Density and porosity	NONE	1
Micro-hardness	Vickers micro-hardness	LOW	0,5
Rockwell Hardness	Rockwell hardness	LOW	0,5
Tensile Test	Ultimate & yielding strength	HIGH	1
Flexural Test	Flexural elasticity modulus	HIGH	1
XRD	Phase content	NONE	0,5
EBSD	microstructural	NONE	0,5
Ion Liberation	Behavior in bio-like medium	LOW	0,5

Table 2.1: Table of scheduled test with the corresponding studied property, destructiveness level and minimum sample fraction needed

To order and plan the study schedule, the least destructive tests were carried out first, ranging from "NONE" for those having virtually no impact on the sample's mechanical and chemical properties, to "HIGH" for those leading to deformation, work hardening and ultimately, mechanical failure. Another important parameter to take into account to not run short of material is the number of samples needed. Some tests such as micro-hardness, Rockwell hardness or ion liberation test can be performed on fractions of a sample (arbitrary fixed at 0,5 in Table 2.1), while others such as tensile and flexural tests require an entire specimen to be performed. This is particularly important to keep in mind, since as it will be explained in section 3.2.2, due to a mechanical breakdown the number of available samples per formulation was reduced to four.

The testing schedule and organization chart had to be modified accordingly, and is shown in Figure 2.1. With this organization, all tests have been performed using only four samples per formulation, leaving one spare specimen at the end for TNZT15,20 and 30.

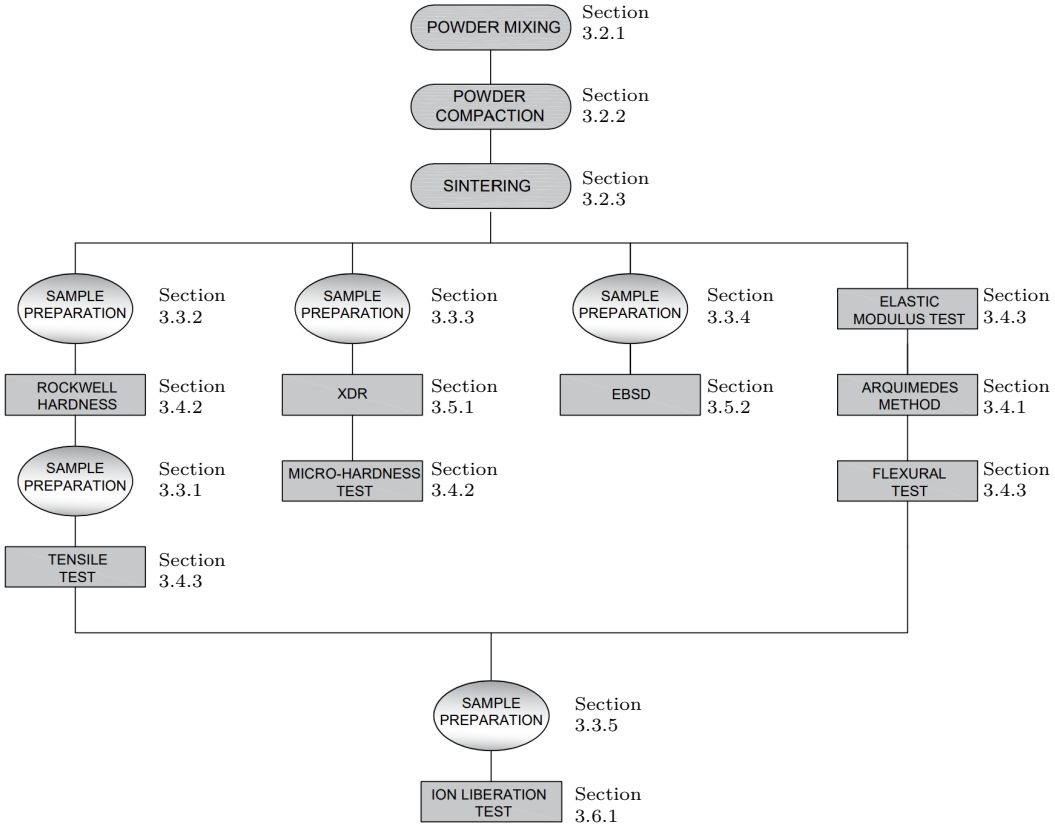

Figure 2.1: Organizational chart of the tests and methods developed throughout the study.

Chapter 3

Methods

3.1 Preamble

This study seeks to enhance the understanding of the quaternary Ti-Nb-Zr-Ta (TNZT) system by examining the different impacts of varying Tantalum concentrations. For this purpose, four distinct alloys with varying Tantalum levels were synthesized while keeping the other elements in an equiatomic ratio. The atomic fraction of tantalum in the synthesized alloys will vary from 15 at% to 30 at% by increments of 5 at %, that is, a tantalum atomic fraction of respectively 15, 20, 25 and 30 at%. Four specimens of each four alloy formulations will be synthesized by cold uniaxial pressing of the powders. Once this step is completed, a green sample will be produced that requires a sintering process to achieve the intended mechanical and chemical properties. The upcoming chapter will guide you through the various stages of this study. This includes the elaboration of the specimens used, their processing, the test descriptions as well as their parameters, and the reasoning behind the choices that were made. The chronological progression of the entire study is shown in a tree-like chart in Figure 2.1. The following section follows this layout and elaborates on the methods and materials employed in this study to achieve the desired results.

3.2 Elaboration of the Quaternary Alloys

3.2.1 Elementary Mix Elaboration

The process of producing the desired alloys begins with metallic powders which are blended in precise proportions to achieve the specified atomic fractions of Ta in the equiatomic TiNbZr matrix. To do this, the powders are weighed individually in a controlled environment to minimize the risk of altering the chemical composition of these reactive pure compounds. To estimate the total weight of the powder mixture, we first needed to determine the size of the mold used for compaction and the density of each powder mix. The granular nature and the inherent interstices between each powder grain must be considered; hence, the estimated mass must be slightly overestimated to ensure sufficient material. The degree of this overestimation is at the experimenter's discretion and depends significantly on the granularity of the used powders. The specimens to be used have dimensions of 30x12x5 mm, totaling a volume of 1.8 cm^3. We used equation 3.1 to calculate the weight percentage of each element in the desired alloy in function of the atomic fraction of each element, where "x" can be interchangeably Ti, Nb, Zr or Ta. Subsequently, Equation 3.2 was used to compute the theoretical density of the alloy with the respective atomic composition. Finally, the theoretical mass of a specimen of a given volume using was calculated using Equation 3.3, as well as the mass of each alloy's component using Equation 3.4.

$$\%W_x = \frac{\%at_x \times u_x}{\%at_{Ti} \times u_{Ti} + \%at_{Nb} \times u_{Nb} + \%at_{Zr} \times u_{Zr} + \%at_{Ta} \times u_{Ta}} \tag{3.1}$$

$$\rho_{Alloy} = \frac{100}{\frac{\%W_{Ti}}{\rho_{Ti}} + \frac{\%W_{Nb}}{\rho_{Nb}} + \frac{\%W_{Zr}}{\rho_{Zr}} + \frac{\%W_{Ta}}{\rho_{Ta}}} \tag{3.2}$$

$$M_{net} = \rho_{Alloy} \times l \times w \times h \tag{3.3}$$

$$M_x = M_{net} \times \%W_x \; ; \quad \forall\, x = Ti, Nb, Zr, Ta \tag{3.4}$$

By multiplying the net mass of each element required for the synthesis (Equation 3.4) by the N specimens (5 per formulation in this study), we derive the total powder mass of each element for every formulation. The values employed to calculate the mass percentage of each compound and the theoretical density of the alloy are the atomic weight and the density of each constituting element. These standard values can be accessed in any physical or online material encyclopedia and are displayed in Table 3.1 alongside the main properties of the powder used in the elaboration.

Therefore, the theoretical atomic and mass composition as well as its theoretical density were calculated and are shown in Table 3.2.

Metal	Atomic radii	Purity	Avg. Particle Size	Structure	Density	Atomic weight
	[pm]	[wt.%]	[μm]		[$g.cm^{-3}$]	[uma]
Ti	136	99,5	43	HCP	4,507	47,867
Nb	198	99,8	1-5	BCC	8,57	92,906
Zr	206	99,5	140	FCC	6,501	91,224
Ta	200	99,5	1-5	BCC	16,65	180,948

Table 3.1: Properties of the powders used in samples' elaboration.

Alloy	Atomic composition [$\%_{at}$]	Mass composition [%]	$\rho_{theoretical}$ [$g.cm^{-3}$]
TNZT15	$Ti_{28.33}Nb_{28.33}Zr_{28.34}Ta_{15}$	$Ti_{14.6}Nb_{28.33}Zr_{27.84}Ta_{29.23}$	7,950
TNZT20	$Ti_{26.67}Nb_{26.66}Zr_{26.67}Ta_{20}$	$Ti_{13}Nb_{25.25}Zr_{24.87}Ta_{36.88}$	8,429
TNZT25	$Ti_{25}Nb_{25}Zr_{25}Ta_{25}$	$Ti_{11.6}Nb_{22.49}Zr_{22.09}Ta_{43.81}$	8,911
TNZT30	$Ti_{23.35}Nb_{23.33}Zr_{23.33}Ta_{30}$	$Ti_{10.32}Nb_{19.99}Zr_{19.63}Ta_{50.06}$	9,397

Table 3.2: Calculated values of the theoretical atomic and mass composition of the synthesized alloys, and their theoretical density.

Each of the powders is then extracted and weighed at a precision of one-thousandth of a gram in a Jacomex model GP Campus glovebox, maintained in a controlled atmosphere ($\Delta P = 25\, mmH_2O$). By operating in a controlled environment, we ensure that no chemical compounds from the surrounding air can react with the highly reactive pure powders, with the primary concern being the oxidation of titanium due to its high reactivity. Such an oxide layer could affect the accuracy of the entire study's results. To address the inherent errors in weighing the elemental compounds, it is crucial to calculate the actual mass composition of each element and compare it to the theoretical values derived in the previous section. The results indicate an average deviation of 0.012% from the calculated values of the four alloys, demonstrating good accuracy in the procedure. The comparison of theoretical and experimental densities, as well as the percent deviation from the theoretical values, is presented in Table 3.3 below.

Alloy	Theoretical density	Experimental density	Deviation from theoretical
TNZT15	7,950 [g/cm^2]	7,950 [g/cm^2]	0,004 [%]
TNZT20	8,429 [g/cm^2]	8,427 [g/cm^2]	0,016 [%]
TNZT25	8,911 [g/cm^2]	8,910 [g/cm^2]	0,014 [%]
TNZT30	9,397 [g/cm^2]	9,396 [g/cm^2]	0,016 [%]

Table 3.3: Real and theoretical density of the synthesized alloys and deviation from theoretical values.

3.2.2 Green Samples Elaboration

The properties of the synthesized alloys, in particular their mechanical behavior, are highly dependent on their homogeneity. Consequently, it is necessary to ensure a proper homogenization of the powder before further processing by operating a thorough mixing. The powder mix obtained is placed in a sample bottle with two mixing balls of Al-Si 52100 chromed steel of 10mm diameter each. To reduce the risks of powder oxidation, this step is performed in the glovebox and the lid of each bottle is then hermetically sealed with paraffin tape. The four bottles corresponding, respectively, to the four alloys are then placed in a rotary mixer for one hour. This type of 3-axis rotary mixer is the most suited for high and medium-viscosity processes with either high solids content in small amounts or difficult mixing dispersion powders.
Once perfectly homogenized after one hour, the powder mix is removed from the mixer and taken to the hydraulic press. The mixed powders are weighted with a scale precise to the thousandth of a gram; samples will be weighted after compression to estimate the loss of material in the process. Then the press' floating matrix is lubricated with talcum powder or any kind of solid lubricant to facilitate extraction. This rectangular-shaped matrix of 30×12mm dictates the dimensions of the base of the samples. After the mixed powders are poured and the matrix is positioned on the press, the compaction process can start. In this study, an Instron model 1343 press was utilized to apply a force of 360 kN to the powder, thereby increasing the pressure to 1000 MPa for 30 seconds. Following the completion of the compression cycle, the now solidified samples are removed from the matrix by manually operating the press and using the appropriate supports. However, during this operation, the machine experienced a technical failure and broke down, causing one of the TNZT20 green samples to get stuck. This sample could not be recovered and test planning had to be changed accordingly, as explained in Chapter 2.

3.2.3 Sintering

Continuing with the sample elaboration process, the specimens of the previous phase were subjected to a heat treatment known as sintering. This thermal process involves precise control over specific factors such as temperature, atmosphere chemical composition, and more importantly perhaps the rate heating and cooling rate. In the current research, a high vacuum electric Carbolite HVT 15/75/450 furnace was used to maintain a partial vacuum of 5.10^{-4} mbar at all times. This is done to prevent specimens from oxidizing in the presence of oxygen and maintain control over titanium's reactivity. The sintering process aims to improve the alloy's mechanical characteristics by promoting atomic diffusion and recrystallization of the elements. This is particularly important in powder-elaborated alloys, where insufficient blending of the elements may lead to great chemical inhomogeneity. This process can also help release internal stress and strain that a material would have accumulated during its mechanical or thermal elaboration. The sintering process occurs at temperatures lower than the threshold fixed by the lowest melting point of all four elements. This ensures that the material maintains its solid state nature and reinforces the connections between particles by increasing the grain size and considerably improving the microstructural homogeneity. As will be discussed later, this process may also lead to changes in porosity geometry and size.
Before sintering, the green samples of each alloy are placed on a ceramic rack to prevent them

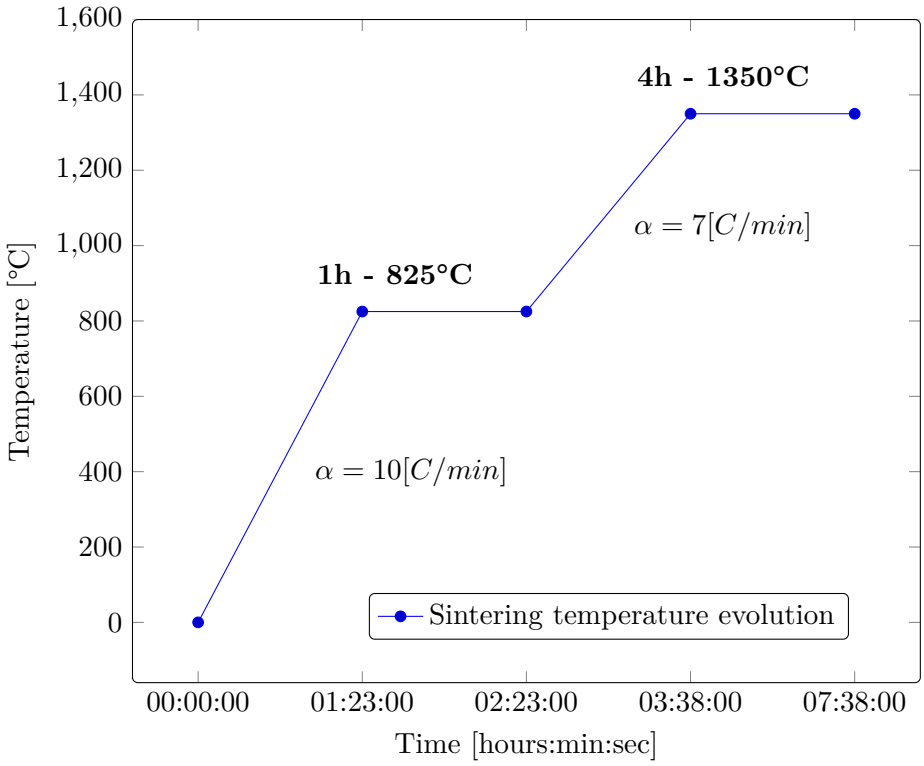

Figure 3.1: Heating phase of the sintering cycle used in the sample's elaboration.

from touching during heat treatment, which could result in unwanted interaction. Finally, the green pieces were carefully labeled and placed in the furnace. To choose the sintering parameters, it is necessary to keep in mind the lowest melting point of all elements, in this case, the titanium fusion at 3287°C, as well as the phase change temperature from phase α to β at 882°C. Between these bounds, usually, the higher the temperature, the better the diffusion and homogenization. To avoid a temperature gradient between the surface of the sample and the bulk of the material, heating followed a controlled increase at a speed of 10 °C/min from the ambient temperature, before plateauing at 825 °C for one hour. This first heating aims to achieve the best temperature homogeneity in the bulk of the material and, therefore, to ensure a uniform microstructure. The temperature is then raised above the temperature of the $\alpha \rightarrow \beta$ phase transition (at 5882°C) by increasing the temperature with a slower heating rate of $\alpha = 7$ [°C/min]. When reaching the 1350°C mark, the temperature is maintained again for four hours, before letting the furnace slowly cool. The key parameters of the thermal cycle that the samples undergo are exposed in Figure 3.1.

After sintering, the samples were removed from the furnace and placed in a desiccant enclosure to avoid any oxidation or unwanted chemical reaction before chemical characterization. Although it is known that it can have a consequent impact on the quality of the sintering, the cooling rate has not been measured in this study. The furnace was left to cool down at a rate controlled by its thermal inertia at room temperature, maintaining a controlled atmosphere.

3.3 Sample Preparation and Experimental Methods

The surface preparation of the sample is critical to ensure the accuracy of the characterization results. Some, such as the flexural test, required very little or no preparation, and others, such as X-ray diffraction (XRD) or EBSD analysis, needed a thorough metallographic treatment, going through several phases of filing and smoothing. Finally, certain tests, such as the tensile test, require the sample to be completely reshaped into a standardized specimen, involving processes such as cutting and milling. The upcoming section details these preparations, beginning with the acquisition of tensile specimens, and subsequently describes the various surface preparation techniques, arranged from the simplest to the most sophisticated.

3.3.1 Tensile Test Specimen Elaboration

In order to conduct tensile tests, it was necessary to elaborate three specimens for each alloy formulation. Due to the unusual size of the original samples synthesized by powder pressing, a parallelepiped of 30x12x5,5 mm, it was impossible to rely on normalized tensile specimen dimensions, and therefore custom specimens were created for this particular case. The process starts with the vertical milling of the parallelepiped samples with a CNC machine using a 10 mm diameter carbide end mill. The shape obtained after milling is shown in Figure 3.2 View (a) and (c). Optimal milling outcomes were achieved at speeds of 1500 rpm or more using carbide end mills. Speeds below this threshold typically caused the milling end to bend and break, as the sample's resistance resulted in the tool bending. After the CNC milling program ended and the shape of the specimen contoured, the piece was removed and taken to the grinding machine. This automatic grinding machine allowed for precise and consistent parallel cuts, by a motorized control of the grinding disk lateral displacement, with a 0,01mm precision and using water as a lubricant. Four longitudinal cuts were performed as shown in Figure 3.2 View (b), separated by 1,5 mm. The order of the cuts in this view is indicated by the four numbers, along the dotted lines. The first two cuts on each opposite side, aim to obtain two parallel flat and smooth surfaces. This allowed for two additional cuts, resulting in the three specimens per alloy required for the tensile test.

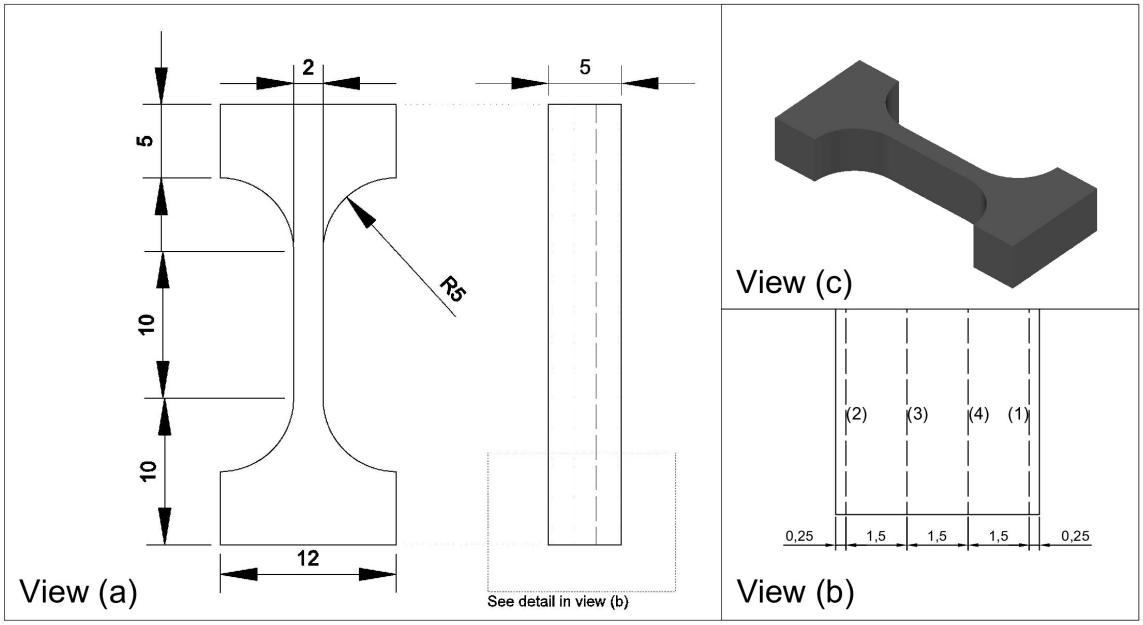

Figure 3.2: Dimensions and machining steps of the tensile specimen created in-situ (quotes in millimeters) - View (a): frontal and side view of the piece after milling - View (b): detail of the cuts performed by the grinding machine - View (c): Isometric view of the piece obtained after milling.

3.3.2 Rockwell Hardness Test Surface Preparation

In this study, it was decided to test Rockwell's hardness of both the upward and downward-facing sides of the synthesized samples. Therefore no resin encapsulation as described in the following section was possible. After sintering, the samples were taken to the metallographic preparation laboratory, where Struers' Labapol-25 filing and polishing machine was used. The samples were manually filed and polished with water as a lubricant. The samples then went through a four-step process at approximately 350 rpm with increasingly small grains: 80, 220, 5000, 10000. The initial filing was conducted on the rough surface using an 80-grit sandpaper disk to reveal the initial sublayer, followed by gradual polishing to achieve a smooth finish. To obtain the best results, surface scratching was prevented by shifting the angle by 90 ° between each change in paper grain. Once the 1000-grain filing was finished, the sample's surface displayed a homogeneous appearance with no scratch or defect visible. With this basic surface preparation, the goal is merely to obtain a surface presenting no major irregularities, since this test is much less sensitive to inhomogeneities than the micro-hardness test, due to the size of the indent.

3.3.3 XRD Analysis and Micro-hardnes Test Surface Preparation

Some characterization methods, such as the microhardness test, require the tested sample to be encapsulated to better manipulate it when surface preparation is taken a step further. This comes in particularly handy in this case, where the characterization was performed on the transverse face of the sample. The samples were first taken to the grinding machine previously used for tensile specimen elaboration, where a longitudinal cut was performed. The resulting slice of approximately 5mm in thickness is taken to the resin filling machine to encapsulate it. Although two types of polymer resin were used for encapsulation during this study, the process followed the same steps and is described below. Struers' LaboPress-3 hydraulic press was used for all samples. The elaboration of the resin resin pellet follows three phases. First, the sample is placed in the cell in the center of the machine, the resin powder is poured on top, and a zinc piston, previously lubricated with a dry lubricant, imposes a downward force of 12 kN on the powder. In the case of the preparation of the specimens for the micro-hardness test, a transparent non-conductive resin was used, Buehler Transoptic 20-3400-080. A thermal cycle follows, keeping the compacted resin under pressure, with 4 minutes of heating at 180°C, then 4 minutes of cooling. After this process, a perfectly homogeneous and solid resin pellet is obtained. The quality of this encapsulation is crucial to ensure that the applied load during the hardness test will not be absorbed by the resin's elasticity. The excess resin on the encapsulated sample and pellet edges is removed with a rotary filing machine using coarse sandpaper disks and water.

The surface preparation of XRD and microhardness samples begins following the same filing and polishing steps as previously described in Section 3.3.2. However, these two characterization methods call for a better surface finishing grade and therefore, further surface preparation is needed. After the last step of section 3.3.2, the encapsulated sample was taken to another filing and polishing machine, Struers' Labapol 5 model. The Labapol 5 machine has a rotating head with sample cells where resin pellets are placed downward. The head pressures the samples onto the polishing disk, rotating in the opposite direction. First, a Struers MD-Chem polishing pad was used with 20 N force and 9µm diamond paste for 4 minutes. For the final polishing, 0.05 µm OPS Colloidal silica (PH 10.5) and 10% oxygenated water were applied with a pipette onto a Struers MD long polishing pad, using a 10 kN force for 5 minutes.
To remove any trace of the colloidal silica solution, the samples were finally immersed and rinsed in ethanol, before being left to dry. After all these steps, the sample surface displays no irregularity and looks like a perfect mirror.

3.3.4 EBSD Analysis Surface Preparation

The elaboration of EBSD samples begins by following the same surface preparation steps as previously described in Section 3.3.3. However, in this case, Struers' Multifast conductive resin, was used for encapsulation. EBSD analysis requires to take the preparation yet another step further since the least imperfection could cause interference with the electron beam and cause the results to be unusable. Therefore, once all polishing steps were performed, samples were finally taken to another laboratory where they were placed for 1 hour each on a Buehler VibroMet 2 polishing machine, using a microcloth of the same brand and a colloidal 0.05 µm silica solution. All remaining silica were disposed of after a 5-minute immersion in water in an ultrasonic cleaner. To get rid of the last traces of humidity and greasy deposits, the samples were finally washed with ethanol and left to dry. After this preparation, the surface is respected to display a perfect mirrorlike aspect exempt from any impurities or irregularities. This last polishing step even made porosity visible to the eye.

3.3.5 Ion Release Test Surface Preparation

For this characterization, pieces of specimens from previous tensile and flexural tests were used. This was done to take advantage of the remaining pieces and avoid additional machining steps. The samples were encapsulated in Buehler 20-3400-080 transoptic resin, following the encapsulation steps described in section 3.3.3. To maximize the exposed area and ultimately improve the accuracy of the ion liberation results, broken tensile specimens were encapsulated showing their sagittal face, while the transverse face of flexural samples was exposed. To obtain three samples per formulation, two segments from a fractured flexural specimen, along with one fragment from a broken tensile specimen were used. After encapsulation, the surface was filed and polished with Struers' Labapol-25 machine and SiC sandpaper up to 10000 grains, as previously described in Section 3.3.2. After this last step, the surface was abundantly rinsed with water and acetone to remove any contamination or deposit that could affect the chemical analysis.

3.4 Mechanical Characterization

This section presents the methodology and equations used in determining the mechanical and structural properties of the different alloys. First, the volumetric and macro-structural changes that the sample exhibited after the sintering phase should be assessed. The measurement collected combined with Archemedes' method will then provide us with precious insights into the density and type of porosity. This will allow for assessing the influence of sintering on the different samples and the role the Ta concentration plays in these changes. Then the different experimental tests implemented will be presented to further characterize the main mechanical properties such as tensile and flexural behavior.

3.4.1 Volumetric Changes and Porosity Characterization

To estimate the volumetric change that occurred during sintering, the samples' three lengths were measured both before (green specimen) and after treatment with a caliper. To reduce the relative error on the volume, which is proportional to the cube of the relative error committed on each length's measurement, we chose a caliper with a resolution as low as a hundredth of a millimeter. A hypothesis was developed to accurately determine the specimen's volume. We consistently presumed that the specimens had a perfect parallelepiped shape, meaning each pair of opposite faces was exactly parallel. Based on this assumption, we ruled out any bulging of the specimen during sintering, allowing us to calculate the volume as that of a regular parallelepiped. Despite being straightforward, these considerations are crucial since the precision of the density measurement using Archimedes' method relies on them.
Taking all these factors into account, the volumes of both green specimens and sintered samples were determined using Equation 3.5, and the relative change in volume during sintering was evaluated using Equation 3.6.

$$Volume_{specimen} = Length * Width * Height \tag{3.5}$$

$$\Delta Volume[\%] = \frac{Volume_{beforesintering} - Volume_{aftersintering}}{Volume_{aftersintering}} \tag{3.6}$$

Once the volume of each sintered specimen was obtained, their weight was carefully measured with a precision of a thousandth of a gram (scale reference: KERN PFB 300) in order to perform Archemedes' method for density and porosity characterization. This commonly employed method is grounded in the principle that the buoyant force experienced by an object when submerged in a liquid equals the weight of the displaced liquid. The volume a sample displaces can thus be determined by measuring the difference between its weight in air (M_{dry}) and its weight when fully submerged in a fluid, commonly water, $M_{submerged}$. To differentiate between open and closed porosity types, the specimen is removed from the fluid and weighed again. This resulting mass is referred to as $M_{saturated}$ and includes the weight of the material along with the fluid held within the open pores of the sample. This technique is especially beneficial for analyzing the general density as well as the type porosity, making it a particularly valuable tool for applications presenting a high-porosity such as powder-elaborated alloys. In this test, the ideal volume that a perfect parallelepiped-shaped specimen with no porosity should occupy for

its measured mass is referred to as "Ideal external volume", abbreviated to "V ext. ideal". The samples were submerged in water, the mass is expressed in grams, and the volume in cm^3 to simplify the calculus. The ideal external volume was calculated from the theoretical density of each alloy shown in Table 3.3 and Equation 3.7. Next, Equation 3.8 was employed to determine the actual external volume of the material, factoring in open porosity and surface irregularities. The exact volumes of open, closed pores, and the total porosity were computed using Equations 3.9, 3.10, 3.11 respectively. By applying this approach, the percentage of open and closed porosity relative to the ideal external volume was determined through Equations 3.12 and 3.13.

$$V_{ext.\,ideal} = \frac{M_{dry}}{\rho_{theoretical}} \tag{3.7}$$

$$V_{ext.\,real} = M_{saturated} - M_{submerged} \tag{3.8}$$

$$V_{open\,porosity} = M_{saturated} - M_{dry} \tag{3.9}$$

$$V_{closed\,porosity} = V_{ext.\,real} - V_{ext.\,ideal} - V_{open\,porosity} \tag{3.10}$$

$$V_{total\,porosity} = V_{closed\,porosity} + V_{open\,porosity} \tag{3.11}$$

$$\%Open\,porosity[\%] = 100 \times \frac{V_{open\,porosity}}{V_{ext.\,ideal}} \tag{3.12}$$

$$\%Closed\,porosity[\%] = 100 \times \frac{V_{closed\,porosity}}{V_{ext.\,ideal}} \tag{3.13}$$

In the same way, the absolute and relative densities of the green and sintered specimens, expressed as a percentage of the theoretical density, were determined by measuring their mass and external volume. This was calculated using Equation 3.14, followed by Equations 3.15 and 3.16. Finally, the total porosity previously calculated was considered to determine the actual relative density of the material, as shown in Equation 3.17.

$$\rho_{green} = \frac{M_{green}}{V_{ext.\,ideal}} \quad \rho_{sintered} = \frac{M_{sintered}}{V_{ext.\,ideal}} \tag{3.14}$$

$$Green\,Relative\,Density[\%] = 100 \times \frac{\rho_{green}}{\rho_{theoretical}} \tag{3.15}$$

$$Sintered\,Relative\,Density[\%] = 100 \times \frac{\rho_{sintered}}{\rho_{theoretical}} \tag{3.16}$$

$$Real\,Sintered\,Relative\,Density[\%] = 100 \times \frac{M_{sintered}}{V_{sintered} - V_{total\,porosity}} \tag{3.17}$$

3.4.2 Hardness Characterization

The concept of material hardness is crucial for the development of new materials, especially for prosthetic applications. Since hardness is typically associated with high wear resistance, it should be accurately evaluated and fine-tuned to meet the required standard. The Rockwell and Vickers tests are two commonly used methods for evaluating hardness. The Rockwell hardness test consists of using a diamond cone or steel ball in the case of this study, to indent a material under a set load and then measuring the depth of the indentation to determine its hardness. This test is specifically designed to evaluate the hardness of both metallic and non-metallic materials. However, the Vickers hardness test uses a diamond indenter in the shape of a pyramid to produce a square indent pattern, allowing an accurate measurement of hardness by computing the area of the indentation. Both Rockwell and Vickers tests have unique benefits in determining the hardness of the material. Rockwell hardness test has the great advantage of requiring very little sample preparation and wide applicability to various materials of diverse hardness. This test remains sensitive to bad planarity; therefore, for all of the aforementioned reasons, it was decided only to characterize hardness at the macroscale with this method.
Rockwell hardness test was performed with a Centaur HD9-35 machine, using an HRT15 scale with 147 Newtons of applied force maintained during 10 s. Five measurements were performed in line and by sample, and their value was read directly on the machine.
Microhardness testing was conducted using a Vickers Shimadzu HMV-2 machine featuring an automatic reading system (ARS) interfaced with a computer. The preparation of the sample followed the procedure described in Section 3.3.3. During data collection, ten measurements were taken, divided between the upper and lower sides of the specimens to investigate the effect of compaction orientation on microhardness. The entire testing process adhered to ASTM E384 standard guidelines. These guidelines specify that the minimum distance between the nearest sides of two indentations must be $2.5 \times d$, and the distance from the indentation center to the nearest specimen edge must be greater than $2.5 \times d$, where d is the largest diagonal of the indent. This ensures avoidance of work-hardening effects due to close indentations and proximity to the sample edge. Additionally, a critical factor in Vickers microhardness testing is ensuring a smooth surface through meticulous preparation and indenting sufficiently far from any material pores. Nonetheless, a closed pore beneath the tested surface may cause the indenter to penetrate deeper, resulting in a distorted indent. Such instances were documented, the position was noted, and the respective hardness values were excluded from statistical analysis.

3.4.3 Elastic, Tensile and Flexural Properties Characterization

Impulse Excitation Characterization

Ultrasonic techniques, such as the impulse excitation principle, come in practical when analyzing Young's modulus in highly porous materials such as powder-elaborated MEA, thanks to their ability to accurately and non-invasively assess the material's elastic properties. Conventional mechanical testing such as a tensile test may be difficult or not feasible in high-porosity materials because of the amount of pores and complex microstructures. Ultrasonic methods bring a special benefit as they rely on how ultrasonic waves propagate through porous structures. By examining

how fast these waves travel through the material and how they lose energy, Young's modulus can be determined to provide insights into the material's stiffness and deformation characteristics. Several main benefits led us to the utilization of ultrasonic techniques. Firstly, ultrasonic testing offers an accurate estimation of Young's modulus without the need for invasive sample preparation or destruction during the test. This allowed for multiple measurements and analysis without causing damage and offered the possibility to reuse the specimens for further testing. This ultrasonic characterization was performed using ATCP-Sonelastic equipment paired with ATCP Sonelastic 3.0 software. The dry mass as well as the specimen dimensions were measured and entered in the software prior to the analysis. The realization of the test is straightforward and consists of placing vertically a directional microphone, aligning it with the center of the upward-facing side of the specimen, and lightly hitting one of its corners with a small metallic hammer. These measurements were repeated at each corner of the sample successively and 15 measurements per alloy were collected. Before conducting this test, it is crucial to verify that all sides, especially the surface being struck, are smooth and flat.

Tensile and Three-points Flexural Test

Tensile and flexural tests are among the most straightforward and used ways to access the material's main mechanical properties. It usually consists of applying an increasing force, whether a tension or a flexion, and observing the corresponding deformation of the material over time. The quantification of the deformation can be measured in several ways, the two most frequent being with extensometer gauges stuck onto the specimen, or by optical means, by tracking a reference point with a camera. The displacement of the movable cross-beam applying the load can also be computed to indicate the displacement applied to the specimen, although in this case the strain of the machine's components needs to be accounted for. In the case of this study, a Shimadzu Autograph AG-100kN was used for both tensile and flexural test, relying on an optical system to characterize the specimen's strain. Three tensile samples were prepared according to the procedure outlined in Section 3.3.1. Once the three tensile samples for each alloy are prepared, a white dot is marked at the center of each specimen to indicate its position. The specimen is then inserted into the jaws of the tensile machine. Before starting the test, the test sample is subjected to tension by manual operation of the machine. Other samples were reused after hardness characterization to perform the flexural test. In this case, no further surface preparation was needed. Prior to the test the sample was deposited on a support, where it rests in equilibrium on two semi-cylindrical grooves, leaving only one degree of freedom in rotation and two in translation. A second part of the matrix with similar supports is approached from above and imposes an increasing uniaxial vertical force onto it. The sample is therefore subjected to a pure bending stress, and its vertical deformation as a function of the applied force is tracked by a camera connected to the software. The test ends when the sample is broken, which allows for the characterization of the ultimate strength in addition to the elastic flexural modulus and yield strength.

3.5 Micro Structural Characterization

X-ray Diffraction

In this section, X-ray diffraction (XRD) analysis method is described. XRD is often utilized in material science research as an effective method to explore crystallographic properties and structural characteristics. This non-invasive method uses X-rays to interact with the atomic structure of materials, producing diffraction patterns, which once analyzed can offer important details on crystal phases, crystallinity and lattice parameters. This section outlines the experimental procedures and data interpretation approaches used in performing XRD tests, which include sample preparation, instrument configuration, and diffraction pattern analysis. All specimens were first encapsulated into a transparent non-conductive resin from Buehler, the TransOptic 20-3400-080, and the exposed surface went through a surface preparation as described in section 3.3.3. One sample of each alloy formulation was then analyzed with a Bruker D2 Phaser diffraction machine, with a scanning speed of 0,005°/s. Resulting diffraction patterns were obtained for angles between 20° and 90°, these results were exported in several file formats .raw, .txt, and .brml. In the context of this study, it was decided to use Maud software for diffraction data analysis. Only .xrdml file format are read by this program, which is why SQLite Version 3.12.2 conversion software was used. This application developed by SQlitebrowser allows for file format conversion from Bruker's proprietary format .brml to readable .xrdml crystallographic files to be opened by Maud.

Electron BackScatter Diffraction analysis

Electron backscatter diffraction (EBSD) is considered to be one of the most effective methods for analyzing the microstructure of a sample. This technique of examining matter by studying the interaction between electrons and atoms was initially discovered by Nishikawa and Kikuchi in 1928 when they first observed EBSD patterns. Since then, it has been extensively used in research. EBSD analysis is performed in a scanning electron microscope (SEM), where a smooth and polished crystalline sample is positioned in the sample chamber at a steep angle from the horizontal (usually around 70°), and the electron beam is focused on a specific spot on the surface. The incoming electrons interact with atoms near the sample's surface, typically within the top 10-200 nm, and scatter in various directions while retaining most of their energy. The key of this analysis lies in the relation that these scattered electrons satisfy, which is known as Bragg diffraction law and shown in Equation 3.18.

$$n.\lambda = 2.d.sin(\theta) \tag{3.18}$$

Where n is an integer, λ represents the wavelength of the electrons, d is the spacing between two lattice planes, and θ is the angle of incidence of the radiation. The diffracted electrons cause "Kikuchi" lines and bands to appear on a fluorescent phosphor screen located close to the sample. These patterns, reflect the crystallographic details of the material and form the electron-backscatter diffraction (EBSP) pattern. This EBSP contains all the information about the crystal structure at the interaction point with electrons. Therefore, by rotating the crystal or changing the material phase, EBSD analysis allows for the measurement of crystal orientations

and identification of phases across the sample's surface. To analyze the diffraction patterns which constitutes a huge amount of data, computer programs and softwares are used to speed up the process. In the present study, Oxford Instruments Aztec software was used to extract the data and plot them in a comprehensible manner. The excellent spatial resolution (tens of nanometers) and accurate crystalline orientation measurements (0.1° to 1°), make EBSD a powerful method for analyzing microstructure. In some cases it can also be combined with energy-dispersive X-ray spectrometry (EDS) to analyze sample composition to provide crucial insights about a material's composition. Thus, the precision of the results relies significantly on the smoothness of the surface, which explains the detailed surface preparation of the samples as discussed in Section 3.3.4.

3.6 Biochemical Characterization

3.6.1 Ion Release Test for Biocompatibility

In preparing samples for the ion liberation test, it is essential to precisely determine the metal area exposed to synthetic saliva. To achieve this, samples from the EBSD analysis were reused to leverage the high-quality surface preparation previously done and discussed in Section3.3.4. Furthermore, each sample for this specific test was prepared as described: the surface of the samples was treated according to methodology. A square region was outlined on the sample's surface, and the surrounding area was masked with nail polish to prevent contact with the saliva-like solution. To measure the outlined area accurately, an image analysis method was selected. A 1-centimeter reference line was measured with a caliper having a 0.01 mm resolution and marked on the resin. Photographs of each prepared sample were taken from a fixed height and then analyzed using Image J software. This tool allows for the precise measurement of the outlined surface area using the 1-centimeter reference mark for scaling. Subsequently, a saliva-like solution was prepared on-site with the composition given in Table3.4, and the pH was measured.

	NaCl	**KCl**	**CaCl2**	**HC3H5O3**	**PH**
Measured amound	6,002	0,375	0,232	5,16	6,38

Table 3.4: Composition of one liter of the elaborated saliva-like solution based on Ringer-Hartmann's solution composition.

The specimens were subsequently positioned with the metallic surface oriented downward within a sealed plastic container that contained 50 ml of the synthetic saliva solution prepared. They were kept in the incubator, model Selecta 2000207, for a duration of 744 hours at a constant temperature of 37°C before being removed. The samples were carefully retrieved to retain as much synthetic saliva in the container as possible, while ensuring not to contaminate the solution and change its chemical composition. The containers were then hermetically sealed and sent to the chemistry lab to analyze the concentrations of Ti, Zr, Nb, and Ta ions using inductively coupled plasma optical emission spectroscopy (OCDS).

Chapter 4

Results

This study investigates the influence of the variations in tantalum concentration on the properties of powder-based Ti-Zn-Nb-Ta alloys. The distinctive properties of tantalum, which influence the strength, corrosion resistance, and biocompatibility of the material, will be examined by evaluating the mechanical, structural, and chemical properties of each MEA formulation. By systematically varying the Ta content in the alloy compositions, the optimal concentration is sought that optimizes specific properties for different applications. The results of this systematic approach are presented herein and aim to provide new insights into the relationship between Ta concentration and alloy performance.

4.1 Density, Porosity and Volumetric Changes Through Sintering

4.1.1 Post Sintering Volumetric Change

This section presents the observed volumetric changes undergone by the TNZT medium entropy alloys during sintering. Understanding the volumetric evolution of these powder-pressed alloys during this crucial phase is of the utmost importance to optimize processing parameters and evaluate their suitability for future applications.
The subsequent section presents the degree of volumetric expansion or contraction observed in the MEA specimens after sintering, shedding light on the impact of Ta concentration. For this analysis, the average volumetric expansion of each specimen and the mean expansion for each alloy type were calculated. Measurements were taken with a caliper accurate to a hundredth of a millimeter before and after sintering to determine the volumetric changes, assuming each specimen to be a perfect parallelepiped. The findings are presented in Table 4.1.

Alloy	Specimen	Volume of green specimen $[cm^3]$	Volume after sintering $[cm^3]$	Δ Volume [%]	Mean Δ volume [%]	Standard deviation [%]
TNZT15	1843	2,00	2,02	1,11	6,20	4,56
	1844	1,92	2,05	7,13		
	1845	1,94	2,03	4,77		
	1846	1,80	2,05	13,40		
	1847	1,95	2,03	4,59		
TNZT20	1848	2,07	2,12	2,25	7,04	5,07
	1849	1,98	2,10	5,97		
	1850	2,01	2,12	5,74		
	1851	1,87	2,13	14,21		
TNZT25	1852	2,01	2,18	8,25	7,89	1,50
	1853	2,00	2,17	8,68		
	1854	1,99	2,19	9,80		
	1855	2,05	2,18	6,41		
	1856	2,07	2,20	6,33		
TNZT30	1857	2,06	2,25	9,04	9,47	1,12
	1858	2,05	2,25	9,85		
	1859	2,06	2,24	8,64		
	1860	2,07	2,24	8,59		
	1861	2,02	2,24	11,26		

Table 4.1: Volumetric change after sintering for each formulation of alloy.

Looking at the results shown in Table 4.1, a clear trend emerges from these results. A correlation is observed between volumetric change and Ta content in the MEA alloys analyzed. In fact, it seems that the higher the Ta content and the greater the dilatation, such as the absolute volumetric change in percentage increases from 6,20 % for 15%$_{at}$ Ta to 9,47 % when the atomic concentration of Ta reaches the 30% mark. This result provides a promising insight into the future behavior of the material, as materials usually undergo a densification phase during sintering.

4.1.2 Density and Porosity

Assuming the specimens maintain a perfect parallelepiped shape, a deeper examination of their properties was carried out by calculating their overall porosity and density. This analysis was conducted by determining the porosity of the samples using the Archimedes method, the results of which are presented in the following section. In presenting these results, some will appear as a percentage of a theoretical "ideal volume". The ideal volume for each formulation and specimen has been determined by multiplying the specimen's post-sintering weight by the theoretical density of the alloy, as outlined in Table 3.2. The Archimedes method provides us with crucial information regarding the type and extent of the material's porosity, as well as its actual apparent density, calculated based on the true volume of the specimens (accounting for porosity). The obtained porosity values for each specimen are divided into two categories: Open and closed pores, as shown in Table 4.2 and expressed as a percentage of the ideal volume. Table 4.3 highlights the changes in the ratio of open to closed porosity as a percentage of total porosity, relative to the tantalum content in the equiatomic Ti-Nb-Zr matrix. These results are finally put into perspective in Figure 4.1, where the effect of Ta concentration on open and closed porosity is better shown and displayed more visually. Conversely, the evolution of the real density with the concentration of Tantalum, logically displays an opposite trend and is shown in Figure 4.2, where the density of green samples (pre-sintering) and post-sintering samples is represented as a percentage of the ideal theoretical density.

		TNZT15	**TNZT20**	**TNZT25**	**TNZT30**
Theorical density	$[g/cm^3]$	7,95	8,43	8,91	9,40
Open pores	[% $V_{ext.ideal}$]	8,29%	12,29%	15,46%	17,53%
Closed pores	[% $V_{ext.ideal}$]	2,26%	0,95%	0,46%	0,37%
Total porosity	[% $V_{ext.ideal}$]	10,55%	13,24%	15,92%	17,90%
Mean rel. dens.	**[% Theo. dens.]**	**89,45%**	**86,76%**	**84,08%**	**82,10%**
SD	[%] $\rho_{theoretical}$	0,24%	0,48%	0,15%	0,09%

Table 4.2: Results of Archimedes' method for determination of porosity and density.

		TNZT15	**TNZT20**	**TNZT25**	**TNZT30**
Total porosity	(% of $V_{ext.ideal}$)	10,55%	13,24%	15,92%	17,90%
% Open pores	(% of total porosity)	78,55%	92,82%	97,13%	97,94%
% Closed pores	(% of total porosity)	21,45%	7,18%	2,87%	2,06%

Table 4.3: Porosity type within each formulation.

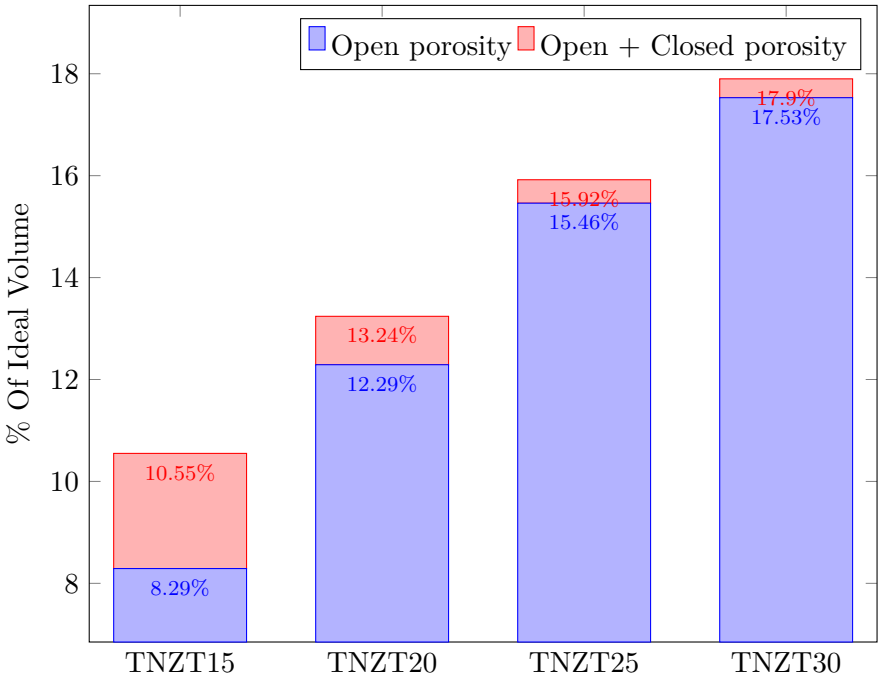

Figure 4.1: Evolution of open, closed, and total porosity with the concentration in Tantalum.

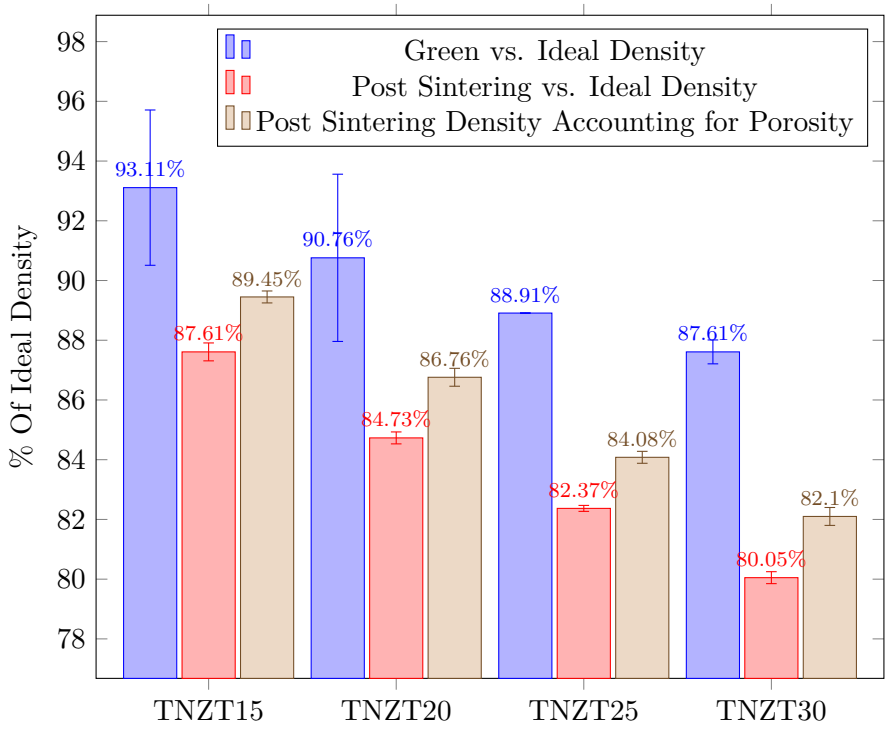

Figure 4.2: Density evolution of pre and post-sintering alloys corrected for porosity.

Based on these observations, the following conclusions can be drawn. First, there is an evident correlation between total porosity and Tantalum concentration in the MEA alloy, as depicted in Table 4.2. Increasing the Ta concentration from 15 to 30$\%_{at}$ caused the total porosity, which includes both open and closed pores, to rise from 10.55% to 17.90% of the sample's theoretical

volume. This increase in total porosity demonstrates a linear trend, which is better illustrated in Figure 4.1, showing the distribution between open and closed porosity. Notably, the evolution of closed or internal porosity exhibits the opposite pattern, indicating an inverse correlation with Ta concentration. The higher the concentration, the lower the volume of inter nal pores. Nevertheless, the significant increase in open porosity offsets this reduction in internal pore volume, resulting in an overall rise in total porosity. This pattern is more clearly shown in Table 4.3, which represents open and internal porosity as a percentage of the total porosity. Finally, the impact of the effect of Ta concentration on material density is summarized and illustrated in Figure 4.2. This combined graph addresses several previously mentioned phenomena. Firstly, it illustrates the expansion experienced by the material during the sintering process by comparing the green relative density with the density after sintering. The relationship between the volumetric change and the Ta content of the alloy are more thoroughly detailed in Table 4.1 in the previous section. The densities of both green and sintered samples exhibit a decreasing trend as the tantalum concentration increases. This reduction is a direct consequence of the previously mentioned porosity changes, illustrated in Figure 4.1.
Finally, after sintering, the relative density was re-evaluated considering the porosity measurements to determine the actual density of the material. In other words, this calculation excludes any porosity present. To achieve this, the relative density was recalculated by deducting the total pore volume from the outer volume of the sintered samples. These findings are also depicted in Figure 4.2 and described as true density. They reasonably show a higher relative density in comparison to porous sintered samples while exhibiting an inverse correlation with Ta concentration.

4.2 Mechanical Characterization Results

4.2.1 Tensile and Flexural Properties

Young's Modulus Determination By Impulse Excitation

The elastic modulus can be determined in numerous ways. This section focuses on presenting the results in a non-destructive ultrasonic way, based on the material's acoustic impedance to measure its elastic modulus. This impulse excitation technique has been favored over others for two reasons. First, it allows for reusing the tested specimens after the measurements due to their nondestructive nature, and second, it provides a more accurate measurement in the case of porous materials. Other methods for characterizing Young's modulus, such as tensile tests, can also be performed, but their results are very sensitive to any impurities or pores within the material. The main findings acquired with this technique are compiled and shown in the following section.

	TNZT15	**TNZT20**	**TNZT25**	**TNZT30**
Mean E [GPa]	69,32 $_{(SD=0,9)}$	67,23 $_{(SD=1,18)}$	66,33 $_{(SD=0,53)}$	63,57 $_{(SD=0,52)}$
Median E [GPa]	68,9	67,2	66,3	63,5

Table 4.4: Young's moduli of the four TNTZ computed on 15 samples per alloy formulation.

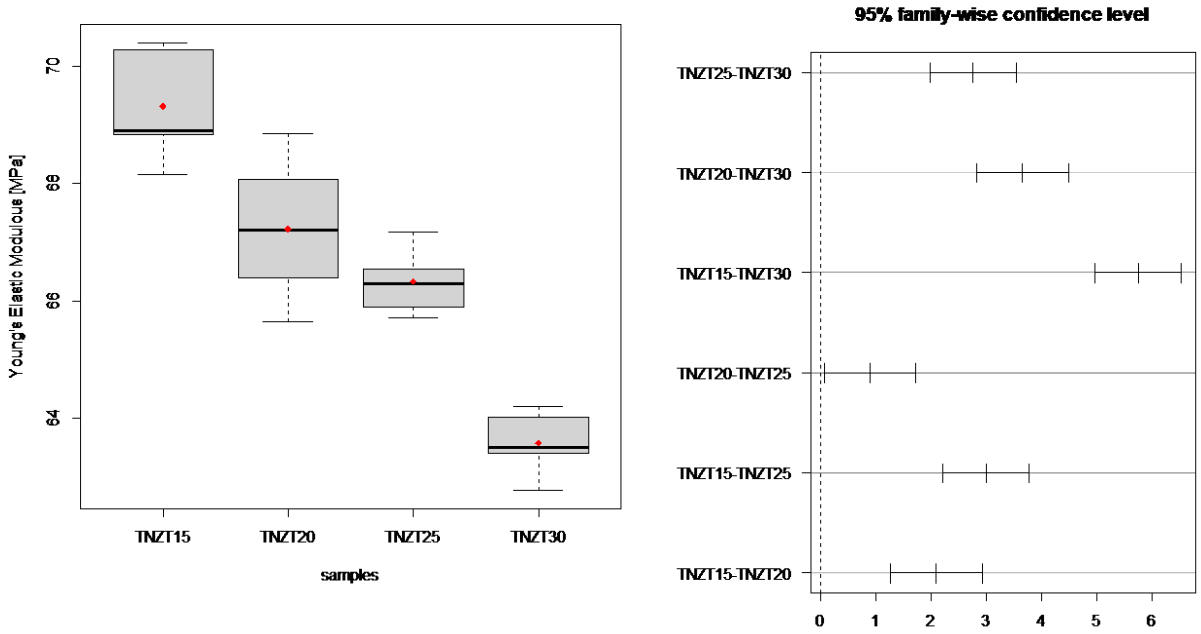

(a) Young's modulus measurement results

(b) Differences in mean levels of samples (95% family-wise confidence level)

Figure 4.3: Statistical analysis of Young's modulus by non-destructive impulse excitation technique (Sonelastic).

The Young's modulus characterization results, based on 15 measurements for each alloy composition, are presented in Table 4.4, which reveal a low standard deviation and a declining

trend with increasing tantalum concentration. This relationship between tantalum content and elastic modulus is more clearly illustrated in the boxplot in Figure 4.3.a. The set of fifteen measurements per group provided a sufficient sample size for the statistical analysis of the mean differences among different alloy formulations, as shown in Figure 4.3.b. Based on these findings, it can be concluded with a 95% confidence level that each alloy composition has a distinct mean elastic modulus that decreases as tantalum concentration rises from 15 to 30$\%_{at}$.

Flexural Properties

The flexural properties of the material under study are examined the following section. The three-point flexural test is among the most common for evaluating a material's stiffness, strength, and deformation behavior under bending loads. By analyzing flexural properties such as flexural strength and flexural modulus of elasticity, valuable information is obtained regarding the material's ability to withstand bending and how well it maintains its structural integrity under such loads.

	TNZT15	**TNZT20**	**TNZT25**	**TNZT30**
Max Force [N]	7756,19 (SD=158,63)	6746,63 (SD=231,5)	9343,79 (SD=611,25)	9448,63 (SD=316,91)
σ_f [N/mm2]	308,08 (SD=54,52)	281,12 (SD=10,97)	380,77 (SD=24,94)	372,3 (SD=13,75)
Standard slope [N/mm]	45159,77 (SD=5116,98)	43465,8 (SD=5202,54)	48640,5 (SD=2354,43)	45237,03 (SD=1022,83)

Table 4.5: Results of the three-point flexion test, showing the evolution of the flexural strength and stiffness with Ta concentration.

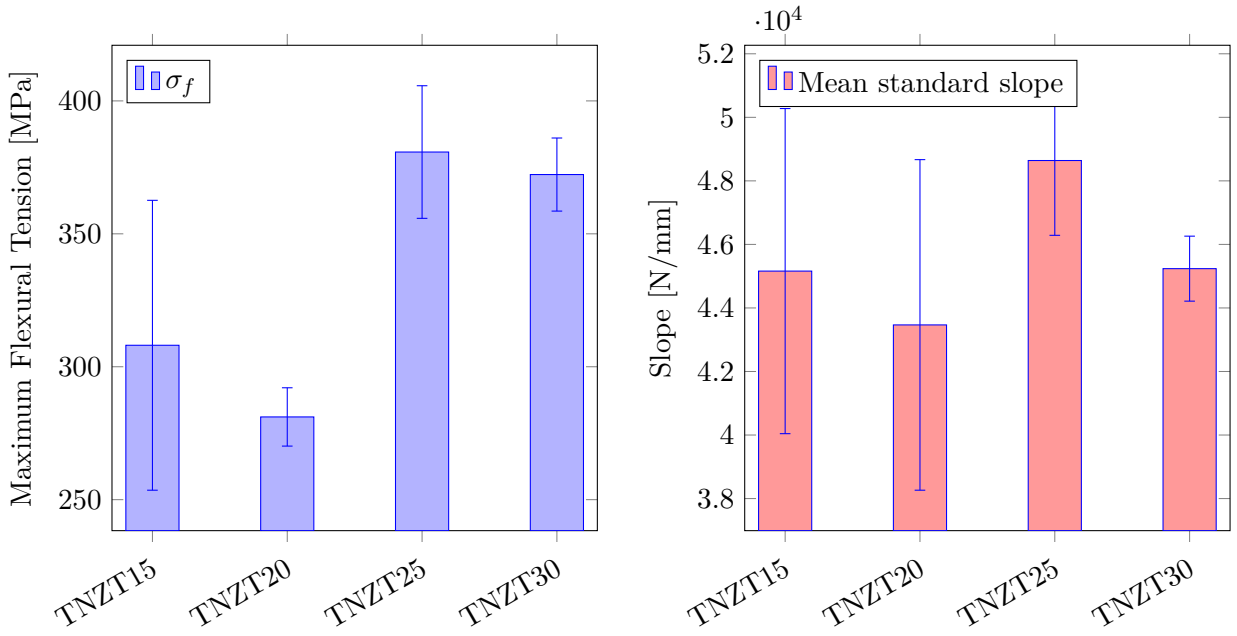

(a) Maximum flexural tension.

(b) Standard Slope.

Figure 4.4: Results of three point flexural test realized on 3 samples per composition - (a) Mean maximum flexural tension - (b) Mean standard slope computed for pressures between 80 and 200 N/mm2.

Based on the findings shown in Table 4.5, crucial details, such as the maximum flexural stress (σ_f) and the highest force the samples could endure, offer direct insights into the flexural strength

of the material. The standard slope, representing the gradient of the initial linear segment of the load-deflection curve, provides further information about the material's stiffness in its elastic domain. Examining the results illustrated in Figure 4.4 (a) and (b), a directly proportional relationship emerges between the flexural strength of the alloys (σ_f) in Figure 4.4a and their stiffness in Figure 4.4b. Analyzing this figure further reveals the influence of the tantalum concentration on both properties. Despite the trend not being linear, two distinct categories can still be discerned. Alloys with a 15 and 20 $\%_{at}$ tantalum concentration exhibit generally lower flexural stiffness (308.08 - 281.12 N/mm^2) compared to their 15 and 20 $\%_{at}$ counterparts (380.77 - 372.3 N/mm^2). Given the apparent correlation between σ_f and flexural stiffness, this observation can be logically extended to the latter.

Tensile Strength and Ductility

The tensile properties of the investigated alloy are then analyzed and presented hereby. The tensile test or traction test provides critical insights into the mechanical behavior of metals under an applied load. Thus, revealing key parameters such as ultimate tensile strength and elongation, as it will be discussed below. The results of this widely used test are fundamental for understanding the performance and suitability of the material for specific applications. Two metrics will be used to characterize the tensile behavior of the material. First, the ultimate tensile strength, which is the maximum load in MPa that the material can withstand before yielding. In addition, it is possible to quantify the plastic behavior of the material by measuring the elongation at rupture (AR%). It is expressed as the percentage of elongation or reduction in the cross-sectional area and provides information about the material's ability to undergo plastic deformation without failure. The AR% values in this section are calculated as shown in Equation 4.1.

$$AR[\%] = \frac{L_f - L_0}{L_0} \times 100\% \tag{4.1}$$

Where L_f is the final length of the specimen at rupture, and L_0 is the original length of the specimen (before applying any tensile load).

	TNZT15	**TNZT20**	**TNZT25**	**TNZT30**
σ_{UTS} [MPa]	141,17 (SD=8,8)	100,28 (SD=18,8)	194,08 (SD=16,1)	171,97 (SD=18,2)
Mean AR%	3,00 (SD=3)	1,18 (SD=0,7)	0,94 (SD=2,4)	-1,00 (SD=1,1)

Table 4.6: Ultimate tensile strength and elongation at rupture computed on three (TNZT15-25-30), and four points (TNZT20).

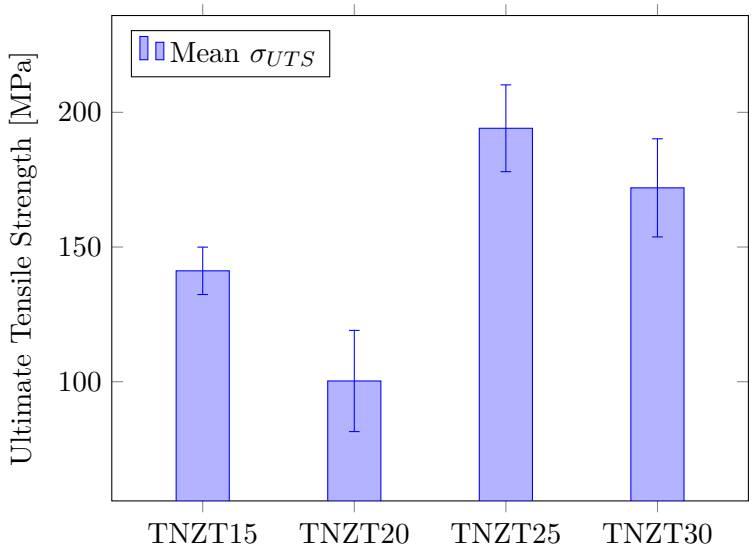

Figure 4.5: Evolution of Ultimate Tensile Strength (UTS) with Ta concentration calculated on 3 specimens per alloy.

4.2.2 Micro and Macro-scale Hardness

In the following section, the results of two measurements of the hardness are presented. First, hardness was measured on a macroscale using a Rockwell HR15T indentometer with an applied force of 147 Newton. Tree specimens were tested for each alloy, performing five measurements on two of their faces labeled as S1 and S2, where S1 and S2 are, respectively, facing upwards and downward during the compression phase and undergoing normal stress. A concise statistical analysis was conducted on these results. The statistical results are presented as a boxplot displaying the mean value of the population as a dark horizontal line, the mean value as a red dot, the lower and upper quartile as the limit of the grey box, and finally, the minimum and maximal values as the extremity of the box. The statistical significance of the findings was assessed using a single-step multiple comparison method, specifically Tukey's HSD test (honestly significant difference). The difference in median hardness values was evaluated with a 95% family-wise confidence level, and the results were illustrated in a pair-wise bar graph. Subsequently, micro-hardness was measured on a microscopic scale by probing between the alloy's pores to obtain an accurate measurement of the material's intrinsic hardness, regardless of porosity. The following sections illustrates these results.

Rockwell Macro Hardness

	TNZT15	**TNZT20**	**TNZT25**	**TNZT30**
Mean Hardness [HR15T]	83,5	83,5	81,3	77,4
Median[HR15T]	83,5	84,8	81,3	78,0
SD [HR15T]	2,4	3,3	2,2	3,1

Table 4.7: Rockwell macro-hardness measurement performed on upper and lower faces of specimens (HR15T-147N applied force).

	Unit	**TNZT15**	**TNZT20**	**TNZT25**	**TNZT30**
Mean Rockwell Hardness	HR15T	83,5	83,5	81,3	77,4
Mean Vickers hardness (HV10)	HV/10	160,8	160,8	147,1	119,2
Mean Vickers hardness	HV	138,7	138,7	128,1	110,9
Mean resistance	MPA	317,7	317,7	212,1	26,1

Table 4.8: Conversion table of Rockwell HR15T hardness values into Vickers hardness.

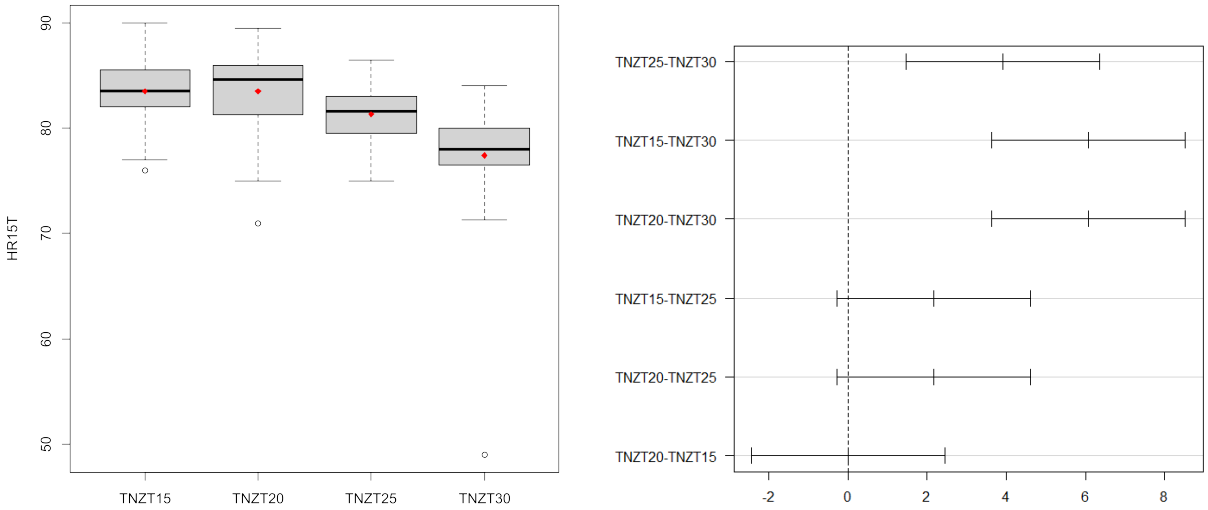

(a) Rockwell's macro hardness (HR15T-147N applied force)

(b) Differences in mean levels of samples (95% family-wise confidence level)

Figure 4.6: Statistical analysis of Rockwell hardness performed on 30 points per alloy formulation.

In conducting Rockwell hardness measurements, three specimens were tested for each alloy composition, with five points measured on both the upward-facing and downward-facing sides. The directions upward and downward correspond to their orientation during compaction. Table 4.7 summarizes the mean and median hardness values. Figure 4.6 (a) presents the statistical analysis of these results. An inverse correlation between hardness and Ta content is suggested, this mean difference is further analyzed in 4.6 (b), where the significance in mean levels between two groups is given with a confidence level 95%. Although it is not possible to conclude that there is a difference in mean value between TNZT15,25 and TNZT20,25 families, a clear difference in hardness mean value is observed overall. It can be stated an undisputable difference in macro hardness between TNZT30 and the rest of the statistical families, with a confidence level of 95%. Additionally, the impact of compression and stress during the compaction phase on the material's hardness was further examined. This involved comparing the hardness values measured on both the downward-facing and upward-facing sides, referred to as S1 and S2 respectively. These findings are presented in Table 4.9, showing an increase in hardness on the face subjected to direct compressive stress during pressing, except for the alloy with the highest Ta concentration. However, this minimal hardening may not be relevant, and the TNZT30 MEA alloy even shows an opposite behaviour, reducing its hardness by 2,34% in the meantime.

	TNZT15	**TNZT20**	**TNZT25**	**TNZT30**
S1 mean hardness	82,67 (SD=2,84)	80,97 (SD=3,3)	80,17 (SD=1,96)	78,33 (SD=2,29)
S2 mean hardness	84,33 (SD=2,13)	86,03 (SD=2,41)	82,03 (SD=1,77)	76,5 (SD=5,04)
Percentual hardening referred to S1	2,01%	6,25%	2,32%	-2,34%

Table 4.9: Comparison of mean Rockwell hardness (HR15T-147N applied force) between the downward (S1) and upward-facing sides (S2) during compaction.

Vickers Micro-hardness

	TNZT15	TNZT20	TNZT25	TNZT30
Number of points	15,5	14,5	14,3	13,4
promedio	370,5	350,8	253,3	219
Median	**421**	**364**	**254**	**202**
sd	163,4	145,3	121,2	115,1

Table 4.10: Micro-hardness measurements in HV measured with Vickers indentometer.

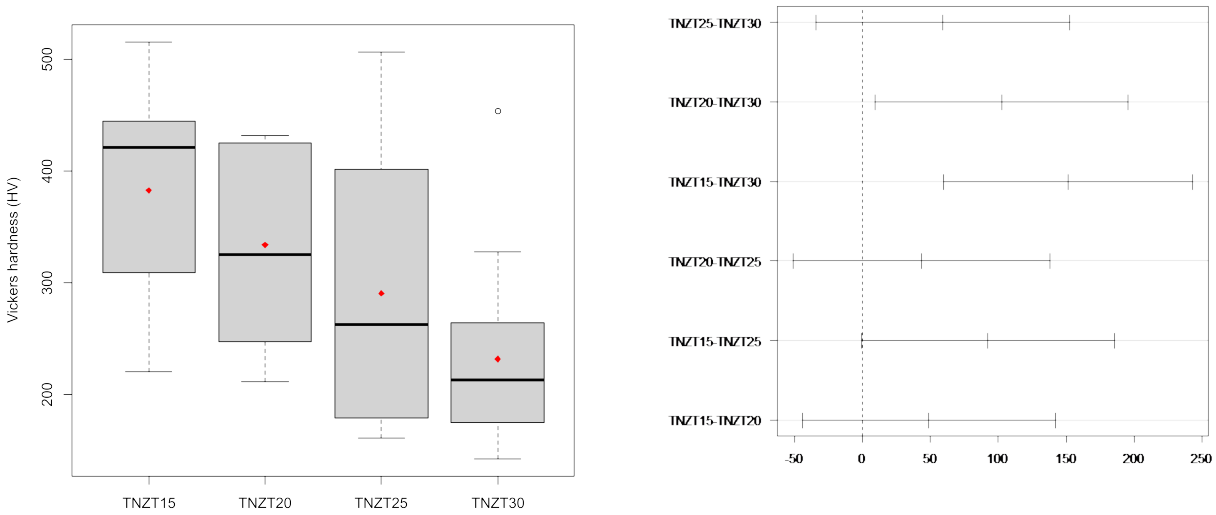

(a) Vickers microhardness

(b) Differences in mean levels of samples (95% family-wise confidence level)

Figure 4.7: Statistical analysis of Vickers microhardness (15 measures per composition).

During this experiment, between 13 and 15 measurements were made on the top side of the specimen. Certain points were excluded because of the print's shape. These excluded measurements exhibited a star-like pattern, likely caused by an internal pore beneath the surface, leading to a corner of the indentometer penetrating further into the material. With this being said, a clear correlation between Ta concentration and the micro-hardness can be observed. According to Figure 4.7 (a) and Table 4.10, the hardness decreases linearly from 370.5 HV to 219 HV as the Ta concentration increases from 15%$_{at}$ to 30%$_{at}$. The significance of this difference in average hardness is further examined in Figure 4.7 (b), where a distinct difference in hardness between 15 and 30%$_{at}$ is found with a 95% confidence level.

4.3 X-Ray Diffraction Results

The following section presents the results of the XRD analysis conducted on the four TNZT formulations. XRD is a widely used method for probing a material's crystallographic properties and providing detailed insights into its atomic-level structure. XRD patterns facilitate the identification of crystal phases, the evaluation of phase composition, and the analysis of structural changes such as crystal strain. XRD analysis allows for the detailed characterization of the crystal structure and the determination of phase purity. In this study, diffraction patterns are processed and interpreted using 'Maud' software for XRD analysis. The subsequent section outlines the key findings and sheds light on the crystallographic features of the material, and on the potential defects or distortions.

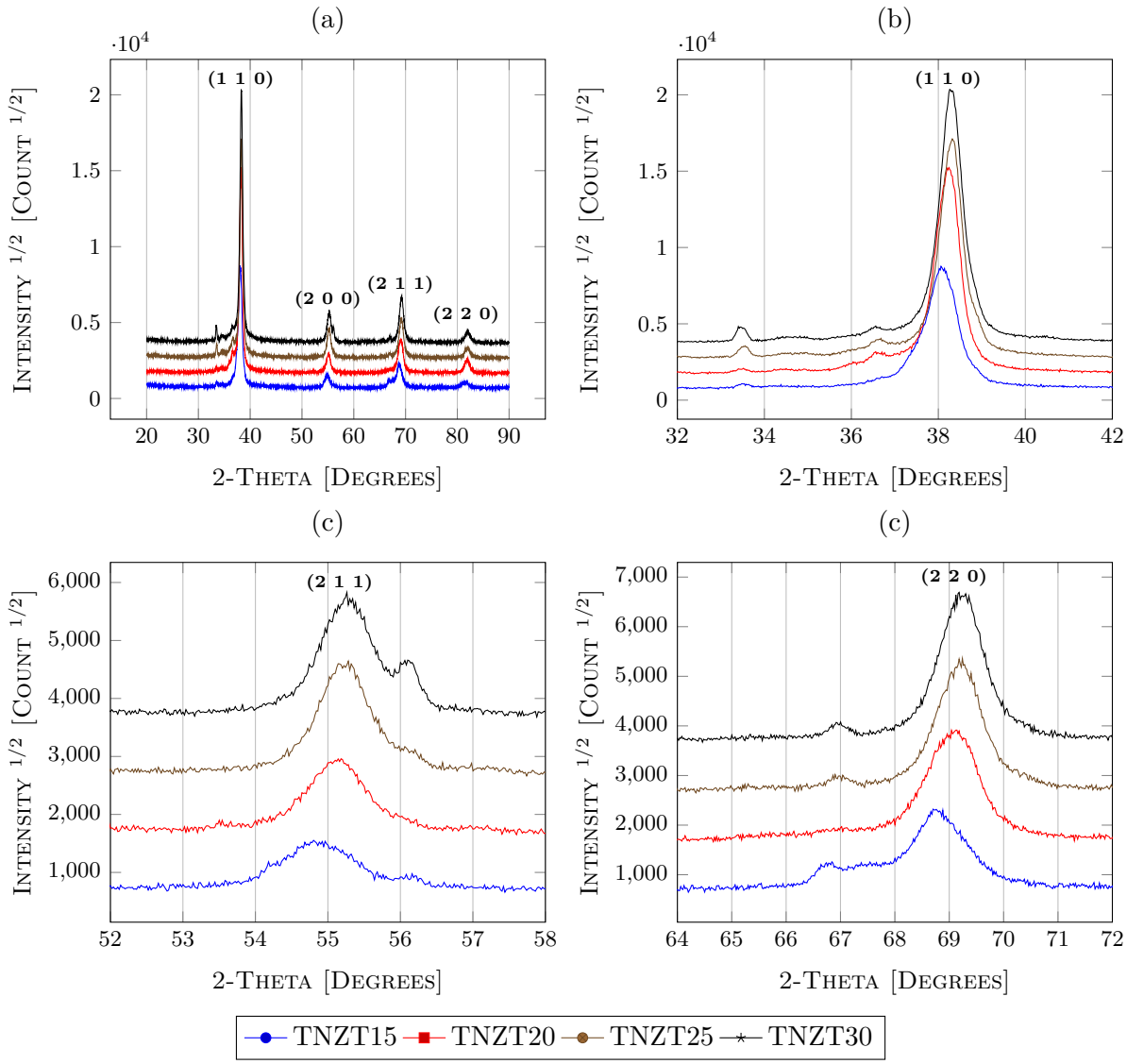

Figure 4.8: XRD results - (a): Full diffraction pattern of the four synthesized TNZT alloys between 20 and 90° angle showing principal cubic diffraction planes - (b): Diffraction plane (1 1 0) centered around 38,14 and 38,22° - (c): Diffraction plane (2 1 1) centered around 55,04 and 55,16° - (d): Diffraction plane (2 2 0) centered around 68,93 and 69,09°.

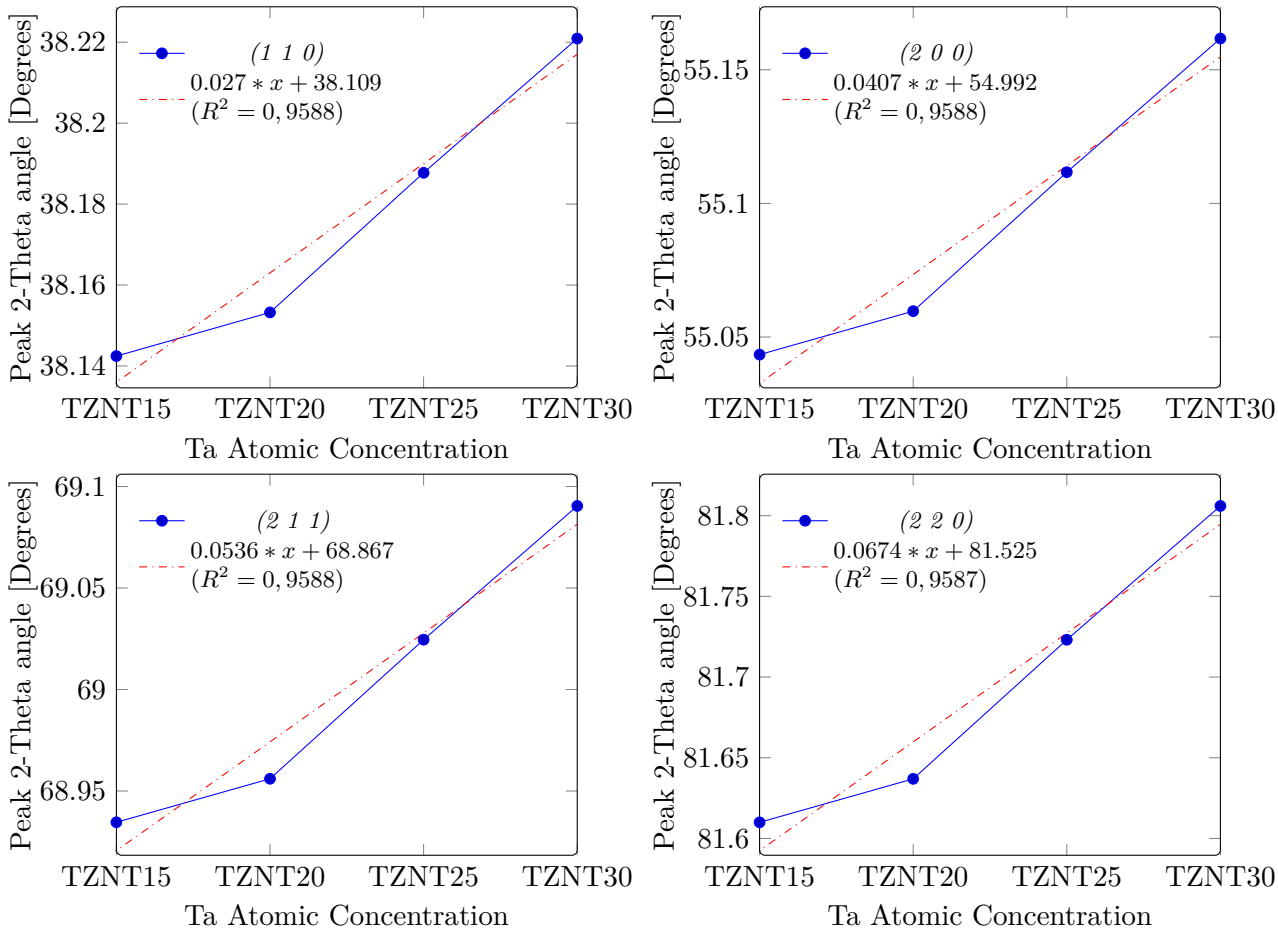

Figure 4.9: Peak displacement of the BCC phase with Ta concentration - Top left: Peak (1 1 0) displacement - Top right: Peak (2 0 0) displacement - Bottom left: Peak (2 1 1) displacement - Bottom right: Peak (2 2 0) displacement.

Figure 4.8 (a) to (d) illustrates the main diffraction peaks corresponding to the primary Ti body-centered cubic (BCC) diffraction plane as a function of Ta concentration. It can be observed that, overall and for each peak, there is a shift towards higher angles. The relationship between the Ta content in the alloy and peak displacement is more clearly depicted in Figure 4.9, where the exact angle of each peak was plotted against increasing atomic percentages of Ta in the Ti-Zn-Nb matrix from 15 to 30 $\%_{at}$. The graphical results demonstrate a linear correlation for each diffraction plane between the tantalum content and the peak displacement. As the concentration increases, the angle shift appears to be greater. The red linear regression coefficient in the four regressions of Figure 4.9 indicates the rate of angular shift for each of the four main atomic planes as a function of Ta concentration. According to Bragg's law, a shift towards higher angles signifies a reduction in the spacing between crystalline planes. This phenomenon could be caused by a contraction of the BCC phase or an increase in its microstrain. Given that Tantalum has a comparable or larger atomic radius relative to the other elements in the alloy, a higher concentration of Ta would typically result in an expansion of the BCC phase. Hence, we propose that the observed effect may instead be primarily attributed to increased microstrain.

Furthermore, at the highest concentrations in Ta, a clear doubling of peak (1 0 1), (2 1 1)-BCC is observed. For the lower concentrations, this effect is made less obvious and the convolution of an intense peak with an other one less intense results in a peak broadening. It is hypothetized that the peak doubling was due to the formation of a second BCC phase of distinct parameters. This plausible hypothesis is supported by the theoretical framework and thermodynamic simulation of the equilibrium state, which guide us to consider the existence of two distinct BCC phases, which will be explored further in Section 5. Additional insights can be derived from the diffractograms. It is known that the relative height of a peak is directly correlated with the weight percentage of the corresponding phase in the sample. Therefore, by examining Figure 4.8.c, it can be anticipated that the separation into two BCC phases increases with the Tantalum concentration. This is evidenced by the emergence of a second peak at higher angle values, resulting in peak doubling. A comparable observation can be observed for the (1 0 0) peak of the HCP phase at approximately 33.5° in Figure 4.8.b, where a significant rise in peak intensity with higher Ta concentrations suggests an increase in HCP fraction.

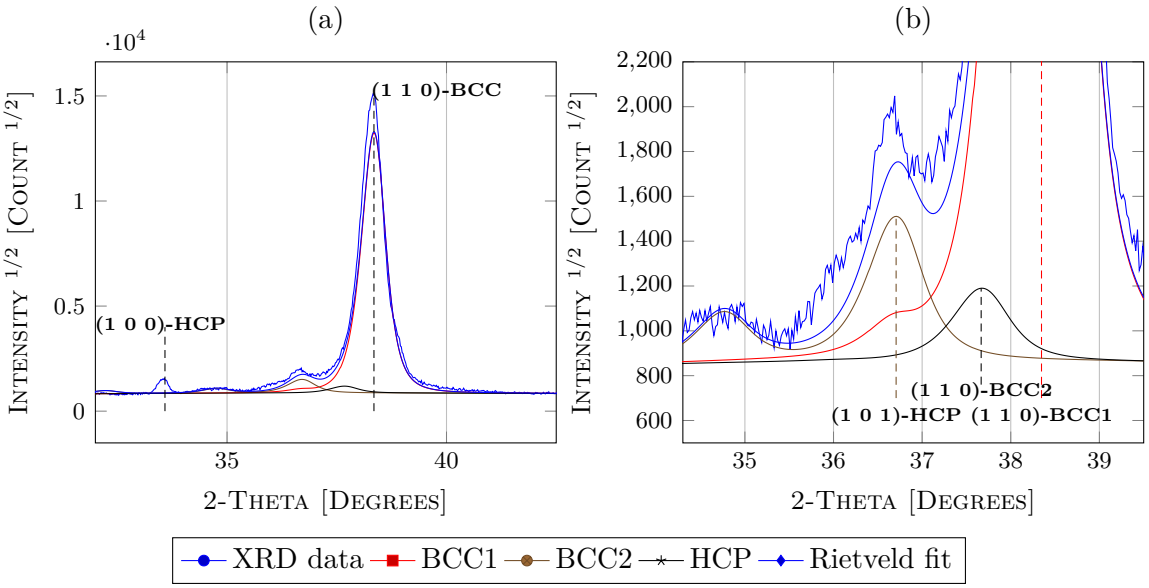

Figure 4.10: Rietveld analysis result of TNZT25 - (a): Fitted results showing presence of phase BCC and HCP - (b): Detail of the 38.2°-centered peak deconvolution.

To quantify the fraction of each phase, a Rietveld analysis is typically performed. This technique allows for the quantification of phases along with their properties, including their parameters, lattice strain, and lattice occupancy. The analysis aims to minimize the squared error between the experimental data and the fitted values, optimizing entry variables such as the crystalline parameters, the microstrain, or the phase fraction. Unfortunately, due to the significant overlap of the peak among the suspected BCC1 and BCC2 phases and the HCP phase, no definitive phase quantification results could be achieved. In Rietveld analysis, preliminary knowledge or estimation of the phases and their parameters is essential to achieve convergence of the results. Consequently, the findings of previous studies were used to provide the algorithm with initial conditions, ensuring that it could converge to a solution. Using the results of the Rietveld analysis of [Al Hawajreh et al., 2023] on a TNZT alloy powder of the same composition and

prepared under nearly identical conditions, the deconvolution of one of TNZT25 peak into its three constituent phases was proposed as shown in Figure 4.10.b. This figure highlights the presence of three phases and underscores the challenge of achieving reliable analysis results due to the overlap of the peaks of these three phases.
In summary, a higher concentration of Ta appears to result in greater segregation into two BCC phases and an increased proportion of the HCP phase. Moreover, the findings suggest that increasing the Ta concentration leads to a higher microstrain within the BCC phase. .

4.4 EBSD Micrography Results

This section presents the findings from an electron backscatter diffraction (EBSD) analysis conducted on our material specimens. EBSD is a powerful microscopy technique widely used to investigate the crystallographic properties and microstructures of materials at the microscopic level. EBSD allows for detailed characterization of grain orientations, grain boundaries, and crystallographic textures by analyzing electron diffraction patterns. This EBSD analysis intends to provide a better understanding of grain structures, grain size distribution, and crystallographic orientations across the sample.In pursuit of this goal, the results obtained from the EBSD were interpreted using the AZtec software, developed by Oxford Instruments. The main findings derived from this investigation are presented subsequently.

4.4.1 Phase Content

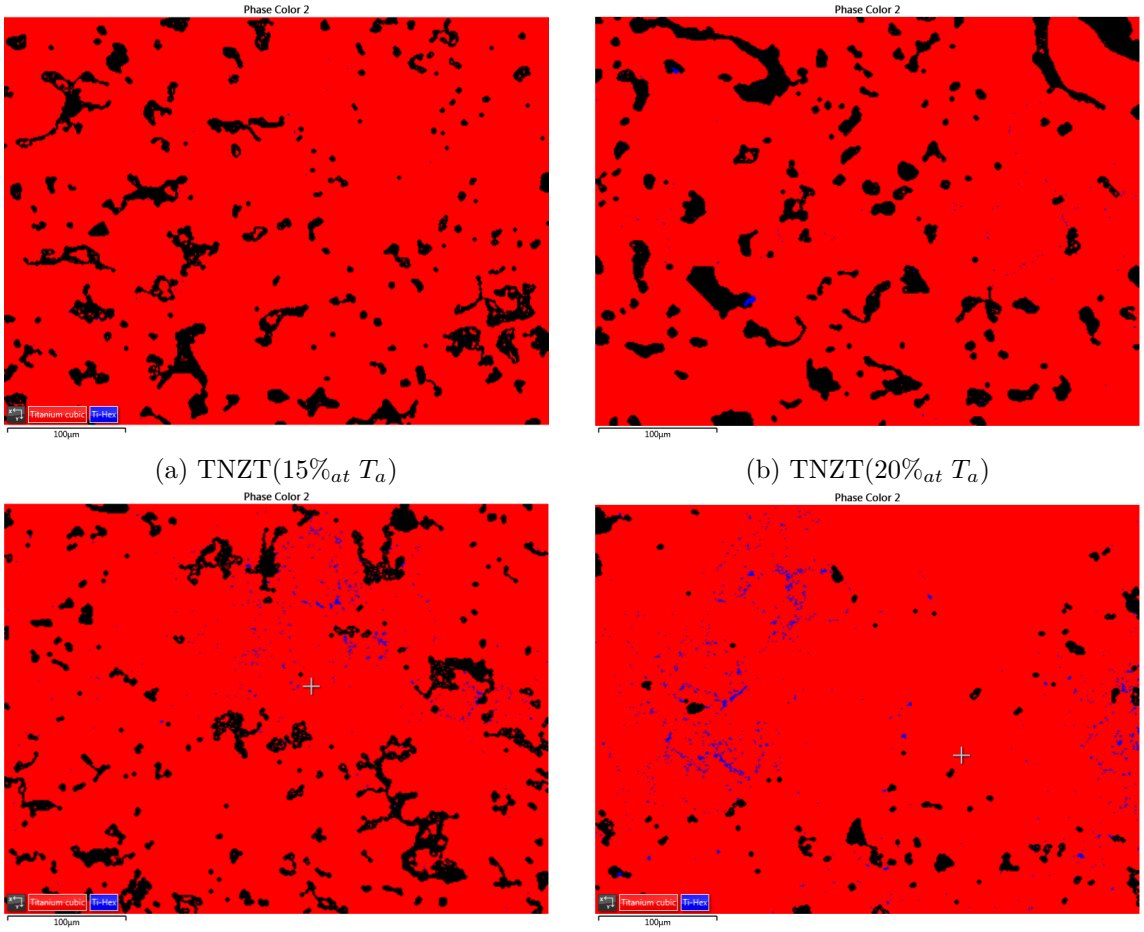

(a) TNZT(15%$_{at}$ T_a)

(b) TNZT(20%$_{at}$ T_a)

(c) TNZT(25%$_{at}$ T_a)

(d) TNZT(30%$_{at}$ T_a)

Figure 4.11: Phase analysis result by electron back-scattered diffraction microscopy (EBSD).

Phase	**TNZT15**	**TNZT20**	**TNZT25**	**TNZT30**
Ti-BCC	89,38% (MAD=0,5018)	88,31% (MAD=0,5913)	89,57% (MAD=0,5935)	96,28% (MAD=0,4667)
Ti-HCP	0,02% (MAD=1,1783)	0,11% (MAD=0,7856)	0,44% (MAD=0,8069)	1% (MAD=0,7404)
Zero Sol.	10,6%	11,58%	9,99%	2,72%

Table 4.11: Evolution of α Ti-BCC (red) and β Ti-HCP (blue) phase proportion with Ta atomic concentration.

Phase	**TNZT15**	**TNZT20**	**TNZT25**	**TNZT30**
Ti-BCC Concentration Accounting for porosity	99,98%	99,88%	99,51%	98,97%
Ti-HCP Concentration Accounting for porosity	0,02%	0,12%	0,49%	1,03%

Table 4.12: Evolution of α Ti-BCC (red) and β Ti-HCP (blue) phase proportion with Ta atomic concentration corrected and accounting for Zero Solution porosity.

This section outlines the changes in phase content as Ta concentration increases. It is important to mention that prior to conducting the phase analysis, the AZtec program must be provided with the elemental composition of the alloy and the expected lattice geometry groups. The results depicted in Figure 4.11 reveal a dual-phase quaternary alloy, predominantly made of a Ti-cubic centered phase (represented in red in the figure), with a minor inclusion of a compact Ti hexagonal phase (shown in blue), which appears to increase proportionally with higher Ta concentration. The increase in Ti-HCP phase with Ta concentration is summarized in Table 4.11, where a slight but steady increase in Ti-HCP concentration is observed, from 0,02%$_{Sup}$ (15 %$_{at}Ta$) to 1,00%$_{Sup}$ (30 %$_{at}Ta$). One of the metrics used to measure the accuracy of the results is the MAD number, or "Mean Angle Deviation". This number indicates the misfit between the measured and the calculated angles between Kikuchi bands; therefore, the larger the MAD value, the higher the misfit, and the lower the indexing confidence. MAD value can therefore be seen as a confidence index and used as such. It is often accepted that a MAD value superior to one indicates a poorly constrained EBSD measurement and a low confidence level. The results of the phase analysis show an acceptable MAD value, between 0,47 and 0,78 except for the concentration of Ti-HCP in TNZT15 (MAD = 1,1783), which can be attributed to the insufficient size of the statistical sample on which the analysis is performed (0, 02% of the sample surface).

In a second time, the following hypothesis was stated: *"All zero solutions result are assimilated to porosity"*. This hypothesis aligns with the FSD observation in Figure 4.15, although the total surface of zero solutions seems to be slightly overestimated compared to visible porosity on the FSD view. Table 4.12 takes this hypothesis into account and shows the result of the phase analysis, considering the alloy as a pure dual phase and removing the effect of porosity. From this table it can be stated that when considering porosity in phase content analysis, the influence of tantalum concentration on the β phase fraction is entirely negated within the examined Ta concentration range of 15 to 30 %$_{at}$.

4.4.2 Grain Geometry and Grain Orientation Distribution

Color Map

This section presents the results of the EBSD analysis, focusing on the color mapping representation of the data. These maps depict individual grains colored according to their crystallographic orientations, aiding the identification of grain boundaries, texture, and grain size distribution within the material. This analysis can provide a deeper understanding of how the material is deformed, recrystallized, and undergoes phase transformations. This representation results directly from Kikuchi's diffraction lines analysis, and is broadly used in research thanks to its clear and visual representation of the data.

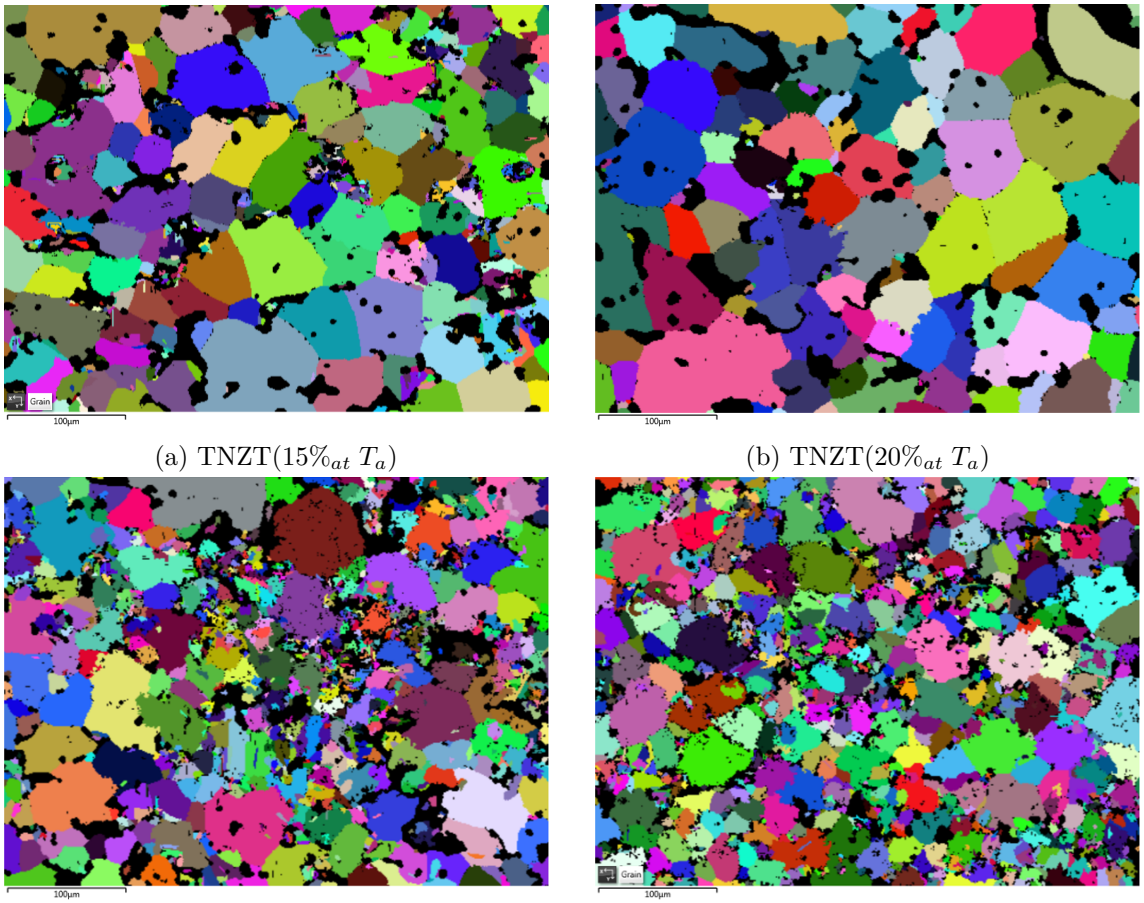

(a) TNZT(15%$_{at}$ T_a)

(b) TNZT(20%$_{at}$ T_a)

(c) TNZT(25%$_{at}$ T_a)

(d) TNZT(30%$_{at}$ T_a)

Figure 4.12: Electron back-scattered diffraction microscopy (EBSD) colored by grain (Minimum of 10 pixels per grain and grain detection angle of 10%).

	TNZT15		**TNZT20**		**TNZT25**		**TNZT30**	
	mean	SD	mean	SD	mean	SD	mean	SD
Area(μm^2)	398,94	871,31	998,08	1343,31	133,41	372,48	131,7	280
Aspect Ratio	1,86	0,66	1,76	0,63	1,81	0,61	1,75	0,53
ECD (µm)	15,07	16,78	28,2	21,89	9,15	9,29	9,73	8,55

Table 4.13: Evolution of grain size in μm^2 and of the aspect ratio with Ta atomic concentration (Minimum of 10 pixels per grain and grain detection angle of 10%).

The grain size map results illustrated in Figure 4.12 provide crucial information on the grain size and geometry within each formulation, as well as their development with varying Ta concentrations. Each distinct color indicates a different lattice orientation of the grain, with black representing zero solution, interpreted as porosity according to the latest hypothesis. The grains were identified using a grain detection angle of 10 ° and a minimum count of 100 pixels per grain, according to ASTM E2627 standards. This analysis reveals two key points: first, an evident refinement of the microstructure with increasing Ta concentration and second, a decrease in grain regularity.

Changes in grain geometry and size were quantified by three metrics as shown in Table 4.13: The area, the aspect ratio, and the equivalent circle diameter (ECD). ECD value is usually preferred to the mean area value, since it provides a consistent and standardized way to compare data and apply statistical methods. It is important to note that the mean value of a sample is highly susceptible to extreme variations. Consequently, this metric may not adequately describe a scenario in which the data exhibit a significant spread with large extremes. Additionally, as indicated by the grain area standard deviation values and simple observation, the data do not closely follow a normal distribution. Therefore, relying solely on a statistical approach is inadequate, and one should conjugate the results of Table 4.13 with observations from Figure 4.12.

From the short review above, key findings emerge. Samples whose Ta content is between 15 and 20 $\%_{at}$ show a relatively similar homogeneous microstructure of smooth-shaped grains. The grain boundaries are continuous and do not present major irregularities. Although an increase from 15,07 to 28,2 μm in ECD is observed between 15 and 20 $\%_{at} Ta$, this effect could be due to the AZtec Program interpreting what could be small impurities inside the pores of Figure 4.12 (a) as legitimate grains, therefore contributing to the reduction of the ECD value. In general, TNZT15 and TNZT20 alloys present a similar microstructure, as far as grain size and shape, respectively, presenting an aspect ratio factor of 1,86 and 0,66. For a Ta content of 25 and 30 $\%_{at}$ the situation changes drastically and the ECD value drops, respectively, to 9,15 and 9,73 μm. The microstructure then displays a very inhomogeneous grain size distribution with numerous small grains (only a few μm in diameter) with rough edges. Interestingly, the highest concentration of these small irregular grains coincides with the area where the highest amount of Ti-HCP phase is formed with Ta addition, as illustrated in Figure 4.11. As for grain geometry, the aspect ratio remains almost identical since no lengthening is observed and grain boundary roughness has no effect on this metric.

Pole Figure and Crystalline Orientation

This section brings a valuable insight into the distribution of the different crystalline orientations. Indeed, the pole figure representation in EBSD microscopy offers a comprehensive visual representation of grains' crystallographic orientations within polycrystalline materials. This analysis is often paired with the color map shown in this same section to allow for the identification of orientation relationships, grain orientation distributions, and texture. This section analyses the microstructure patterns and orientation in two different manners. Firstly, a pole figure was created that displays the frequency and distribution, with respect to the normal to the sample surface, of one of the three crystallographic directions for a cubic lattice. In this case, the direction 100 has been chosen by convention. In this representation, X and Y are, respectively, the longitudinal and transverse directions of the specimen. Another metric, known as the multiple of uniform density (MUD), is chosen to quantify the distribution of misorientation angles between neighboring grains within a sample. Therefore, a low local MUD value indicates a predominantly low-angle grain boundary population, indicating a well-textured material. In essence and to summarize, a MUD of 1 indicates randomly oriented grains while a MUD significantly higher is indicative of a a crystalline orientation tendency.

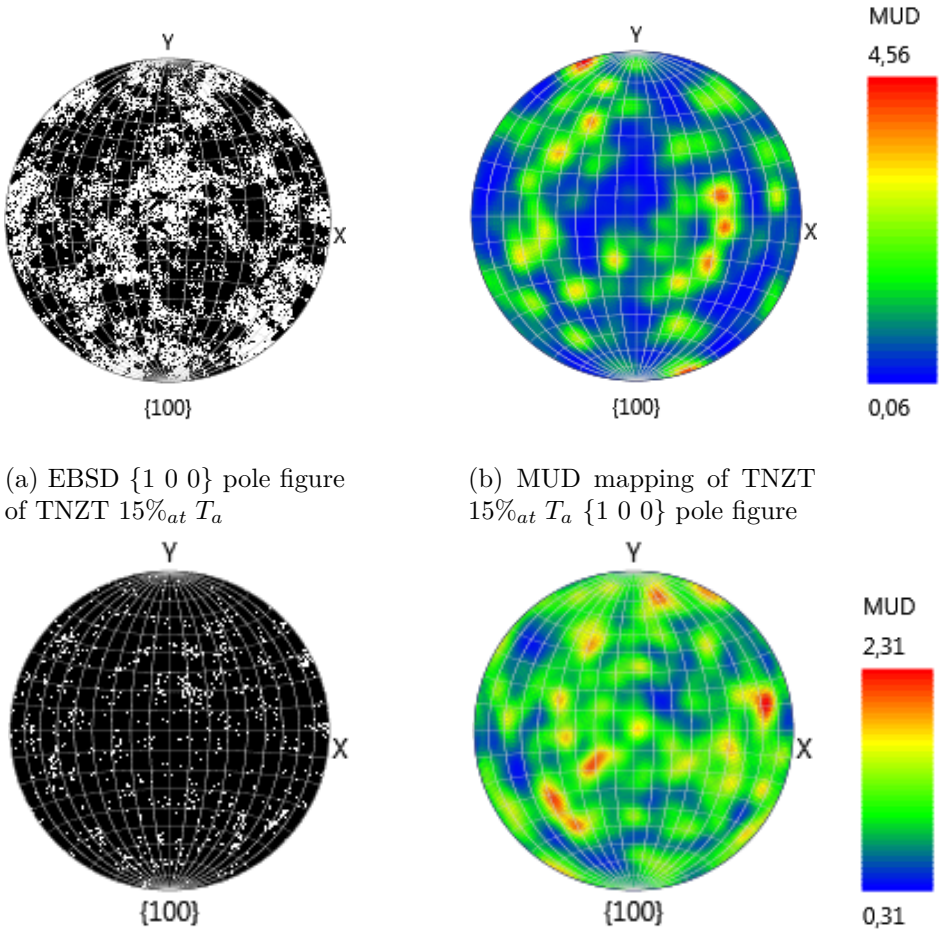

(a) EBSD {1 0 0} pole figure of TNZT 15%$_{at}$ T_a

(b) MUD mapping of TNZT 15%$_{at}$ T_a {1 0 0} pole figure

(c) EBSD {1 0 0} pole figure of TNZT 30%$_{at}$ T_a

(d) MUD mapping of TNZT 30%$_{at}$ T_a {1 0 0} pole figure

Figure 4.13: Inverse Pole Figure (IPF) view.

In the {1 0 0} pole figures, there are no clusters of diffraction points when examined along the x, y, and z (perpendicular to the plane and facing us) Cartesian coordinates. Figures 4.13 (a) and (c) display the pole figure for two different concentrations in Ta, and show great homogeneity in the diffraction directions. Although Figure 4.13 (a) shows much more diffraction points than (c), no preferential direction can be stated and the two samples seem to have an anisotropic grain orientation. This finding can be further elucidated by examining the MUD index of the two pole figures depicted in 4.13 (b) and (d). The MUD values, illustrated on a linear color gradient from blue to red, reveal generally low indices in both samples, with peak values of 4.56 and 2.31 MUD for $15\%_{at}$ and $30\%_{at}$ Ta content, respectively. Although some clusters appear in red, they are few and their intensity remains pretty low. In general, the MUD index is maintained at low values across both samples without clear evidence of structure in the few clusters. This indicates the random nature of the crystalline orientation, with no preferential growth direction.

4.4.3 Elementary Analysis

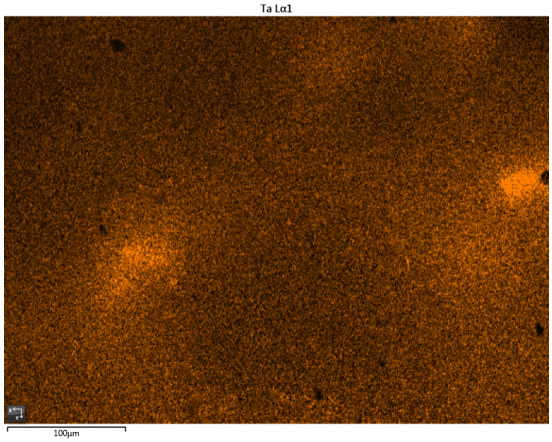

(a) Ta distribution TNZT(15%$_{at}$ Ta).

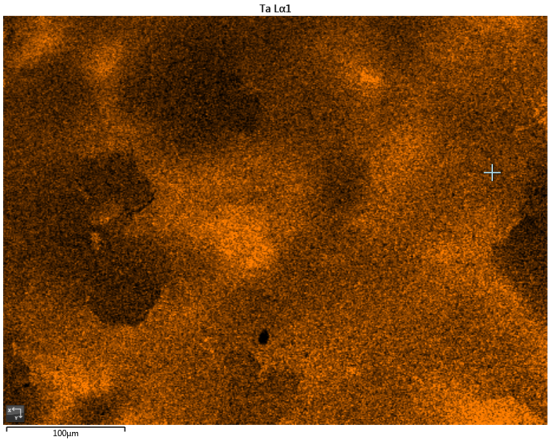

(b) Ta distribution TNZT(30%$_{at}$ Ta).

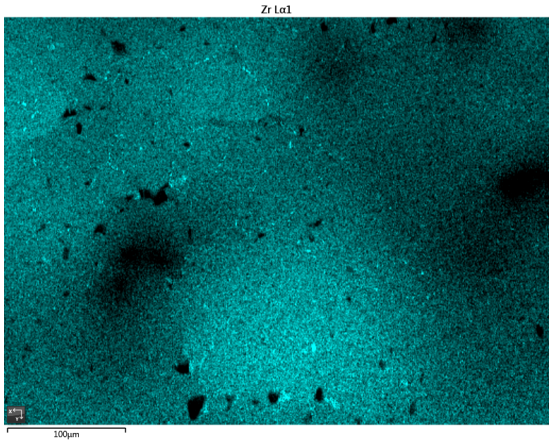

(c) Zr distribution TNZT(15%$_{at}$ Ta).

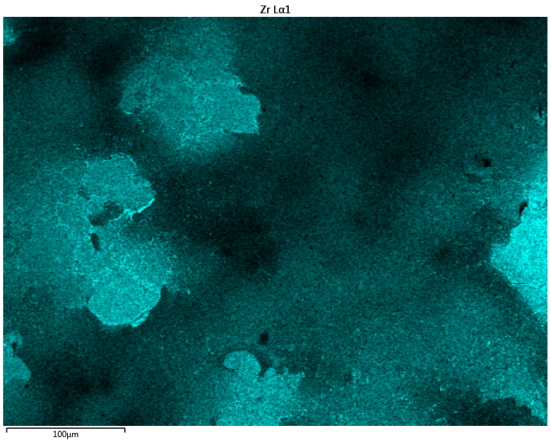

(d) Zr distribution TNZT(30%$_{at}$ Ta).

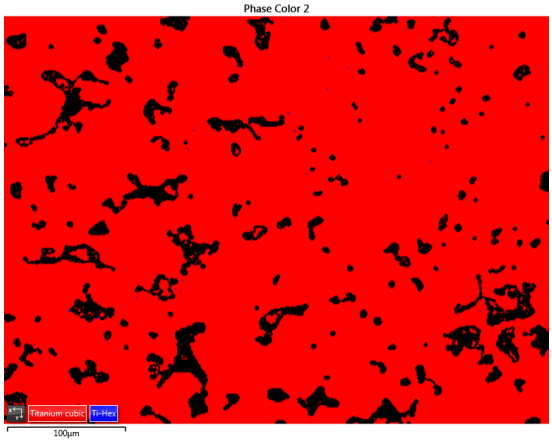

(e) Phase color map TNZT(15%$_{at}$ Ta).

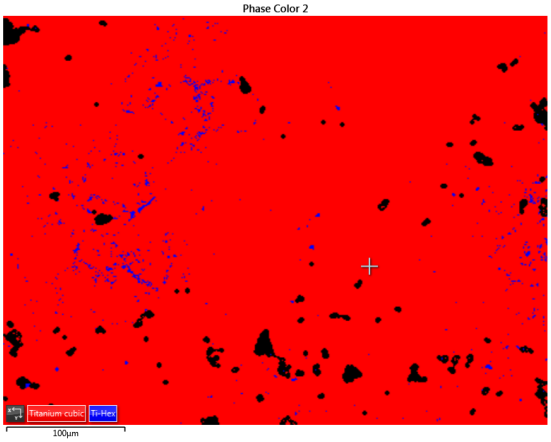

(f) Phase color map TNZT(30%$_{at}$ Ta).

Figure 4.14: Ta and Zr concentration observed by EBSD together with phase color map view for 15 and 30 %$_{at}$ Ta TNZT alloys.

The outcome of the elementary analysis, as depicted in Figure 4.14, offer a perspective on the elemental distribution variations with increasing Ta concentration, and contextualize these findings against the phase content illustrated in Figure 4.14 (c) and (d). In Figures (a) through (d), the pixel's luminosity indicates the concentration of each element within the specified region. Brighter areas correspond to elevated levels of Ta or Zr.

At first glance, a clear inverse correlation is found between the Ta and Zr content. It seems that comparing Figure 4.14 (a) to (c) and (b) to (d), an increase in one's concentration causes a deprivation in the other's. For the lowest Ta concentration of 15 $\%_{at}$, almost no Ti-HCP phase is to be seen, as previously described in the phase analysis section. These results show a homogeneous distribution of Ta and Zr atoms, respectively, as shown in (a) and (c), except for some diffuse areas. These diffuse inhomogeneities could be due to a lack of diffusion during sintering. As Ta concentration reaches the 30 $\%_{at}$ mark, many Ti-HCP grains are scattered across the surface. These micrometric Ti-HCP grains appear to be highly concentrated in Zr. As for the Ta distribution, as mentioned before, highly concentrated Zr areas of the Ti-HCP phase are particularly deprived of Ta, which remains mainly in the cubic-centered phase, where a more inhomogeneous distribution is observed compared to Figure (a).
This section focuses solely on alloys with 15 and 30 $\%_{at}Ta$ concentration. Nonetheless, meaningful conclusions can still be drawn. Specifically, there is a linear and proportional change in the distribution of Ti and Zr relative to the phase content, which is most effectively illustrated in Figure 4.11.

4.4.4 Forescatter Diodes

Figure 4.15 illustrates the view captured by the Forescatter Diodes (FSD). These diodes utilize forescattered electrons to generate well-textured and high-contrast micrographs, which are especially beneficial for examining micro-textures, such as porosity in this case.

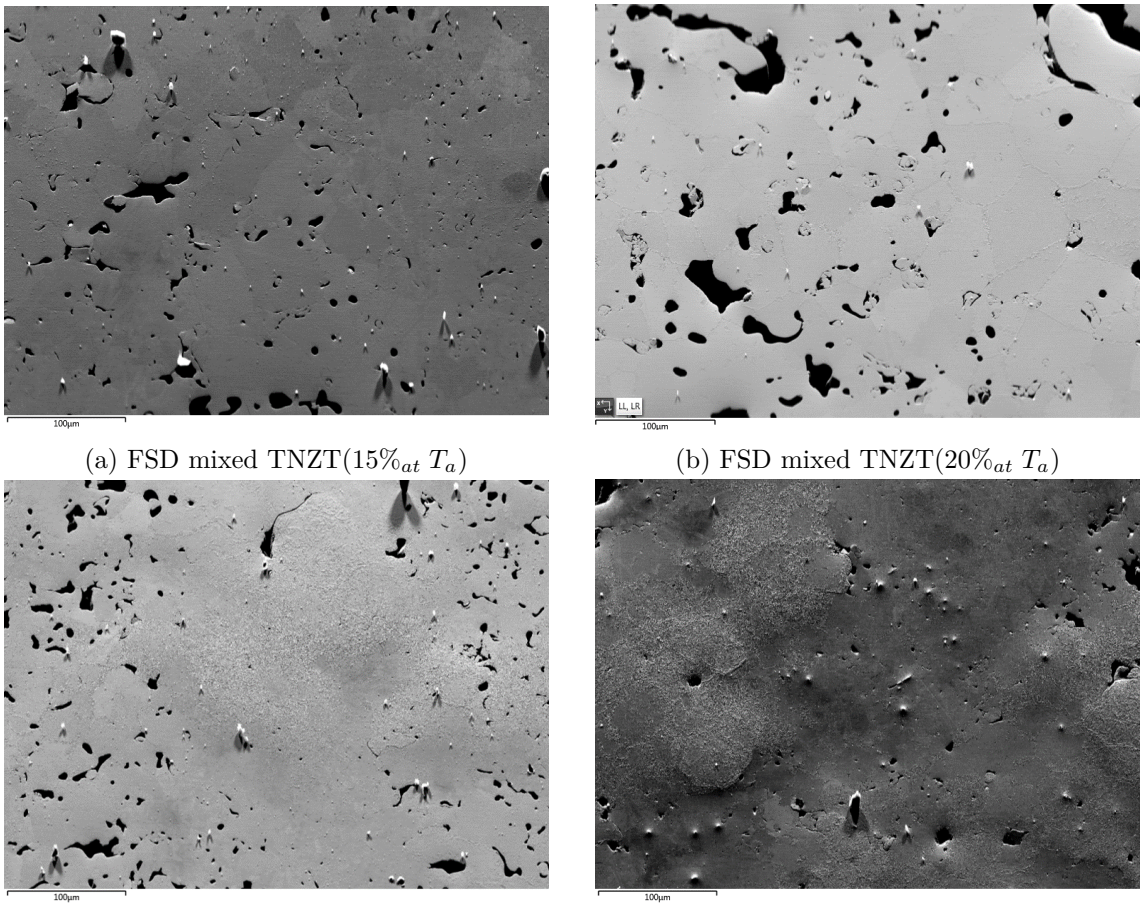

(a) FSD mixed TNZT(15%$_{at}$ T_a)

(b) FSD mixed TNZT(20%$_{at}$ T_a)

(c) FSD mixed TNZT(25%$_{at}$ T_a)

(d) FSD mixed TNZT(30%$_{at}$ T_a)

Figure 4.15: Forescatter diode mixed result by electron back-scattered diffraction microscopy (EBSD).

The forescatter diode examination of the alloy surface provides significant insights into the development of microporosity with varying Ta concentrations, as shown in Figure 4.15. However, since only one observation per sample was performed, the collected data is insufficient for a robust statistical analysis of surface porosity. Nevertheless, at a glance, it appears that increasing the Ta concentration reduces the size of surface pores. Although this conclusion is preliminary due to the limited observations, it can be contextualized by referring to the zero solution results in Table 4.11, which also show a decrease in surface porosity with higher Ta concentrations. It is important to note that the observed surface porosity is what we previously referred to as "closed porosity," because the samples were cut transversely before microscopy. Consequently, these results can also be compared with Figure 4.3, which shows a trend of decreasing internal closed porosity with increasing Ta concentration. Pore size and shape also follow this pattern, with higher Ta content resulting in smaller, more rounded pores.

4.5 Ion Release Test

In the following section, the ion liberation behavior of the TNZT medium-entropy alloy is analyzed when exposed to an organic-like medium simulating physiological conditions. The release of ions in this environment is studied to assess the alloy's biocompatibility and long-term performance post-implantation. This will provide valuable insights into the possible applications as a bio-compatible alloy for future dental or orthopedic implant applications. Hopefully, these analysis results will help us understand how the material behaves in biological systems, which is crucial for developing safer biomaterials for medical use.

	Concentration average $[(ng.L^{-1}.cm^{-2}.h^{-1}]$			
Analyte (Measure Mode)	**TNZT15**	**TNZT20**	**TNZT25**	**TNZT30**
Ta (λ= 268.517 nm)	1,153	2,198	2,819	2,123
Nb (λ= 316.340 nm)	7,693	7,992	8,182	8,183
Ti (λ= 336.121 nm)	1,070	1,746	2,575	4,411
Zr (λ= 343.823 nm)	0,197	1,641	0,788	0,824
Total Ions	10,112	13,577	14,363	15,541

Table 4.14: Result of ion liberation analysis performed by QTEGRA lab on synthetic saliva solution after a 744 hours sample submersion at 25°C.

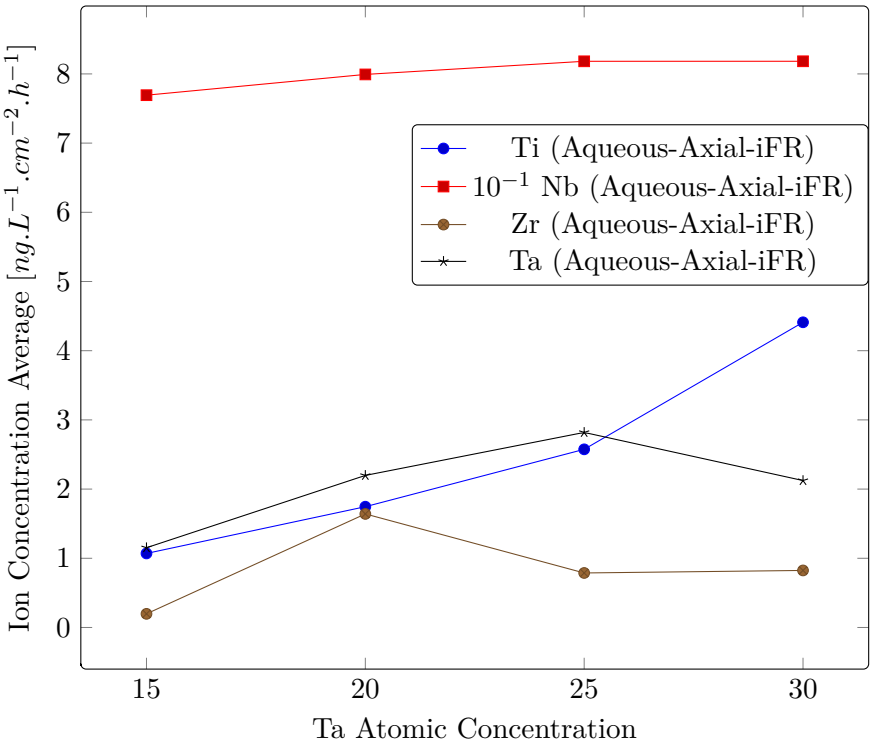

Figure 4.16: Evolution of Ti, Nb, Zr, Ta ion concentration in an organic-like medium (744 hours submersion at 25°C with Ta concentration.

The data presented in Table 4.14 and illustrated in Figure 4.16 demonstrate a direct correlation between the Ta content in the TNZT alloy and the total concentration of released ions. The

concentration of Ti ions in the organic medium at the end of the test increases from 1,070 to 4,411 $ng.L^{-1}.cm^{-2}.h^{-1}$ as the Ta content increases from 15 to 30 $\%_{at}$. In contrast, the concentration of Nb ions remains nearly unchanged with increasing Ta content, despite the fact that its concentration is significantly higher by a factor of ten. Regarding the concentrations of Ta and Zr ions, Figure 4.16 does not reveal any clear direct or inverse trend or correlation.

Chapter 5

Discussion

5.1 Tantalum Concentration as a Parameter for Controlling Porosity and Volumic Changes

5.1.1 Influence of Ta on Porosity and Density

The concentration of Tantalum in equiatomic TNZT MEA could significantly influence the alloy's porosity. For atomic concentrations ranging from 15 to 30 $\%_{at}$, the relative density of the green sample post-pressing decreased as the Tantalum concentration increased, as shown in Figure 4.2. This linear trend demonstrates a clear relationship between Ta concentration and the porosity of green alloys, increasing overall porosity from 10.55% to 17.90% of the ideal alloys' volume, as indicated in Table 4.1. The increase in porosity with higher Tantalum content can be attributed to several factors. One possible reason is the variation in particle sizes; Tantalum particles are the largest in the mixture and may create gaps and voids if not adequately pressed. Another factor is the difference in the elastic modulus between the powders. Tantalum has a Young's modulus of 186 GPa, whereas Titanium only reaches 105 GPa. This disparity in elastic moduli could lead to differential strain in the material, resulting in interstices being formed and increased internal porosity. The concentration of Ta was also observed to influence the type of porosity. A direct relationship was found between the alloy concentration of this element and its external porosity (open pores), resulting in an increase from 8.29% to 17.53% in external porosity, as illustrated in Figure 4.1. Interestingly, in the same figure, the trend for internal porosity appears to be the opposite. Increasing the Ta concentration within the range of 15 to 30 $\%_{at}$ might serve as a parameter to modify and decrease the internal porosity of this type of MEA.

This result is supported by taking a closer look at the material. EBSD analysis, in particular the view of the forescatter diode in Figure 4.15, strengthens this hypothesis. These results show a decrease in the pores' number and size across the four samples and are consistent with Tantalum concentration having a direct influence on the reduction of internal porosity. Furthermore, from this observation, the effect of Tantalum appears to be beneficial in forming well-rounded and homogeneous spherical pores.

5.1.2 Influence of Ta on Volumic Changes After Sintering

An expansion of sintered alloys was observed in the complete range of compositions. It was found that increasing the concentration of Tantalum resulted in greater expansion during sintering. This can be attributed to two distinct causes. Firstly, the increase in overall porosity with Ta content, as shown in Figure 4.1. Although this may partly explain the phenomenon, the MEA still shows an expansion and a decrease in density with higher Ta, as shown in Figure 4.2, even when porosity is considered. Another explanation for volumetric expansion might be the different phase compositions among the four alloys. Although the Tantalum content initially appears to increase the beta BCC phase fraction, once porosity is taken into account, the results of the EBSD analysis indicate an almost perfectly uniform beta phase in all alloys, as evidenced in Table 4.12. Hence, it can be inferred that the primary reason for the observed volumetric expansion is the enlargement of the Beta-Ti lattice formed during the sintering process. This hypothesis is corroborated by the results of the XRD analysis, where a peak shift is observed to the higher angle values corresponding to the β phase, signaling an expansion of the BCC phase with increased tannin concentration (Figures 4.8 and 4.9).

5.2 On The Influence of Tantalum Concentration on Microstructure and Mechanical Properties

5.2.1 Influence of Ta on Microstructural Changes

It was found that all the developed MEAs with Ta concentrations between 15 and 30 $\%_{at}$ showed an almost perfectly uniform $\beta - Ti$ phase with very little presence of the hexagonal compact phase $\alpha - Ti$, respectively, in red and blue in 4.12. Once porosity was taken into account, the results of Table 4.12 show that an increase in Tantalum, a stabilizing element β, had little to no impact on the content of the BCC phase in this concentration range, only reducing it by 1,01%. Arguably, an increase in Ta concentration from 15 to 30$\%_{at}$ led to a marginal increase in the phase content of $\alpha - Ti$, from 0, 02% to 1, 03%. Although this first observation suggests that an almost ideal solid solution of beta Ti was obtained independently of the concentration of Ta, it seems that it led to a lack of diffusion and inhomogeneities of composition. Indeed, Figures 4.14 (a) to (d) show that a high concentration of Tantalum leads to some areas being richer in tantalum and poorer in Zr, and vice versa for regions impoverished in tantalum. As a first approach, this could be explained by the low diffusion coefficient of Tantalum, as is commonly recognized in the literature. However, there is a correlation between the depleted areas of Tantalum and enriched in Zr, with the formation of Zr-enriched α HCP phase, in blue in Figure 4.14(e) and (f). This correlation leads consider a second explication of this phenomenon, based on the formation of two BCC phases of distinct compositions, as it will be discussed later in this section.

In addition, it was found that the increase in Ta concentration led to general grain refinement. Figure 4.12 shows this reduction in grain size, roundness, and grain boundary smoothness. This observation is reflected in Table 4.13 where an inverse correlation is established between the equivalent circular diameter (ECD) and the atomic concentration in Ta. Tantalum concentrations between 15 and 20 % exhibited generally smooth grain boundaries, with sizes ranging from 15 to 28.2 μm ECD. Conversely, higher concentrations of Tantalum, between 25 and 30 %, resulted in a decrease in grain size to 9.29 and 8.55 μm ECD, producing very irregular interfaces (Figure 4.12) and the appearance of a nanometric HCP phase (Figure 4.11). The grain orientation was analyzed using an Inverse Pole View (IPF) analysis as shown in Figure 4.13, which revealed no preferential orientation, thereby confirming the formation of randomly oriented phases that contribute to anisotropic properties. Interestingly, nanometric α HCP grains tend to form primarily in Zr-rich and Ta-deficient phases (Figure 5.1).

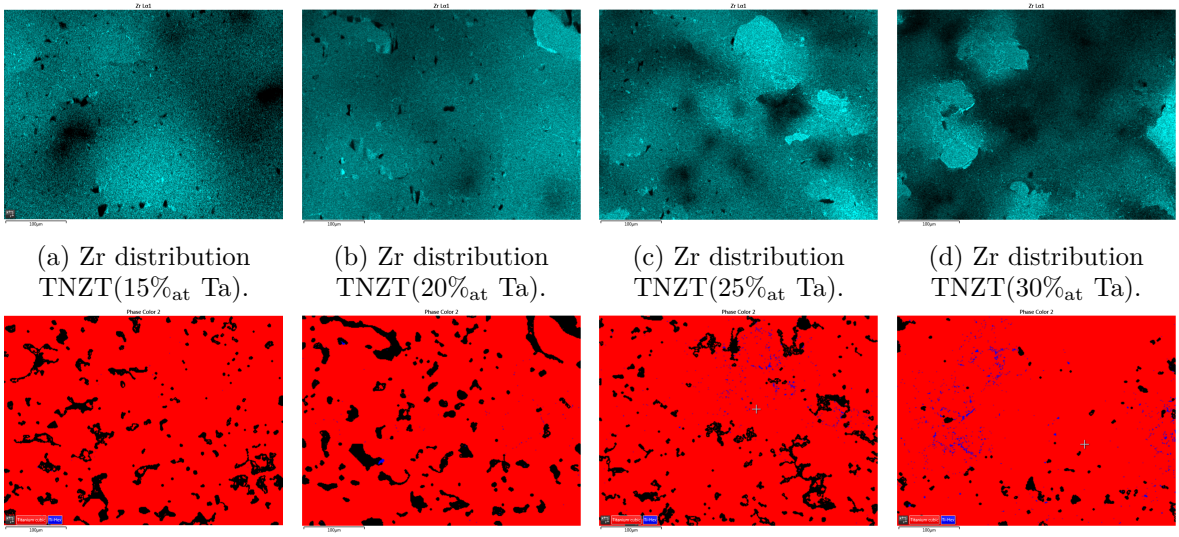

(a) Zr distribution TNZT(15%$_{at}$ Ta).
(b) Zr distribution TNZT(20%$_{at}$ Ta).
(c) Zr distribution TNZT(25%$_{at}$ Ta).
(d) Zr distribution TNZT(30%$_{at}$ Ta).

(e) Phase color map. TNZT(15%$_{at}$ Ta) ($\alpha = 0,02\%$)
(f) Phase color map. TNZT(20%$_{at}$ Ta) ($\alpha = 0,12\%$)
(g) Phase color map. TNZT(25%$_{at}$ Ta) ($\alpha = 0,49\%$)
(h) Phase color map. TNZT(30%$_{at}$ Ta) ($\alpha = 1,03\%$)

Figure 5.1: Zr concentration observed by EBSD together with phase color mapping for 15, 20,25 and 30 %$_{at}$ Ta, in red β BCC, in blue α HFC, pores are shown in black.

This section will discuss the relationship observed between the formation of Ti-HCP phases and the formation of Ti and Zr-rich regions. This phenomenon might be attributed to the alloy maintaining two BCC phases, BCC1 and BCC2, after sintering. Figure 5.2 shows the changes in the thermodynamic equilibrium of the TNZT system for different concentrations of Ta, illustrating an increase in the transition temperature from monophasic to biphasic from 1170 ° C to 1260 ° C as the Ta content increases. As the Ta concentration rises, an increase in the liquidus temperature from 2030 ° C (Figure 5.2.a) to 2090 ° C (Figure 5.2.d) is also observed. This simulation foresees that, upon cooling from high temperatures, the initial monophasic domain decomposes into two phases of BCC, resulting in one phase being richer in Nb and Ta (BCC1) and the other having a higher concentration of Ti and Zr (BCC2), as detailed in Table 5.1 where the chemical composition of the phase was calculated at 1000 ° C. The simulation of the thermodynamic equilibrium of the four formulations shows that the transformation temperature β to α increases with the concentration in Ta. Before this phase transformation, the BCC2 phase reaches an almost binary state, highly concentrated in Ti and Zr while deprived in Ta and Nb. For TNZT30 this transformation was calculated and occurred at 780 ° C between two almost binary phases depleted in Ti and Nb, leading to the following transformation: $\beta(Ti_{43,8}Nb_{5,3}Zr_{48,4}Ta_{2,4}) \rightarrow \alpha(Ti_{43,1}Nb_{0,4}Zr_{56,3}Ta_{0,2})$. This leads to the existence of a theoretical biphasic domain of binary HCP (Ti_xZr_y) and a stable ternary phase of BCC1 ($Ti_{x'}Nb_{y'}Ta_{z'}$) at lower temperatures, as already found in previous studies on this system for similar compositions [Al Hawajreh et al., 2023, p.4357]. While this thermodynamic simulation represents an ideal scenario where diffusion is perfect, it can still offer valuable insights and assist in predicting possible phase transformations during the sintering process.

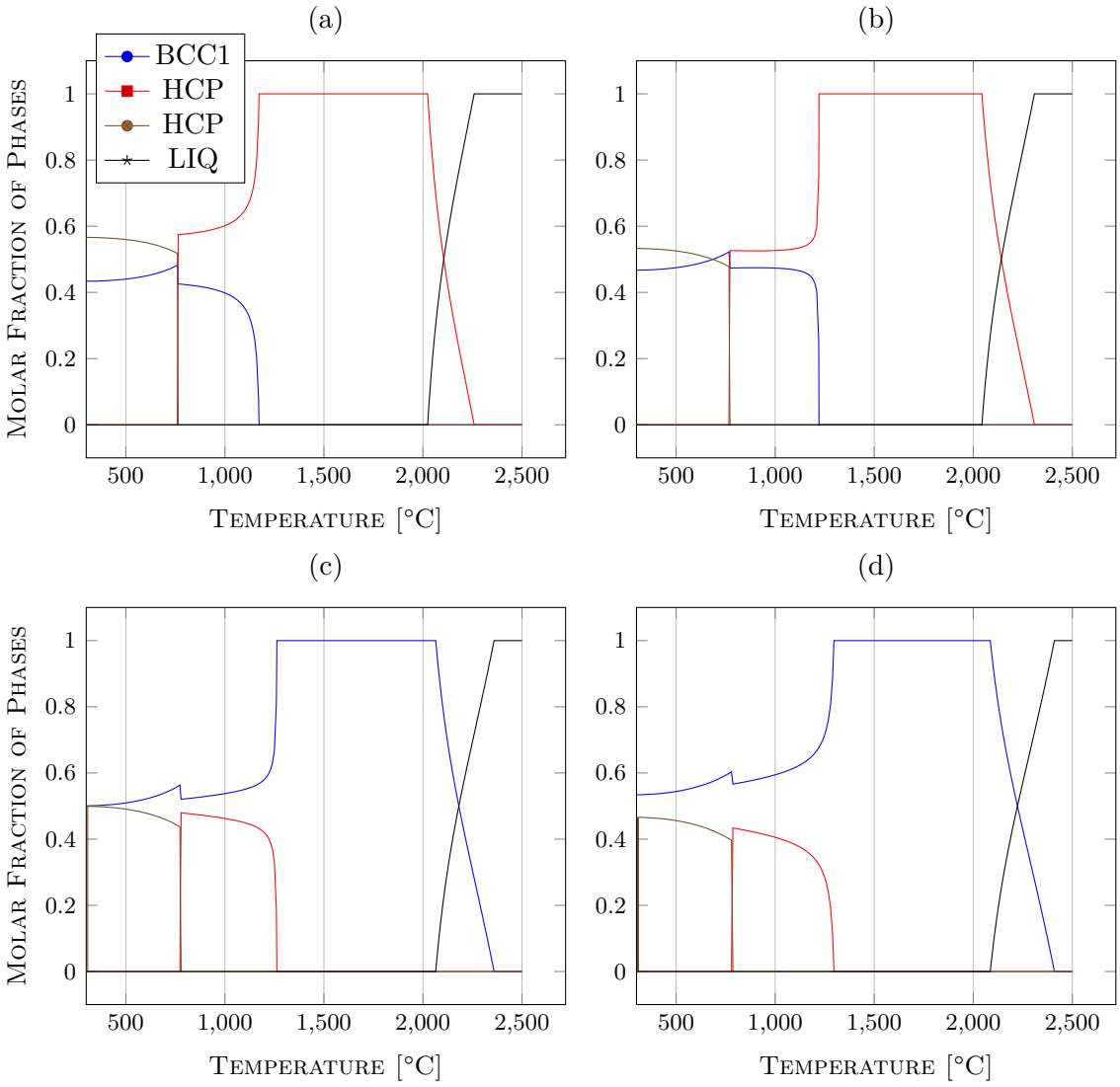

Figure 5.2: Molar fraction of phases obtained by thermodynamic simulation computed between 300 and 2500°C. Simulation result for A) TNZT15 - B) TNZT20 - C) TNZT25 - D) TNZT30

	TNZT15	**TNZT20**	**TNZT25**	**TNZT30**
BCC1	$Ti_{16}Nb_{47}Zr_8Ta_{29}$	$Ti_{16}Nb_{42}Zr_7Ta_{36}$	$Ti_{15}Nb_{37}Zr_6Ta_{41}$	$Ti_{15}Nb_{33}Zr_6Ta_{46}$
BCC2	$Ti_{36}Nb_{16}Zr_{42}Ta_6$	$Ti_{36}Nb_{13}Zr_{44}Ta_6$	$Ti_{36}Nb_{11}Zr_{47}Ta_6$	$Ti_{36}Nb_9Zr_{49}Ta_6$

Table 5.1: Phase molar fraction at equilibrium determined by thermodynamic simulation computed at 1000°C.

The transformation from BCC2 (enriched with Ti and Zr) to an HCP phase could explain the observed correlation between the Zr-enriched regions and the presence of micrometric HCP grains formed in Figure 5.1, as well as the general refinement of the grain structure associated. Higher Ta concentrations seem to result in increased retention of the BCC2 phase, as indicated by the elemental analysis in Figure 5.1 where the Zr-enriched regions seems to increase proportionally

to Ta content. Furthermore, these results are supported by Figure 4.8.c, showing the emergence of a secondary BCC peak with the Ta concentration.
Furthermore, part of this phase appears to have transformed, explaining the presence of HCP in BCC2-rich areas in TNZT25 and TNZT30. Increasing the Ta concentration appears to increase the proportions of the BCC2 retention and HCP phases as suggested by the EBSD and XRD results. The presence of multiple phases, including BCC1 and BCC2, leading to the formation of micrometric Ti-HCP grains, likely also contributes to microstructural refinement by creating more interfaces that hinder grain growth. This could account for the relationship between the grain size and the concentration in micrometric β Ti grains.

5.2.2 Consequences on Mechanical Properties

As expected, the grain refinement observed with the increase in Ta (Table 4.13) is correlated with an increase in tensile and flexural ultimate strength as demonstrated in Figure 5.3. The enhancement of these mechanical properties might be attributed to the effects of the Hall-Petch mechanism resulting from the grain refinement induced by the increased Ta content. The correlation between reduced grain size and improved mechanical characteristics is a well-known phenomenon in polycrystalline materials and has been widely researched. This refinement was found to lead to an overall improvement in yield strength, hardness, creep rate, and fatigue behavior of mild steels [Armstrong, 1970]. This comes as a consequence of Hall Petch's law, which describes the evolution of a material's yield strength with grain size. A dramatic increase in strength is usually observed when refining the microstructure, due to an increase of the density of grain boundaries leading the propagation of dislocations to slow down. However this strengthening effect shows its limits on a nanometric scale when the grains pass below a critical size (10 nm), leading to an inverse effect of grain softening [Voyiadjis and Yaghoobi, 2019, chap.1].

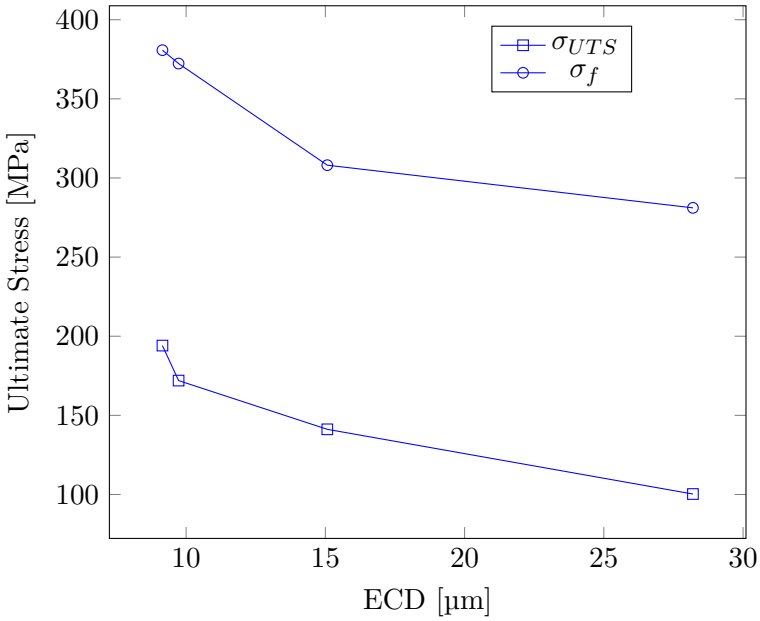

Figure 5.3: Evolution of tensile and flexural ultimate strength with the grain equivalent circular diameter (ECD).

Moreover, it should be noted that, all synthesized alloys exhibited a clean and brittle fracture profile after tensile and flexural tests. This suggests a low plasticity range and predominantly elastic behavior. Several factors could contribute to this limited plastic behavior. The atomic mismatch denoted δ in the literature, due to the different atomic radii of the constituting elements (Ti (147 p.m.), Nb (207 p.m.), Zr (160 p.m.), and Ta (220 p.m.)) has been cited to cause lattice distortion and serve as a dislocation blocker [Nguyen et al., 2019]. Furthermore, the presence of nanometric HCP grains along with internal pores may also act as stress concentration sites, facilitating crack propagation, leading to fragile fractures before the material reaches its yield strength and undergoes plastic deformation [He et al., 2018].
While an increase in Ta concentration leads to grain refinement, Figure 4.6 shows a decrease in superficial hardness. This finding contradicts the theoretical expectations for polycrystalline materials, as mentioned in [Armstrong, 1970, p.9], where the empirical data suggests that a material's hardness typically increases with microstructure refinement. This result is further investigated in Figure 4.7 by performing a microhardness characterization, pinching between the pores to remove the incidence of external porosity on the results. The results show that hardness decreases linearly from 370,5 to 219 HV with the Ta concentration increasing from 15%$_{at}$ to 30%$_{at}$. Meanwhile, the internal porosity decreases from 2.26% to 0.37% as shown in Table 4.2. On the other hand, a slight reduction in the elasticity modulus was noted (Figure 4.3). Previous research on the TZNT system indicates that the elastic modulus has a minimal correlation with porosity [González-Guillén et al., 2023]. Hence, it appears that the observed decrease in hardness and Young's Modulus cannot be attributed to an increase in internal porosity or grain size. This implies that the observed softening and reduction in elastic modulus might be primarily due to alterations in the intrinsic properties of the BCC phase with its Ta content, rather than porosity and microstructural characteristics.

5.3 Potential Effects of Ta on Biocompatibility

The data in Table 4.14 summarizes the ion concentration of each element for all four synthesized TNZT alloys, measured in $ng.L^{-1}.cm^{-2}.h^{-1}$. To assess the relevance of these results, they will be compared to the known toxicity thresholds of the different elements. The toxicity of Nb^{5+}, Zr^{2+} was studied, among others, in [Caicedo et al., 2008]. In this study, it was found that among all the metallic ions studied, Cobalt and Niobium were the most toxic metals. The results in Table 4.14 show that mainly Nb ions were formed during the ion release test. Nb^{5+} and Zr^{2+} ions were measured respectively at 8,57-10,18 and 0,33-1,00 $.10^{-3}$ ppm, which is well below the 5 mM threshold over which DNA damage was induced and viability decreased under 50% [Caicedo et al., 2008]. The release of Nb ions was also below the nontoxic concentration of 172 $\mu g.L^{-1}$ established by [Li et al., 2010]. The concentration of Ti ions from 1,26 to 5,52 $.10^{-3}$ ppm, increasing with the concentration of Ta, was substantially less than the 5ppm threshold, above which it showed inhibition in cell proliferation [Liao et al., 1999]. Finally, the Ta concentration was assessed. Oxidized Tantalum has very low toxicity and it is not surprising that the observed ion concentration (1,26 to 2,62 $.10^{-3}$ ppm) fell far below the dose of 8000 mg/kg, under which no toxicity was found after oral ingestion by rats [Bard et al., 1985]. The results showed a slight increase in total ion release with the Ta fraction, despite the Tantalum's corrosion resistance and passivation behavior. A more detailed analysis may explain this. As shown in Figure 4.16, while the increase in Ta concentration did not affect the final concentrations of Zr and Nb ions, it did cause a rise in the Ti^{4+} ion concentration, increasing from 1.07 to 4.411 $ng.L^{-1}.cm^{-2}.h^{-1}$. Meanwhile, the concentration of Tantalum ions increased at a comparable rate (from 1.153 to 2.819 $ng.L^{-1}.cm^{-2}.h^{-1}$), and then decreased when it reached 30 $\%_{at}$ of Ta (2.123 $ng.L^{-1}.cm^{-2}.h^{-1}$). A possible explanation lies in the difference in redox potential between Ti and Ta. Tantalum is in oxidation state (OS) 5, while Titanium exists in OS = 4 and OS = 5 for different potentials and pH levels. Based on the experiment conditions and potential-pH diagrams for titanium-water and tantalum-water systems, Titanium is more likely to reach OS 5. The oxidation half-reactions in aqueous solution (pH=6.38) are shown in Equations 5.1 and 5.2 with their standard oxidation potentials.

$$OS:\ 0 \rightarrow +4 \qquad Ti \Leftrightarrow Ti^{4+} + 4.e^{-} \quad E^{o} = -1,63V \tag{5.1}$$

$$OS:\ 0 \rightarrow +5 \qquad Ta \Leftrightarrow Ta^{5+} + 4.e^{-} \quad E^{o} = -0,63V \tag{5.2}$$

These potentials would need to be corrected for pH by using Nernst's equation to reflect the effect of protons' concentration on the electrochemical reaction. The reduction potential observed for Tantalum under these conditions is greater than that of Titanium. Hence, it is plausible that Tantalum served as the cathode, causing the anodic corrosion of Titanium. The impact of this anodic corrosion appears to increase with higher concentrations of Ta, resulting in more Ti ions being released into the solution, despite the alloy's overall reduction in the Ti content. This increase in Ta seems to be also correlated with the amount of the Ta-enriched and Ti-deficient BCC phase, as illustrated in Figure 5.1. This hypothesis, despite the lack of academic support, suggests that the increased segregation into the BCC1 (Ta-enriched) and BCC2 (Ti-enriched) phases as the Ta concentration rises could be one reason for Titanium's preferential oxidation, by creating a galvanic couple within the two phases.

Conclusion And Prospects

By the end of this study, a homogeneous and randomly oriented BCC phase was achieved across all synthesized TNZT, with minimal HCP phase present at higher Ta concentrations. The addition of Tantalum in the studied concentration range effectively improved the ultimate tensile and flexural strain and led to grain refinement in the microstructure while simultaneously lowering the elastic modulus. The elastic moduli observed at various Ta concentrations (69.32-63.37 GPa) were found to be less than most of the commonly used biocompatible Ti-V-Al alloys. These promising results highlight the role of Tantalum in better adjusting the elastic properties of the TNZT system to that of human bones. The results also demonstrated that tantalum concentration could control porosity type and shape in P&S alloys. Low internal porosity was achieved, decreasing with the Tantalum fraction (2.26-0.37 vol.%), while external porosity increased greatly with higher Ta concentration (8.29-17.53 vol.%), also resulting in more rounded pores. The decrease in stress-concentrating structures such as internal pores, combined with the increase in open porosity, can positively influence implant osseointegration while maintaining the integrity of the material. Several hypotheses were proposed to explain these findings, including particle size mismatch and the influence of sintering parameters, though the origin of this phenomenon could not be fully explained with the current data. In contrast, despite the fact that no tribological tests have been performed, the decrease in hardness from 370.5 to 219 HV, with increasing Ta content, could indicate a deterioration in the wear resistance of the alloys. This negative outcome would typically lead to the release of metallic microparticles, with the adverse effects discussed in this research. Moreover, the ion release behavior was examined, revealing an unexpected phenomenon. Although all alloys tested exhibited corrosion behavior significantly below toxic levels for human health, an interesting observation was made: higher concentrations of released Ti ions were detected in alloys with the highest Ta content, despite the lower Ti content. It was proposed that this phenomenon was due to a galvanic coupling between phases with very different compositions. This hypothesis requires further investigation, and the corrosion behavior of TNZT alloys would benefit from a more detailed characterization of its corrosion rate, passivation behavior, and other electrochemical properties within this Ta concentration range.

From the data gathered in this research, the increase in Ta concentration within the examined range appears promising for the development of these new biomaterials. Despite the encouraging outcomes, the possible adverse effects at higher Ta concentrations mentioned in this work need to be studied further by characterizing the alloys' tribological and electrochemical properties. It is expected that future research on this system will aim to identify the optimal compositional trade-off, and if the results are convincing, proceed with the first in vivo testing.

Bibliography

[Akmal et al., 2021] Akmal, M., Hussain, A., Afzal, M., Lee, Y. I., and Ryu, H. J. (2021). Systematic study of (MoTa) NbTiZr medium- and high-entropy alloys for biomedical implants- In vivo biocompatibility examination. *Journal of Materials Science & Technology*, 78:183–191.

[Akmal et al., 2022] Akmal, M., Seong, H. W., and Ryu, H. J. (2022). Mo and Ta addition in NbTiZr medium entropy alloy to overcome tensile yield strength-ductility trade-off. *Journal of Materials Science & Technology*, 109:176–185.

[Al Hawajreh et al., 2023] Al Hawajreh, G., Gonzalez, G., Romero-Resendiz, L., Vidilli, A., Otani, L. B., and Amigó, V. (2023). Effect of the Ti/Ta ratio on the feasibility of porous Ti25+x-Nb25-Zr25-Ta25-x (X= 0, 5, and 10) alloys for biomedical applications. *Journal of Materials Research and Technology*, 24:4364–4378.

[Armstrong, 1970] Armstrong, R. W. (1970). The influence of polycrystal grain size on several mechanical properties of materials. *Metallurgical Transactions*, 1(5):1169–1176.

[Bard et al., 1985] Bard, A. J., Parsons, R., and Jordan, J. (1985). Standard Potentials in Aqueous Solution.

[Caicedo et al., 2008] Caicedo, M., Jacobs, J. J., Reddy, A., and Hallab, N. J. (2008). Analysis of metal ion-induced DNA damage, apoptosis, and necrosis in human (Jurkat) T-cells demonstrates Ni2+ and V3+ are more toxic than other metals: Al3+, Be2+, Co2+, Cr3+, Cu2+, Fe3+, Mo5+, Nb5+, Zr2+. *Journal of Biomedical Materials Research Part A*, 86A(4):905–913.

[Cantor et al., 2004] Cantor, B., Chang, I. T. H., Knight, P., and Vincent, A. J. B. (2004). Microstructural development in equiatomic multicomponent alloys. *Materials Science and Engineering: A*, 375-377:213–218.

[Cantor et al., 2002] Cantor, B., Kim, K. B., and Warren, P. J. (2002). Novel Multicomponent Amorphous Alloys. *Journal of Metastable and Nanocrystalline Materials*, 13:27–32.

[Chen et al., 2010] Chen, J.-H., Liu, C., You, L., and Simmons, C. A. (2010). Boning up on Wolff's Law: Mechanical regulation of the cells that make and maintain bone. *Journal of Biomechanics*, 43(1):108–118.

[Costa et al., 2019] Costa, B. C., Tokuhara, C. K., Rocha, L. A., Oliveira, R. C., Lisboa-Filho, P. N., and Costa Pessoa, J. (2019). Vanadium ionic species from degradation of Ti-6Al-4V metallic implants: In vitro cytotoxicity and speciation evaluation. *Materials Science and Engineering: C*, 96:730–739.

[F. Ashby, 2011] F. Ashby, M. (2011). Materials Selection in Mechanical Design. Technical report.

[González-Guillén et al., 2023] González-Guillén, C., Kamel, G., Degalez-Duran, E., Klyatskina, E., Naeem, M., Romero-Resendiz, L., Gonzalez, G., and Amigó, V. (2023). The Effect of Ti/Ta Ratio and Processing Routes on the Hardness and Elastic Modulus of Porous TiNbZrTa Alloys. *Materials*, 16:7362.

[Guo et al., 2022] Guo, L., Ataollah Naghavi, S., Wang, Z., Nath Varma, S., Han, Z., Yao, Z., Wang, L., Wang, L., and Liu, C. (2022). On the design evolution of hip implants: A review. *Materials & Design*, 216:110552.

[Hayakawa et al., 2002] Hayakawa, R., Hatano, Y., Fujii, K., Fukumoto, K.-i., Matsui, H., and Watanabe, K. (2002). Surface segregation and oxidation of Ti in a V–Ti alloy. *Journal of Nuclear Materials*, 307-311:580–584.

[He et al., 2018] He, E., Liu, J., Lee, J., Wang, K., Politis, D. J., Chen, L., and Wang, L. (2018). Effect of porosities on tensile properties of laser-welded Al-Li alloy: an experimental and modelling study. *The International Journal of Advanced Manufacturing Technology*, 95.

[Kopova et al., 2016] Kopova, I., Stráský, J., Harcuba, P., Landa, M., Janeček, M., and Bačákova, L. (2016). Newly developed Ti–Nb–Zr–Ta–Si–Fe biomedical beta titanium alloys with increased strength and enhanced biocompatibility. *Materials Science and Engineering: C*, 60:230–238.

[Li et al., 2010] Li, Y., Wong, C., Xiong, J., Hodgson, P., and Wen, C. (2010). Cytotoxicity of Titanium and Titanium Alloying Elements. *Journal of Dental Research*, 89(5):493–497.

[Liao et al., 1999] Liao, H., Wurtz, T., and Li, J. (1999). Influence of titanium ion on mineral formation and properties of osteoid nodules in rat calvaria cultures. *Journal of biomedical materials research*, 47(2):220–7.

[Mathey et al., 2024] Mathey, E., Pelletier, M., Walsh, W., Gall, K., and Carpenter, R. (2024). Implant Strength Contributes to the Osseointegration Strength of Porous Metallic Materials. *Journal of biomechanical engineering*, 146:1–27.

[Miracle and Senkov, 2017] Miracle, D. B. and Senkov, O. N. (2017). A critical review of high entropy alloys and related concepts.

[Nasibi et al., 2020] Nasibi, S., Alimohammadi, K., Bazli, L., Eskandarinezhad, S., Mohammadi, A., and Sheysi, N. (2020). TZNT alloy for surgical implant applications: A systematic review. *Journal of Composites and Compounds*, 2(3):62–68.

[Nguyen et al., 2019] Nguyen, V. T., Qian, M., Shi, Z., Song, T., Huang, L., and Zou, J. (2019). Compositional design of strong and ductile (tensile) Ti-Zr-Nb-Ta medium entropy alloys (MEAs) using the atomic mismatch approach. *Materials Science and Engineering: A*, 742:762–772.

[Nomura et al., 2022] Nomura, J., Takezawa, A., Zhang, H., and Kitamura, M. (2022). Design optimization of functionally graded lattice infill total hip arthroplasty stem for stress shielding reduction. *Proceedings of the Institution of Mechanical Engineers, Part H: Journal of Engineering in Medicine*, 236:095441192210751.

[Polyzois et al., 2012] Polyzois, I., Nikolopoulos, D., Michos, I., Patsouris, E. S., and Theocharis, S. (2012). Local and systemic toxicity of nanoscale debris particles in total hip arthroplasty. *Journal of Applied Toxicology*, 32.

[Ranganathan, 2003] Ranganathan, S. (2003). Alloyed pleasures: Multimetallic cocktails.

[Sidhu et al., 2021] Sidhu, S. S., Singh, H., and Gepreel, M. A. H. (2021). A review on alloy design, biological response, and strengthening of β-titanium alloys as biomaterials. *Materials Science and Engineering: C*, 121:111661.

[Singh et al., 2014] Singh, A., Kumar, N., Dwivedi, A., and Subramaniam, A. (2014). A geometrical parameter for the formation of disordered solid solutions in multi-component alloys. *Intermetallics*, 53:112–119.

[Stejskal et al., 2007] Stejskal, V., Hudecek, R., Stejskal, J., and Sterzl, I. (2007). Diagnosis and treatment of metal-induced side-effects. *Neuro endocrinology letters*, 27 Suppl 1:7–16.

[Tsai et al., 2013] Tsai, K.-Y., Tsai, M.-H., and Yeh, J.-W. (2013). Sluggish diffusion in Co–Cr–Fe–Mn–Ni high-entropy alloys. *Acta Materialia*, 61(13):4887–4897.

[Voyiadjis and Yaghoobi, 2019] Voyiadjis, G. Z. and Yaghoobi, M. (2019). Chapter 1 - Introduction: Size effects in materials. In Voyiadjis, G. Z. and Yaghoobi, M., editors, *Size Effects in Plasticity*, pages 1–79. Academic Press.

[Wang et al., 2020] Wang, X., Guo, W., and Fu, Y. (2020). High-entropy alloys: emerging materials for advanced functional applications. *Journal of Materials Chemistry A*, 9(2):663–701.

[Yeh, 2006] Yeh, J.-W. (2006). Recent progress in high-entropy alloys. *European Journal of Control - EUR J CONTROL*, 31:633–648.

[Yeh et al., 2004] Yeh, J.-W., Chen, S.-K., Lin, S.-J., Gan, J.-Y., Chin, T.-S., Shun, T.-T., Tsau, C.-H., and Chang, S.-Y. (2004). Nanostructured High-Entropy Alloys with Multiple Principal Elements: Novel Alloy Design Concepts and Outcomes. *Advanced Engineering Materials*, 6(5):299–303.

Appendix A

ODS

RELACIÓN DEL TRABAJO CON LOS OBJETIVOS DE DESARROLLO SOSTENIBLE DE LA AGENDA 2030

Este trabajo de fin de máster se alinea con los objetivos de desarrollo sostenible (ODS) de la agenda 2030 que se muestran a continuación en la tabla A.1. El énfasis de este estudio está en el objetivo número 3, que concierne a la salud y al bienestar. De hecho, dado que la esperanza de vida ha incrementado significativamente en los últimos años, la inserción de implantes médicos en jóvenes plantea nuevos retos respecto a las consecuencias a largo plazo de la presencia de materiales extraños, comúnmente metálicos, en el cuerpo. La seguridad a largo plazo de los biomateriales actuales ha sido cuestionada recientemente, revelando posibles efectos adversos para la salud de los pacientes. Incluso en pacientes mayores, en quienes los efectos a largo término son frecuentemente subestimados, los materiales específicos pueden causar reacciones inflamatorias y rechazo de los implantes. Esto conduce a cirugías complejas de reemplazo y representa un riesgo considerable en pacientes ya vulnerables. Este estudio se dedica a evaluar la viabilidad de emplear nuevas aleaciones para implantes y prótesis, con el objetivo de mitigar los efectos perjudiciales de los materiales actuales y, así, mejorar el bienestar de los pacientes. Adicionalmente, este estudio tiene una dimensión innovadora y representa una potencial oportunidad industrial para los laboratorios médicos, permitiéndoles alinearse con el objetivo 9 "Industria, Innovación e Infraestructuras" de los ODS.

Objetivos de Desarrollo Sostenibles	Alto	Medio	Bajo	No Procede
ODS 1. **Fin de la pobreza.**	☐	☐	☐	☒
ODS 2. **Hambre cero.**	☐	☐	☐	☒
ODS 3. **Salud y bienestar.**	☒	☐	☐	☐
ODS 4. **Educación de calidad.**	☐	☐	☐	☒
ODS 5. **Igualdad de género.**	☐	☐	☐	☒
ODS 6. **Agua limpia y saneamiento.**	☐	☐	☐	☒
ODS 7. **Energía asequible y no contaminante.**	☐	☐	☐	☒
ODS 8. **Trabajo decente y crecimiento económico.**	☐	☐	☐	☒
ODS 9. **Industria, innovación e infraestructuras.**	☐	☒	☐	☐
ODS 10. **Reducción de las desigualdades.**	☐	☐	☐	☒
ODS 11. **Ciudades y comunidades sostenibles.**	☐	☐	☐	☒
ODS 12. **Producción y consumo responsables.**	☐	☐	☐	☒
ODS 13. **Acción por el clima.**	☐	☐	☐	☒
ODS 14. **Vida submarina.**	☐	☐	☐	☒
ODS 15. **Vida de ecosistemas terrestres.**	☐	☐	☐	☒
ODS 16. **Paz, justicia e instituciones sólidas.**	☐	☐	☐	☒
ODS 17. **Alianzas para lograr objetivos.**	☐	☐	☐	☒

Figure A.1: Objetivos de desarollo sostenible de la agenda 2023

BUDGET ANALYSIS

Study of the Influence of Tantalum Concentration on Ti-Nb-Zr-Ta Medium Entropy Alloys and Perspectives of Future Developments for Biomedical Applications

GUILLOTIN TITOUAN

Contents

List of Tables

List of Figures

Preamble

The following section presents the results of the budget analysis of this work. In the subsequent chapters, the cost will be calculated considering that this study was led by an engineer hired by a public administration, in this case, the UPV, and sold as a service to another public or private entity.

The costs were divided into material, machine and labor costs. To determine the machinery's hourly cost, estimating its useful life in years and its annual usage was essential. Subsequently, the hourly costs for machinery and manual labor, inclusive of all taxes, were determined and are shown in Table 1.3 and Table 1.1, respectively. Furthermore, the unit cost of each disposable resource, classified as 'material' below, was obtained and is summarized in Table 1.2. It is important to point out that given the many manipulations carried out, it was necessary to neglect and discard some of the electrical costs against other more important expenditures. Therefore, only the electrical consumption cost of the 744h-ion release test and the computer's consumption during the writing and correction phases were taken into account. The energy cost of other manipulations is indeed negligible in comparison. All costs are expressed in euros VAT included, and employers' contribution is included in the case of the labor hourly rate.

Finally, to assess the 'retail price' of this study, the Spanish VAT rate was applied, and the industrial profit margin was accounted for by applying a 6% industrial benefit, as stated by the Spanish "Real Decreto 1098/2001, Art.131" for public administrations. This margin aims to ensure the financial sustainability of the laboratory entity by covering operational costs and enabling investment. Finally, the data were further analyzed to identify the main expenditure sources, as illustrated in Figure 3.1, to more effectively determine cost reduction strategies for future studies.

Chapter 1

Material Equipment And Labor Costs

The next section details the individual costs of materials and equipment, in addition to the hourly labor rates. As stated in the preamble, all unit costs are derived from the retail prices of each item, inclusive of VAT. The hourly rates for all involved personnel, such as engineers, thesis director, or lab technicians, are calculated based on the median gross salaries in Spain, including employer contributions.

Table 1.1: Labour Hourly Rate

Position/Job	**Hourly Rate**
Thesis director	51,81 €/h
Laboratory technician	23,5 €/h
Engineer	31 €/h

Table 1.2: Material List and Unit Cost

Item	**Reference Unit**	**Retail Price**
9pm diamond suspension	Liter (L)	280,00 €
Absorbent paper	metro (m)	0,02 €
Acetone	Liter (L)	3,50 €
Aluminium foil	metro (m)	0,06 €
Artificial saliva Inger-Hartman	Liter (L)	0,70 €
Colloidal silica suspension 0.05 pm	Liter (L)	46,00 €
Conductive Resin	Kilogram (Kg)	48,68 €
Distilled water	Liter (L)	1,75 €
Energy cost	kWh	0,13 €
Ethanol	Liter (L)	5,00 €
Grinding disks	Unit (u)	6,00 €
Hourly elec. cost computer (60W)	Hour (h)	0,01 €
Hourly elec. cost furnace (1500W)	Hour (h)	0,19 €
Hourly elec. Cost Incubator (245W)	Hour (h)	0,03 €
ICP-OEP Laboratory sercices	Sample	50,00 €
Laboratory gloves (pair)	Unit (u)	0,08 €
Milling carbide ends	Unit (u)	8,50 €
Niobium powder	Kilogram (Kg)	1760,00 €
Non-conductive resin	Kilogram (kg)	47,99 €
Parafin tape	metro (m)	0,03 €
Plastic sample bottle	Unit (u)	0,22 €
Polishing pad Bhueler	Unit (u)	100,00 €
SiC sandpaper	Unit (u)	3,00 €
Stainless steel balls	Unit (u)	1,00 €
Struers Long MD polishing pad	Unit (u)	84,00 €
Struers MD Chem polishing pad	Unit (u)	77,00 €
Talcum powder	Kilogram (Kg)	2,50 €
Tantalum powder	Kilogram (Kg)	750,00 €
Titanium powder	Kilogram (Kg)	230,00 €
Zircon tray for sintering	Unit (u)	25,00 €
Zirconium powder	Kilogram (Kg)	250,00 €

Table 1.3: Machine List and Unit Cost

Item	**Retail Price**	**Life Cycle**	**Annual Use**	**Hourly Cost**
	[€]	[years]	[h/year]	[€/hour]
3-axis powder mixer	6500 €	8 y	1500 h/y	0.54 €/h
Arquimedes lab equipment	750 €	8 y	1500 h/y	0.06 €/h
Aztec EBSD software	1400 €	1 y	1800 h/y	0.78 €/h
CNC drilling/milling machine	15000 €	8 y	1500 h/y	1.25 €/h
CNC grinding machine	12000 €	8 y	1500 h/y	1.00 €/h
Compresser (for compressed air)	300 €	8 y	500 h/y	0.08 €/h
Computer OS license	150 €	10 y	1500 h/y	0.01 €/h
Computer with dedicated program	1500 €	4 y	1500 h/y	0.25 €/h
Digital/mechanical caliper	70 €	8 y	1500 h/y	0.01 €/h
Durometer with tools	4200 €	8 y	1500 h/y	0.35 €/h
EBSD microscope	320000 €	12 y	1500 h/y	17.78 €/h
Glove-box	22000 €	8 y	1500 h/y	1.83 €/h
Hydraulic press for green elaboration	45000 €	12 y	1500 h/y	2.5 €/h
Incubator	3200 €	12 y	1500 h/y	0.18 €/h
Laptop Asus Vivobook	1100 €	4 y	1500 h/y	0.18 €/h
Micro-durometer	5500 €	8 y	1500 h/y	0.46 €/h
Polishing machine	25000 €	8 y	1500 h/y	2.08 €/h
Precision scale	400 €	12 y	1500 h/y	0.02 €/h
Resin filler machine	1300 €	8 y	1800 h/y	0.09 €/h
Rotary filing machine	10990 €	8 y	1500 h/y	0.92 €/h
Sintering furnace	65000 €	12 y	1500 h/y	3.61 €/h
Sonelastic lab equipment	5530 €	8 y	1500 h/y	0.46 €/h
Tensile/Flexile test Shimadzu machine	90000 €	8 y	1800 h/y	6.25 €/h
Tensile/Flexural test Shimadzu machine	80000 €	8 y	1800 h/y	5.56 €/h
Ultrasound cleaner	250 €	8 y	1500 h/y	0.02 €/h
Vacuum pump	250 €	8 y	1500 h/y	0.02 €/h
VibroMet 2 polishing machine	10000 €	8 y	1800 h/y	0.69 €/h
XRD diffractometer	59500 €	6 y	1500 h/y	6.61 €/h

Chapter 2

Cost Breakdown Per Study Section

From this initial information, the cost breakdown of the entire study was calculated by dividing it into 7 sections. For reasons of clarity, the sections follow the logical and chronological order of the course of the study. From its early stage of planning to the compilation and presentation of the results.

2.1 Study Planning

Table 2.1: Section One - Study Planning Cost Breakdown

	1 Delimitation and Planning of the study				
		Item	Quantity	Unitary price	Cost
1	Labour	Preliminary research	10 h	31 /€/h	310,00 €
		Study planning	4 h	31 /€/h	124,00 €
		Meeting with tutor	3 h	51,8 €/h	155,40 €
	Equipment	Laptop Asus Vivobook	14 h	0,183 €/h	2,57 €
	Material	Energy cost computer (60W)	14 h	0.00762 €/h	0,11 €
				Section 1 cost	**592,07 €**

2.2 Sample Elaboration

Table 2.2: Section Two - Sample Elaboration Cost Breakdown

	2.1 Powder elaboration				
		Item	Quantity	Unitary price	Cost
2.1	Equipment	Glove-box	4 h	1,83 €/h	7,33 €
		3-axis powder mixer	1 h	0,54 €/h	0,54 €
		Precision scale	4 h	0,02 €/h	0,09 €
	Material	Titanium powder	0.037 Kg	230 €/Kg	8,43 €
		Niobium powder	0.071 Kg	1760 €/Kg	125,03 €
		Zirconium powder	0.070 Kg	250 €/Kg	17,45 €
		Tantalum powder	0.148 Kg	750 €/Kg	110,87 €
		Parafin tape	2 m	0,03 €/m	0,06 €
		Plastic sample bottle	20 u	0,22 €/u	4,40 €
		Laboratory gloves (pair)	2 u	0,08 €/u	0,17 €
		Stainless steel balls	20 u	1 €/u	20,00 €
	Labour	Laboratory technician	4 h	23,5 €/h	94,00 €
				2.1 Cost	**381,04 €**
	2.2 Powder compaction				
		Item	Quantity	Unitary price	Cost
2.2	Equipment	Hydraulic press for green elaboration	3 h	2,5 €/h	7,50 €
		Digital/mechanical caliper	2 h	0,01 €/h	0,01 €
		Precision scale	1 h	0,02 €/h	0,02 €
		Compresser (for compressed air)	0,25 h	0,08 €/h	0,02 €
	Material	Laboratory gloves (pair)	1 u	0,08 €/u	0,08 €
		Talcum powder	0,005 Kg	2,5 €/Kg	0,01 €
	Labour	Laboratory technician	3 h	23,5 €/h	70,50 €
				2.2 Cost	**78,15 €**
	2.2 Green sintering				
		Item	Quantity	Unitary price	Cost
2.3	Equipment	Sintering furnace	8 h	3,61 €/h	28,89 €
		Vacuum pump	8 h	0,19 €/h	1,52 €
	Material	Elec. cons. furnace (1500W)	8 h	0,02 €/h	0,17 €
		Zircon tray for sintering	1 u	25 €/u	25,00 €
	Labour	Laboratory technician	1 h	23,5 €/h	23,50 €
				2.3 Cost	**79,08 €**
				Section 2 cost	**538,27 €**

2.3 Sample Preparation

Table 2.3: Section Three - Sample Preparation Cost Breakdown

	3.1 Tensile test sample preparation				
		Item	Quantity	Unitary price	Cost
3.1	Equipment	CNC drilling/milling machine	4 h	1,25 €/h	5,00 €
		CNC grinding machine	7 h	1 €/h	7,00 €
		Tensile/Flexile test Shimadzu machine	3 h	6,25 €/h	18,75 €
		Computer with dedicated program	1 h	0,25 €/h	0,25 €
	Material	Grinding disks	2 u	6 €/u	12,00 €
		Milling carbide ends	3 u	8,5 €/u	25,50 €
	Labour	Laboratory technician	14 h	23,5 €/h	329,00 €
				3.1 cost	**397,50 €**
	3.2 Hardness test sample preparation				
		Item	Quantity	Unitary price	Cost
3.2	Equipment	Rotary filing machine	0,7 h	0,92 €/h	0,64 €
	Material	SiC sandpaper	4 u	3 €/u	12,00 €
	Labour	Laboratory technician	1 h	23,5 €/h	23,50 €
				3.2 cost	**36,14 €**
	3.3 XRD and micro-hardness sample preparation				
		Item	Quantity	Unitary price	Cost
3.3	Equipment	Resin filler machine	0,7 h	0,09 €/h	0,06 €
		Rotary filing machine	1,4 h	0,92 €/h	1,28 €
		Polishing machine	1 h	2,08 €/h	2,08 €
		CNC grinding machine	2 h	1 €/h	2,00 €
		Ultrasound cleaner	0,2 h	0,02 €/h	0,00 €
	Material	SiC sandpaper	4 u	3 €/u	12,00 €
		Struers MD Chem polishing pad	1 u	77 €/u	77,00 €
		Struers Long MD polishing pad	1 u	84 €/u	84,00 €
		9pm diamond suspension	0,1 L	280 €/L	28,00 €
		Colloidal silica suspension 0.05 pm	0,3 L	46 €/L	13,80 €
		Ethanol	0,2 L	5 €/L	1,00 €
		Non-conductive resin	0,12 Kg	47,99 €/Kg	5,76 €
		Talcum powder	0,05 Kg	2,5 €/Kg	0,13 €
	Labour	Laboratory technician	5 h	23,5 €/h	117,50 €
				3.3 cost	**344,62 €**

3.4 EBSD Microscopy sample preparation

		Item	Quantity	Unitary price	Cost
3.4	Equipment	Resin filler machine	0,7 h	0,09 €/h	0,06 €
		Rotary filing machine	1,4 h	0,92 €/h	1,28 €
		Polishing machine	1 h	2,08 €/h	2,08 €
		VibroMet 2 polishing machine	1 h	0,69 €/h	0,69 €
		Ultrasound cleaner	0,2 h	0,02 €/h	0,00 €
	Material	SiC sandpaper	4 u	3 €/u	12,00 €
		Struers MD Chem polishing pad	1 u	77 €/u	77,00 €
		Struers Long MD polishing pad	1 u	84 €/u	84,00 €
		9pm diamond suspension	0,1 L	280 €/L	28,00 €
		Colloidal silica suspension 0.05 pm	0,3 L	46 €/L	13,80 €
		Ethanol	0,2 L	5 €/L	1,00 €
		Conductive Resin	0,12 Kg	48,68 €/Kg	5,84 €
		Talcum powder	0,005 Kg	2,5 €/Kg	0,01 €
	Labour	Laboratory technician	6 h	23,5 €/h	141,00 €
				3.4 cost	**366,78 €**

3.5 Ion liberation sample preparation

		Item	Quantity	Unitary price	Cost
3.5	Equipment	Resin filler machine	2 h	0,09 €/h	0,18 €
		Rotary filing machine	4 h	0,92 €/h	3,66 €
	Material	Acetone	0,1 L	3,5 €/L	0,35 €
		SiC sandpaper	4 u	3 €/u	12,00 €
		Talcum powder	0,015 Kg	2,5 €/Kg	0,04 €
	Labour	Laboratory technician	6 h	23,5 €/h	141,00 €
				3.5 cost	**157,23 €**

Section 3 cost	**1302,27 €**

2.4 Mechanical Characterization

Table 2.4: Section Four - Mechanical Characterization Cost Breakdown

	4.1 Elastic modulus ultrasonic characterization				
		Item	Quantity	Unitary price	Cost
4.1	Equipment	Sonelastic lab equipment	2 h	0,46 €/h	0,92 €
		Digital/mechanical caliper	1 h	0,01 €/h	0,01 €
		Precision scale	1 h	0,02 €/h	0,02 €
		Computer with dedicated program	2 h	0,25 €/h	0,50 €
	Labour	Laboratory technician	2 h	23,5 €/h	47,00 €
				4.1 cost	**48,45 €**
	4.2 Density and porosity characterization				
		Item	Quantity	Unitary price	Cost
4.2	Equipment	Arquimedes lab equipment	2 h	0,06 €/h	0,13 €
		Digital/mechanical caliper	1 h	0,01 €/h	0,01 €
		Precision scale	1 h	0,02 €/h	0,02 €
	Labour	Laboratory technician	2 h	23,5 €/h	47,00 €
				4.2 cost	**47,15 €**
	4.3 Rockwell hardness characterization				
		Item	Quantity	Unitary price	Cost
4.3	Equipment	Durometer with tools	3 h	0,35 €/h	1,05 €
	Labour	Laboratory technician	3 h	23,5 €/h	70,50 €
				4.3 cost	**71,55 €**
	4.4 Micro-hardness characterization				
		Item	Quantity	Unitary price	Cost
4.4	Equipment	Micro-durometer	3 h	0,46 €/h	1,38 €
		Computer with dedicated program	3 h	0,25 €/h	0,75 €
	Labour	Laboratory technician	3 h	23,5 €/h	70,50 €
				4.4 cost	**72,63 €**
	4.5 Tensile and flexural test				
		Item	Quantity	Unitary price	Cost
4.5	Equipment	Tensile/Flexural test Shimadzu machine	6 h	5,56 €/h	33,33 €
		Computer with dedicated program	6 h	0,25 €/h	1,50 €
	Labour	Laboratory technician	6 h	23,5 €/h	141,00 €
				4.5 cost	**175,83 €**
				Section 4 cost	**415,61 €**

2.5 Microstructural Characterization

Table 2.5: Section Five - Microstructural Characterization Cost Breakdown

	5.1 XRD Analysis				
		Item	Quantity	Unitary price	Cost
5.1	Equipment	XRD diffractometer	4 h	6,61 €/h	26,44 €
	Labour	Laboratory technician	3 h	23,5 €/h	70,50 €
				5.1 cost	**96,94 €**
	5.2 EBSD Microscopy				
		Item	Quantity	Unitary price	Cost
5.2	Equipment	EBSD microscope	16 h	17,78 €/h	284,44 €
		Computer with dedicated program	16 h	0,25 €/h	4,00 €
		Aztec EBSD software	3 h	0,78 €/h	2,33 €
	Labour	Laboratory technician	6 h	23,5 €/h	141,00 €
				5.2 cost	**237,94 €**
				Section 5 cost	**334,89 €**

2.6 Ion Release Test

Table 2.6: Section Six - Biochemical Characterization Cost Breakdown

	6 Ion liberation test				
		Item	Quantity	Unitary price	Cost
6	Equipment	Incubator	744 h	0,18 €/h	132,27 €
		Elec. cons. Incubator 36L (245W)	744 h	0,03 €/h	22,97 €
		ICP-OEP Laboratory sercices	12 Sample	50 €/Sample	600,00 €
	Material	Artificial saliva Inger-Hartman	0,6 L	0,7 €/L	0,42 €
	Labour	Laboratory technician	3 h	23,5 €/h	70,50 €
				Section 6 cost	**826,15 €**

2.7 Analysis and Writing

Table 2.7: Section Seven - Analysis and Writing Cost Breakdown

	7.1 Data analysis and interpretation				
		Item	Quantity	Unitary price	Cost
7.1	Labour	Engineer	100 h	31 €/h	3100,00 €
	Equipment	Laptop Asus Vivobook	100 h	31 €/h	18,33 €
	Material	Energy cost computer (60W)	100 h	0.00762 €/h	0,76 €
				7.1 cost	**3119,10 €**
	7.2 Manuscript redaction				
		Item	Quantity	Unitary price	Cost
7.2	Labour	Engineer	200 h	31 €/h	6200,00 €
	Equipment	Laptop Asus Vivobook	200 h	31 €/h	36,67 €
	Material	Energy cost computer (60W)	200 h	0.00762 €/h	1,52 €
				7.2 cost	**6238,19 €**
	7.3 Revision and correction				
		Item	Quantity	Unitary price	Cost
7.3	Labour	Tutor	10 h	51,8 €/h	518,00 €
		Engineer	20 h	31 €/h	620,00 €
	Equipment	Laptop Asus Vivobook	40 h	31 €/h	7,33 €
	Material	Energy cost computer (60W)	40 h	0.00762 €/h	0,30 €
				7.3 cost	**1141,82 €**
				Section 7 cost	**10499,11 €**

Chapter 3

Total Study Cost

The total cost of each section of the study was calcuilated from the previous cost breakdown chapter and were compiled in Table 3.1. Spanish VAT rate of 21% is then applied to this cost, to which it should be added a 6% of industrial Benefit rate, as stated by the "Real Decreto 1098/2001, Art.131" for public institutions.

Table 3.1: Total Study Cost

Study section		**Breakdow cost**
Section 1		592,07 €
Section 2		538,27 €
Section 3		1302,27 €
Section 4		415,61 €
Section 5		334,89 €
Section 6		826,15 €
Section 7		10499,11 €
Total sections		**14508,37 €**
IVA	21%	3046,76 €
IVA included		**17555,13 €**
Industrial benefit	6%	1053,31 €
Benefit included		**18608,44 €**
Total study cost		**18608,44 €**

Discussion

After obtaining the cost that a client would need to pay such a study, the expenditures were further examined through the prism of the type of resource category: material, machin, and labor. These results are presented as a sunburst chart in Figure 3.1, and give a different perspective about the main sources of expenditure during this study. Most costs are attributed to labor (85.8%), with the rest split between equipment and materials, accounting for 8.6% and 5.6%, respectively. The figure offers further details by breaking these categories into the study's primary tasks. Thus, post-treatment and writing represented 87. 3% of labor expenses, while laboratory work comprised only 12. 7 % of these costs. Almost all expenditures on machinery (92.8%) were related to the characterization work carried out in the laboratory. Meanwhile, in terms of material expenses, the majority (61.7%) were due to sample preparation for various characterization methods and only 38% were associated with alloy formulation. After this analysis, it appears clearly that the large majority of the cost of such a study comes from labor work, specifically data post treatment & analysis, and the writing of the report. The data presented in Figure 3.1 can be useful for pinpointing the primary sources of costs and better understanding the factors that can be adjusted to reduce the overall expenses of the study.

Figure 3.1: Sunburst chart of the study's costs by category of resource and project phase